Solar RRL

Lead-Free Double Perovskites for Perovskite Solar Cells

--Manuscript Draft--

Manuscript Number:	solr.201900306R1
Full Title:	Lead-Free Double Perovskites for Perovskite Solar Cells
Article Type:	Invited Review
Section/Category:	Special issue, on invitation only: Perovskite Solar Cells and Optoelectronics
Keywords:	halide double perovskites; lead-free perovskites; perovskite solar cell
Corresponding Author:	Peter Chen, Ph.D National Cheng Kung University Tainan, TAIWAN
Corresponding Author Secondary Information:	
Corresponding Author's Institution:	National Cheng Kung University
Corresponding Author's Secondary Institution:	
First Author:	Po-Kai Kung
First Author Secondary Information:	
Order of Authors:	Po-Kai Kung
	Ming-Hsien Li
	Pei-Ying Lin
	Jia-Yun Jhang
	Martina Pantaler
	Doru C. Lupascu
	Giulia Grancini
	Peter Chen, Ph.D
Order of Authors Secondary Information:	
Abstract:	The perovskite solar cells (PSCs) have achieved high power conversion efficiency (PCE) with credible certified value over 25%. More efforts have been devoted to the development of stable and eco-friendly perovskite materials. Lead-free double perovskites (LFDPs) have become a noteworthy choice as a photo-active layer because of their favorable photovoltaic properties, intrinsic chemical stability, and environmental friendliness. This review presents various LFDP materials whose structural stability and optoelectronic properties are predicted by theoretical calculation. We also review synthesis and experimental properties of LFDP and its application in PSCs and optoelectronics in pursuing high performance, low toxicity and functional stability. Perovskites active layer are critical for PSCs and their appropriate properties are responsible for achieving high PCE. On the other side, the stability of PSCs under working conditions is a critical requirement for its practical applications. Defect-ordered perovskites are also presented to provide another outlook of lead-free perovskite based photovoltaic. The introduction and interest towards lead-free double perovskite in PSCs can represent a viable solution to the toxicity issue, stimulate further research and bring real impact for future photovoltaic technologies.
Additional Information:	
Question	**Response**
Please submit a plain text version of your cover letter here.	Dear Editor,

Powered by Editorial Manager® and ProduXion Manager® from Aries Systems Corporation

	Enclosed please find the invited manuscript entitled "Lead-Free Double Perovskites for Perovskite Solar Cells" for the submission to the special issue of "Perovskite Solar Cells and Optoelectronics" on Solar RRL. The perovskite solar cells (PSCs) based on lead have achieved high power conversion efficiency (PCE) with credible certified value over 24% (see NREL efficiency chart, http://www.nrel.gov/ncpv/images/efficiency_chart.jpg). Currently, several issues such as device stability and toxicity are the focus to make real impact for this technology. Lead-free double perovskites (LFDPs) have become a noteworthy candidate for lead substitution because of their favorable photovoltaic properties, intrinsic chemical stability, and environmental friendliness. This review starts with various LFDP materials whose structural stability, band diagram and optoelectronic properties are predicted by theoretical calculation (Section 2). In Section 3, synthesis and experimental properties of LFDP and its application in PSCs in pursuing high PCE, low toxicity and functional stability are presented. Finally, the outlooks for lead-free substitution are addressed in Section 4, which is focused on double perovskite-based optoelectronic application and defect engineering of double perovskites. These applications have delivered promising performance due to the unique properties of individual double perovskite. The expansion of the lead-free double perovskite in PSCs can stimulate further research and bring real impact for future photovoltaic technologies. Other than photovoltaics, many optoelectronic applications have been revealed recently, showing the potential and growing space of such LFDP based material. To sum up, this review provides a brief but full picture for developing LFDP-based perovskite solar cells with the merits of growing efficiency, low toxicity and long-term stability. We believe this review would be of critical to the special issue of "Perovskite Solar Cells and Optoelectronics" launched by Solar RRL, and related to the researchers in the field of perovskite-based photovoltaics and optoelectronics. With my best regards, Peter Chen Professor Department of Photonics, National Cheng Kung University No.1, Dasyue Road, Tainan, Taiwan 701 Tel: +886-6-2757575 ext. 63919 E-mail: petercyc@mail.ncku.edu.tw
Do you or any of your co-authors have a conflict of interest to declare?	No. The authors declare no conflict of interest.

Powered by Editorial Manager® and ProduXion Manager® from Aries Systems Corporation

DOI: 10.1002/ ((please add manuscript number))
Article type: Review article

Lead-Free Double Perovskites for Perovskite Solar Cells

*Po-Kai Kung, Ming-Hsien Li, Pei-Ying Lin, Jia-Yun Jhang, Martina Pantaler, Doru C. Lupascu, Giulia Grancini and Peter Chen**

Po-Kai Kung, Ming-Hsien Li, Pei-Ying Lin, Jia-Yun Jhang
Department of Photonics, National Cheng Kung University, Tainan, 701, Taiwan
Martina Pantaler, Prof. Doru C. Lupascu
Institute for Materials Science and Center for Nanointegration Duisburg-Essen (CENIDE), University of Duisburg-Essen, Universitätsstraße 15, 45141 Essen, Germany
Prof. Giulia Grancini
Department of Physical Chemistry, University of Pavia, Via Torquato Taramelli 14, 27100 Pavia, Italy
Prof. Peter Chen
Department of Photonics, National Cheng Kung University, Tainan, 701, Taiwan
Hierarchical Green-Energy Materials (Hi-GEM) Research Center, National Cheng Kung University, Tainan, 701, Taiwan

E-mail: petercyc@mail.ncku.edu.tw

Keywords: halide double perovskites; lead-free perovskites; perovskite solar cell

The perovskite solar cells (PSCs) have achieved high power conversion efficiency (PCE) with credible certified value over 25%. More efforts have been devoted to the development of stable and eco-friendly perovskite materials. Lead-free double perovskites (LFDPs) have become a noteworthy choice as a photo-active layer because of their favorable photovoltaic properties, intrinsic chemical stability, and environmental friendliness. This review presents various LFDP materials whose structural stability and optoelectronic properties are predicted by theoretical calculation. We also review synthesis and experimental properties of LFDP and its application in PSCs and optoelectronics in pursuing high performance, low toxicity and functional stability.

Perovskites active layers are critical for PSCs and their appropriate properties are responsible for achieving high PCE. On the other side, the stability of PSCs under

working conditions is a critical requirement for its practical applications. Defect-ordered perovskites are also presented to provide another outlook of lead-free perovskite based photovoltaic. The introduction and interest towards lead-free double perovskite in PSCs can represent a viable solution to the toxicity issue, stimulate further research and bring real impact for future photovoltaic technologies.

1. Introduction

The continuous increase of energy demand worldwide has tremendously increase the photovoltaic (PV) development. Perovskite solar cells have emerged as a promising PV technology. Starting from 2009, Miyasaka et al. used methylammonium lead iodide and bromide ($CH_3NH_3PbI_3$ and $CH_3NH_3PbBr_3$, respectively) to substitute the sensitizer in liquid dye-sensitized solar cells (DSSC): the debut of perovskite in PVs.[1] In this case, however, the perovskites were unstable in the polar solvent. To obviate this issue, two ground-breaking works have sooner demonstrated the potential of perovskite active layer in solid state DSSC, adopting solid-state hole conductor to replace the liquid electrolyte. These first realized solid-state PSCs showed efficiencies of 10.9% and 9.7% by Grätzel's and Snaith's group, respectively.[2] These pioneer works stimulated extensive research efforts to optimize and boost the performance of PSCs.

Among the past decade, the PCE of PSCs has achieved over 25% [3] as a result of combined efforts in material optimization, device architecture, and interfacial engineering. Such attempts have made PSCs the first all-solution-processable PV technology outperforming the efficiencies of the current technologies based on polycrystalline and thin-film silicon solar cells. The remarkable enhancement of PCE is attributed to the superb optical and photophysical characteristics of perovskites which shows the capability of broadband absorption ranging from the visible to near-infrared spectrum (300-800 nm) along with the high extinction coefficient (of $\approx 10^5$ cm^{-1} at 550 nm), allowing the saturated light absorption within 400-500 nm thickness. Moreover, the low exciton binding energy (which is already dissociated at room temperature), long diffusion lengths, and pronounced defect tolerance are all beneficial for PV technology. These unique properties are further reflected by other fields, such as photodetector[4] and light-emission device.[5]

Although the PCE of PSCs approaches the theoretical efficiency limit for single junction solar cells, the commercial availability of PSCs is now hindered by challenging issues such as stability and toxicity due to the constituents of organic compound and lead. It has been shown that perovskite material has a tendency of degradation upon exposure to moisture, heat, or prolonged illumination in the ambient environment.[6] Numerous efforts have been recently devoted to solving such issues and some strategies showed promising long-term stability. Among them, to enhance the long-term stability

of PSCs, some major solutions are adopted such as (a) compositional engineering,[7] (b) dimensional engineering[8] and (c) lead-substitution[9] in perovskites, (d) application of inorganic charge transport layers[10] and (e) device encapsulation.[11] These aforementioned methods effectively extended the lifetime of the device from a few days to several months in certain aging scenario. However, very few can really sustain under true working condition for long time. The second issue is the lead content within the perovskite crystal. Although the lead content is not much, the potential exposure of such toxic element is still a serious concern for the health and the environment. Lead-based perovskites have shown the tendency of releasing toxic PbI_2 as a degradation product. Besides, the readily dissolution of Pb^{2+} in water would form the toxic solution which results in environmental pollution and damage toward the human. Lead is harmful to the nervous and reproductive systems and to the hematopoietic and renal organs, mainly as a result of increased oxidative stress.[12] According to U.S. Department of Health and Human Services, children exposed to lead resulted in high risks of having learning disabilities, behavioral problems, malformed bones, slow growth, seizures, coma, and even death.[13]

Despite the achievements of encapsulation, toxic Pb in PV modules must ultimately be replaced with an environmentally benign or less harmful substance. Some criteria of selecting Pb alternative will be addressed in Section 2. A straightforward idea is to substitute Pb with elements of the same group IV, such as tin (Sn) and germanium (Ge).[14] Nevertheless, devices employed Sn and Ge showed lower, incomparable performance with the Pb-based PSCs. For instance, the Sn-based PSCs generally exhibit a PCE of less than 10%.[9, 15] Besides the photovoltaic performance, both Sn and Ge show a tendency of oxidation from the +2 state to the +4 state due to their high energy 5s and 4s orbitals. This phenomenon turns out to be a rapid decomposition of perovskite material which is unfavorable for the long-term application.[16]

Another option to carry out lead-free active layer while retaining the typical perovskite crystal structure is to replace two Pb^{2+} cations with a pair of nontoxic heterovalent (i.e., oxidation states of +1 and +3) metal cations. Such compound is known as“double perovskites”with a typical formula of $A_2M(I)^{+}M(III)^{3+}X_6$. An alternative of replacing two heterovalent metal cations substitution is using one tetravalent metal cation and one vacancy site, whose general formula is $A_2M(IV)^{4+}X_6$, in order to maintain charge neutrality. The double perovskite composed of tetravalent ions is regarded as vacancy-ordered halide double perovskites which are the analogy of $AM(I)^{+}M(III)^{3+}X_6$. The pioneer compound of LFDP is $Cs_2AgBiBr_6$ whose spectroscopic limited maximum efficiency was calculated to be less than 8%.[17] The realization of $Cs_2AgBiBr_6$ double perovskites as an active layer in PSCs revealed the possibility of other promising candidates, such as $Cs_2InSbCl_6$, $Cs_2AgInBr_6$,

$Rb_2AgInBr_6$, and $Rb_2CuInCl_6$. They are being predicted to show higher PCE and suitable bandgaps compared to $MAPbI_3$ counterpart.[18, 19] Double perovskites pave a way for opening up more substitution choices of using different metal cations in the B-site.[20, 21-23]

Early applications of double perovskites majorly include the involvement of oxide-based double perovskites due to its impressing properties, such as paramagnetism, ferromagnetism, and magnetoresistance.[24] Research interest has recently been shifted to halide-based double perovskites for potential PV application due to the aforementioned findings. Numerous efforts have been devoted to overcome the issues of toxicity and stability in PSCs.

Our main goal in this review is to present the feasibility and potential of double perovskites serving as an active layer for solar cells and highlight their current issues. Theoretical calculations for predicting the material properties, such as structural stability and optoelectronic properties, of double perovskite are presented in **Section 2**. Simulation effectively provides a rational way to deduce appropriate candidates from the various combination of LFDPs. Despite the ability to narrow down search window, simulation still holds its limitation on accurate prediction. The mismatch between experimental results and theoretical calculations are highlighted. In **Section 3**, experimental results of double perovskites are reviewed, including material synthesis, bandgap engineering, dimensional engineering and their application in PV performances. Two prototypical LFDPs of $Cs_2AgBiBr_6$ and $Cs_2AgInCl_6$ play a major role in this section. It is noted that LFDPs-based PSCs are majorly composed of inorganic compounds which exhibit decent device stability but poor PCE. Issues such as indirect bandgaps resulting from the B-site cations belonging to IIIA groups and parity-induced forbidden transition causing by that from the VA group are discussed. This section further strengths the raising desire for future research.

The challenges and outlooks of LFDP in the beginning and end of section 2 and 3 (i.e. concluding remarks) are highlighted to present the whole puzzle in the existing studies and provide possible solutions or directions. Finally, the opportunities for LFDP are addressed in **Section 4** which focuses on optoelectronic applications and defect engineering. These applications have delivered promising performance due to the unique properties of individual double perovskite. One example is the efficient light emitting diode (LED) resulted from the high photoluminescence quantum efficiency (PLQE) of $Cs_2AgInCl_6$.

2. Theoretical calculations on the materials properties of lead-free double perovskite

The organic-inorganic hybrid perovskites basically follow the Goldschmidt rule which is widely adopted to verify their structural stability. To further discover perovskite with possible compound, trial-and-error-based Edisonian approaches and rational methodology comprising computational screening are commonly employed. Experimental validation, such as material synthesis or crystallinity, is required. As a derivative of organic-inorganic hybrid perovskite, the design of double perovskite is examined by the Goldschmidt rule to obtain a stable lattice structure, as revealed in **Section 2.1**. Hundreds of possible LFDPs candidates stand out after the evaluation.

In addition to the structural stability, optoelectronic properties have a significant impact on the performance of photonic devices. Two major families of $CsAgBiX_6$ and $CsAgInX_6$ have been widely evaluated. Their electronic structures, doping effect, and defects are discussed in **Section 2**. The disadvantages of wide bandgap, indirect bandgap, and parity-induced forbidden transitions hinder the usage of $CsAgBiX_6$ and $CsAgInX_6$ as an active layer for PSCs. Current results suggest that searching a new alternative is highly demanded in order to pursue high PCE and competitive working stability for the LFDP-based solar cell. The significant deviation between the calculated values and the experimental measurement, such as inconsistency of bandgap values, suggested the limit and deficiency of theoretical calculation. An accurate calculation of electronic structure is required to figure out coincident bandgap with the experiment.

2.1 Formability and crystal structure of double perovskites

The crystal structure of perovskite family originates from the mineral-$CaTiO_3$, which follows the formula of ABX_3. Divided by nature of the anionic species (X), discovered perovskite can be classified into oxide- (O^{2-}) and non-oxide-based perovskites such as chalcogenide (S^{2-}, Se^{2-}, Te^{2-}) and halide (Cl^-, Br^-, I^-). Besides, pseudohalide anions such as $HCOO^-$ [25], BF_4^- [26], or SCN^- [27] are also possible chemical species for perovskites.

From the formability point of view, several electronic and structural requirements needed to be satisfied in order to form perovskite structure. First, the charge neutrality between cations and anions need to be maintained, i. e. N(A) + N(B) = 3 N(X), by which N stands for the electronic charge of the individual A, B, or X ions.[28] For retaining stable octahedra, the octahedral factor μ of metal halide perovskite should has a value between 0.442 and 0.895. Furthermore, the ionic radii of A, B and X need to meet the Goldschmidt rule which predicts a stable perovskite structure by the ratio of the ionic radius.[29, 30]

The required factors for obtaining stable structure are presented in **Eq. 1**, which is known as octahedral factor μ and tolerance factor *t*. The octahedral factor μ, prediction of the stability of the BX_6 octahedra, is the ratio between the ionic radius of B-site

cation (r_B) and that of X-site anion (r_X), hence the feasible size of B-site cation is limited by the octahedral cavity defined by the X_6 octahedron. For a stable perovskite structure of metal halide perovskite, the μ value should be in the range of $0.442<\mu<0.895$.[30-32] The Goldschmidt rule stands for the calculation of tolerance factor *t* according to **Eq. (1)**, which applies the ionic radii of A, B and X ions (r_A, r_B, and r_X) to predict the crystallized structure.[29, 31, 32] Such relation can be applied to estimate the tolerable mismatches of sizes of the A, B, and X ions in order to form the perovskite-like crystal with structural stability.

$$\mu = \frac{r_B}{r_X} \qquad t = \frac{(r_A + r_X)}{\sqrt{2}(r_B + r_X)}. \tag{1}$$

Following the Goldschmidt rule, a stable ABX_3 perovskite structure should have a tolerance factor within $0.8 < t < 1.0$. Take $t = 1$ as an example, such a tolerance factor can result in an ideal ABX_3 perovskite structure with a cubic crystal structure, such as $SrTiO_3$.[33] For the tolerance factor ranging from 0.9 to 1.0, the perovskites demonstrate a major structure composed of a cubic unit cell. With a decreasing tolerance factor (t = 0.80-0.89), the materials tend to crystallize into distorted perovskite structures, such as orthorhombic, tetragonal, or rhombohedral crystal structure. For $t < 0.8$, the A cation is too small to retain the perovskite structure, and the perovskite structure thus turns into an alternative structure such as the ilmenite-type $FeTiO_3$. If $t > 1.0$, the oversized A cation in ABX_3 cubic structure lead to a hexagonal structure.[31, 34]

The Goldschmidt rule is also employed to describe the idea of homovalent (isovalent) and heterovalent (aliovalent) substitution within hybrid organic-inorganic perovskite for structural determination, such as Sn-based perovskite and double perovskites, in order to search potential candidates for photovoltaic applications based on the ionic radii of the involved ions. With the application of Goldschmidt rule, Kieslich et al. reported simulated divalent-metal-cation substitution for lead substitution to form novel perovskites with around 600 undeveloped compounds introduced, such as alkaline-earth metal- and lanthanide-based perovskites.[35]

The prototypical $MAPbI_3$ shows a standard structure of hybrid organic-inorganic perovskite where the Pb occupies the center of the regular PbI_6 octahedra and thus forming a comer-shared three-dimensional network, as shown in **(Scheme 1)** The structure of $MAPbI_3$ composes of an orthorhombic lattice with a space group of Pnma under low temperature and undergoes a two-phase transition with increasing temperature.[36]

The expected perovskite structure is a network of corner-sharing octahedral along with a cuboctahedral cavity occupied by the A-site atom and a six-fold coordination between the B-site ion and the halide ions.[23, 37-39] For double perovskite, the B-sites

are occupied by cations with different valences (e.g. Ag^{+} and Bi^{3+}) and the charge difference between two B-site metal ions has reported to induce the rock-salt ordering crystal structure. The unit cell of double perovskite is identical with typical perovskites, but the B^{+}/B^{3+}-site octahedra are spatially staggered to create the double perovskite as shown in **Scheme 1**.[40] Recently, Nazeeruddin et al. analyzed the applicability of the tolerance factor and octahedral factor for vacancy ordered double perovskite, $A_2M(IV)^{4+}X_6$, by summarizing the existing experimental data.[41] They indicated that the tolerance factor is applicable for LFDPs since its applicability was examined by comparing the values of tolerance factor with the crystallography data. The structural stability map demonstrated the relationship between the tolerance factor and the crystal structure. The crystal structure presented a distinguishable range of tolerance factor between the perovskite structure and the non-perovskite structure, indicating an accurate prediction of the perovskite structure. On the contrary, the structural map exhibited that the relation between the octahedral factor and the crystal structure showed no distinguishable range of μ between the perovskite structure and the non-perovskite structure.

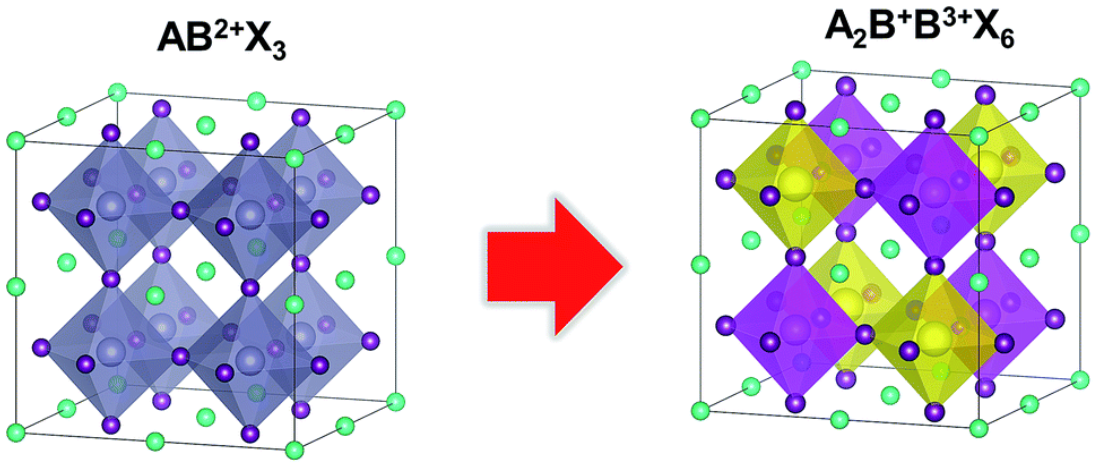

Scheme 1. Illustration of typical perovskite ABX_3 and double perovskite $A_2M`M``X_6$ with the alternated B-site substitution. The B-site ions of double perovskite were filled with B^{+}/B^{3+}, which was varied from the typical B^{2+}. The cyan, gray, yellow, pink, and purple color balls stand for A^{+}, B^{2+}, B^{+}, B^{3+}, and X^{-} ions, respectively.[40]

The crystallographic nature of double perovskites was studied by the application of powder X-ray diffraction (XRD) and single crystal XRD which verified the perovskite-like structure of double perovskites.[42] The Goldschmidt rule indicated that silver ion in $Cs_2AgBiBr_6$ possessed a suitable radius to support octahedral coordination of halides (Br^{-} and I^{-}) in the perovskite crystal lattice.[37] Moreover, other reports experimentally revealed that $CsAgBiX_6$ crystallized into a truncated octahedral crystal with a cubic space group of Fm-3m.[23, 38, 43] It is worth noting that the unit cell axis of $Cs_2AgBiBr_6$

is estimated to be ≈11.25 Å, which is double to that of $MAPbBr_3$ (≈5.92 Å).[44] The B-site elements (e.g. Ag^+& Bi^{3+}) possessed different metal–halide bond lengths which can be estimated from the distinct ionic radii of the Ag^+(129 pm), Bi^{3+} (117 pm) and Br^- (183 pm). The different Ag-Br and Bi-Br bond lengths were expected to alternate the crystallization nature within a cubic unit cell, but no crystallographic evidence shows that the lattice distortion could be induced by using different B-site ions. Further investigation is needed to gain insight into the relation between the dissimilar metal halide bond lengths and the crystallographic disorder.[45]

The stability and formability of double perovskites are usually predicted by the tolerance factor *t* and octahedral factor μ with appropriate value from 0.81 to 1.11 for *t*, from 0.44 to 0.90 for μ to give a stable perovskite structure.[30] These factors could be further adjusted to enhance the accuracy for predicting the structure of vacancy ordered double perovskites which have a general formula of A_2BX_6 including the substitution of a pair of B-site ions with a quadrivalention and a vacancy. The structural stability of vacancy ordered double perovskites could be decided by the radius ratio of A-site cation to that of a 12-coordinate void according to tolerance factor and octahedral factor.[46] The vacancy-ordered structure goes through a symmetry-lowering phase transition upon cooling, resulting from a cooperative octahedral tilting and rotations of the crystal structure. The influential factor of the phase transition was the difference in ionic radii of the composing atoms.

The accuracy of *t* was further improved by the proposal of a new tolerance factor τ, as shown in **Eq. 2** with the consideration of electronic charges.[47]

$$\tau = \frac{r_X}{r_B} - n_A\left(n_A - \frac{r_A/r_B}{\ln(r_A/r_B)}\right) \quad (2)$$

In **Eq. 2**, n_A stands for the oxidation state of A ion, and r_i for the ionic radius of I ion. The presence of τ offered a new indicator, which could also be extensively adapted, for prediction of the novel compound with its accurate and probabilistic nature. It is worthy to note that the structural stability of perovskites showed a monotonic dependence on τ (e.g., as τ increased, the probability of being perovskite decreased) and a stable perovskite structure was expected to exist when $\tau < 4.18$. Oppositely, the structural stability doesn't vary monotonically with the change of *t*. Moreover, τ was combined with μ as a single-variable descriptor which is contrary to the usual double-variable descriptor (t, μ) and hence such index gained more physical insight of structural prediction of new stable inorganic and hybrid organic-inorganic single and double perovskites.

In 2018, a new strategy composed of machine-learning and first-principles density functional theory (DFT) calculations for predicting structural stability of halide double perovskites was proposed and delivered calculated results matched with experimental investigations. However, the stable perovskite structure of double perovskites exhibited a possibility of limiting the interactions of outer most orbitals of neighboring cations by confining them into either only B(I) site cations or B(II) site cations within a cubic unit cell. Thus, a localized, narrow conduction band along with a wide bandgap could be observed for double perovskites.[17] As a result, alternatives other than cubic unit cell suggest a potential way for the realization of remarkable properties similar to Pb-based perovskites.

2.2 Optoelectronic calculations of lead-free double perovskites

Due to the massive available and undeveloped chemical combination for ABX_3 structure, combinatorial computational high-throughput screening (HTC) could assist the design of double perovskites. In the following section, numerous theoretical calculations on optoelectronic properties for lead-free double perovskites in pursuing decent photophysical properties, nontoxicity, and ambient stability are reviewed

For searching alternatives ion of Pb^{2+}, the electronic structure calculations have drawn considerable attention in order to determine the electronic properties of LFDP before synthesis. Umebayashi et al. reported that the Pb^{2+} possessed an electronic configuration of $6s^26p^0$ which significantly influenced the band structure of $MAPbI_3$.[48] The valence band maximum (VBM) of $MAPbI_3$ was composed of hybrid electronic states of the filled $6s^2$ and $5p^6$ states of Pb^{2+} and I^-, respectively, while the conduction band minimum (CBM) was composed of the vacant 6p state of Pb^{2+} resulting in outstanding photovoltaic properties. The $6s^26p^0$ electronic configuration was also exhibited in both Tl^+ and Bi^{3+} except for Pb^{2+}, but only Bi^{3+}possessed nontoxic nature and was applied into organic reactions as a nontoxic additive.[49]

The pioneering works demonstrated that double perovskites, which filled the B-sites with trivalent Bi^{3+} cation along with monovalent Ag^+ cation, were potential candidates for efficient lead-free PSCs.[23, 37, 38] As-synthesized compounds have shown a capability of acting as a light absorber and active layer due to its suitable bandgap and long photoluminescence (PL) lifetime. Although the toxic issue remained with the presence of Ag^+, the low solubility constant (K_{sp} at 25 °C = 5×10^{-13}, four orders lower than that of Pb^{2+}) suggested minor damage. Many substitutions such as Cu^+, K^+, Tl^+, In^+, and Na^+ have been proposed, which will be discussed in following sections. The main material discussed in Section 2.2.1 is Cs_2AgBiX_6 and its relevant compounds. Bandgap mismatch between simulation and experiment, ion substitution, and indirect bandgap of these materials are widely discussed. Current advances of Bi-based LFDP

lies in the direction of bandgap engineering via ion substitution at M-site or X-site. The other key issues such as optical properties (absorption coefficient or refractive index) and electronic properties (defect state, exciton binding energy or carrier diffusion length) of LFDPs, development of energy level matching carrier transport layer, carrier dynamic and interfacial engineering at perovskite/carrier transport layer interface are rarely discussed.

A potential candidate of Cs_2AgInX_6 and its relevant compound are highlighted in **Section 2.2.2**. However, theoretical calculations combing with the experimental results of these compounds demonstrate the parity-induced forbidden transition which hinders their development in PV technique. Some alternatives for $Cs_2AgInCl_6$ with direct bandgap are proposed to avoid the parity-induced forbidden transition but few of them are realized.[50] Besides, the defect properties are also examined via simulations but further experimental verification is needed. Development of LFDP other than Cs_2AgBiX_6 or Cs_2AgInX_6 is highly demanded to improve the performance of LFDP-based PSCs.

2.2.1 Theoretical calculations of Bi-based double perovskites

Bismuth trivalent ions possess identical electronic structure and the lone-pair *s* electron to lead ions. Therefore, Bi-based PSCs was expected to inherit the extraordinary performance of $MAPbI_3$-based PSCs. Nevertheless, most reported lead-free double perovskites, either experimentally or theoretically, demonstrated indirect bandgaps.[17, 37, 43, 51] For instance, compounds of Cs_2AgBiX_6 (X = Cl, Br, and I) family were shown to have indirect bandgaps determined by optical measurements and electronic structure calculations.[17, 52, 53] Moreover, various bandgap values of single double perovskite have been reported and the wide variety of possible causes were proposed, such as synthesis route and characterization technique.

Specifically, $Cs_2AgBiBr_6$ exhibited an indirect bandgap of 1.98 eV along with the energy barrier of direct transition as high as 2.21 eV which is lower than that of $MAPbBr_3$ (2.3 eV).[37, 54] The chemical mismatch between Ag and Bi was the main cause of indirect bandgaps and the presence of 4d states of Ag atom was responsible for the reduced bandgap of Cs_2AgBiX_6 (X = Cl, Br, and I).[17, 23, 55] The first principle calculations suggested the CBM of Cs_2AgBiX_6 was majorly composed of the Bi-6p/halogen-p antibonding states at the L point (π/a, π/a, π/a) while the VBM located at the X point ($2\pi/a$, 0, 0) was resulted from the Ag-4d/halogen-p hybrid orbitals, which lead to the establishment of indirect bandgaps.[23, 43]

Besides the indirect bandgap nature, the values of bandgaps are 1.8–2.2 and 2.2–2.8 eV for $Cs_2AgBiBr_6$ and $Cs_2AgBiCl_6$, respectively. The bandgap of $Cs_2AgBiBr_6$ nanocrystals (NCs) reported by Zhou et al. was 2.52 eV which was 0.57 eV higher than

the bandgap of bulk $Cs_2AgBiBr_6$ (1.95 eV) and was attributed to the quantum confinement effect in NCs. The absorption spectra of the $Cs_2AgBiBr_6$ NCs displayed a sharp peak which was blue shifted from the band edge with a value of more than 1 eV.[56] Interestingly, such peak shift was ascribed to the direct Bi s–p transition instead of quantum confined excitonic transition. Li et al. stated that the width of the bandgap of $Cs_2AgBiBr_6$ could be adjusted by structural modulation under high pressure.[57] Under pressure around 15 GPa, the bandgap was 1.7 eV, a significantly reduced value compared to the bandgap under ambient pressure. The wide variety of deduced bandgap values suggested the need of accurate bandgap predication for searching outstanding candidates of PV application.

Figure 1 summaries the experimental bandgap value of reported lead-free double perovskites. It is noted that $Cs_2AgBiBr_6$ and $Cs_2AgBiCl_6$ double perovskites deliver a broad distribution of bandgap values.[52, 53] Such inconsistency can be ascribed to the routes of material synthesis,[23, 43] characterization methods,[23, 37, 58] and selected models for calculations.[17] Variation of preparation approaches could lead to different morphology and structure of the final product, resulting in different material form, such as bulk or NCs.[59] The NCs structure could considerably influence the electronic configuration of compound due to quantum confinement, resulting in modified bandgaps.

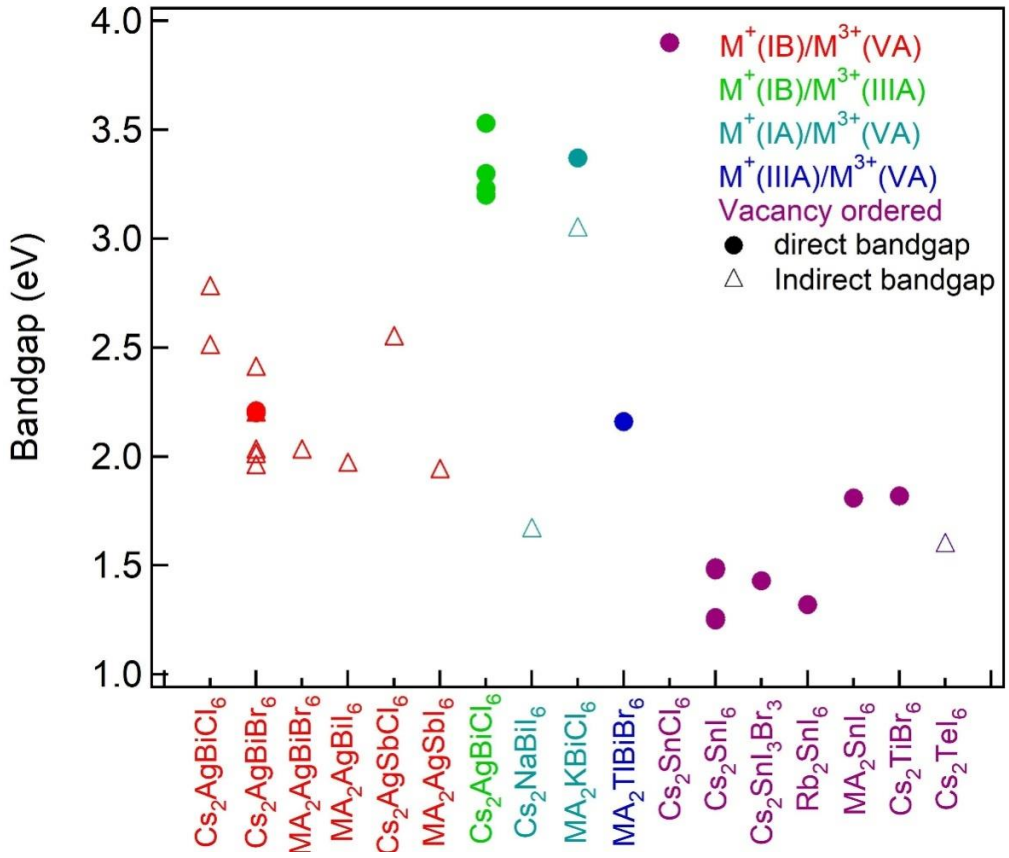

Figure 1. Bandgap values and transition nature of experimentally-synthesized double perovskite.

Two widely applied calculations for estimating the bandgaps of materials are Perdew–Burke–Ernzerhof (PBE) and Heyd–Scuseria–Ernzerhof (HSE), which the accuracy could be further improved with the strong dependence on the fraction of exact exchange-α. For instance, such inaccuracy was demonstrated by Hoye et al. who calculated the bandgaps for two polymorphs of BiI_3 at different α using HSE.[60] Results showed that a wide variation of bandgap up to 0.5 eV could be delivered depending on α. Other inaccuracy of bandgap evaluation might result from fitting procedure of the Tauc plot.

Given the results above, a detailed investigation is needed for bandgap variation since the bandgap plays a critical role during operation of PSCs. Single particle Green's function and the screened Coulomb interaction (GW) approximation effectively improved the limitation of DFT and hybrid functions despite the high cost and high computational quantities.[60] As a result, Filip et al. aimed to obtain accurate bandgap through state-of-the-art many-body perturbation theory calculations in the GW approximation basing on Yambo code.[43] Accurate bandgaps calculations were conducted and verified by experimental results with a demonstration that electronic states ($4s^2 4p^6$) of Ag^+ in double perovskite were a crucial factor of GW calculations of their quasiparticle bandgaps. The accuracy based on hybrid functions was further examined by Hoye et al. who compared the calculated results with the more accurate GW calculations.[60] With the proper α selected for the HSE calculations, two calculations presented a decent agreement.

Figure 2 displays the calculated electronic band structure of Cs_2AgBiX_6 via the DFT calculations. The wide bandgap along with the indirect transition nature induced an inefficient optical extinction. Bandgap engineering was demonstrated by Volonakiset al. who observed that the bandgap of Cs_2AgBiX_6 was reduced when smaller elements from halogen or the pnictogen column were involved, in order to obtain suitable bandgap with direct nature.[38] Consequently, the VBM increased when the X-site elements (e.g. halogen) shifted downward in the periodic table since the valence band was majorly determined by halogen-p states. On the other hand, the CBM was found to be higher as the applied pnictogen moving downward in the periodic table since the conduction band was dominated by the pnictogen-p states. Besides, the approximation of electron effective mass was estimated to be 0.53 m_e (0.37 m_e) along L to W direction, while the hole effective mass was 0.15 m_e (0.14 m_e) along X to Γ direction which were found to be comparable with that of $MAPbI_3$.

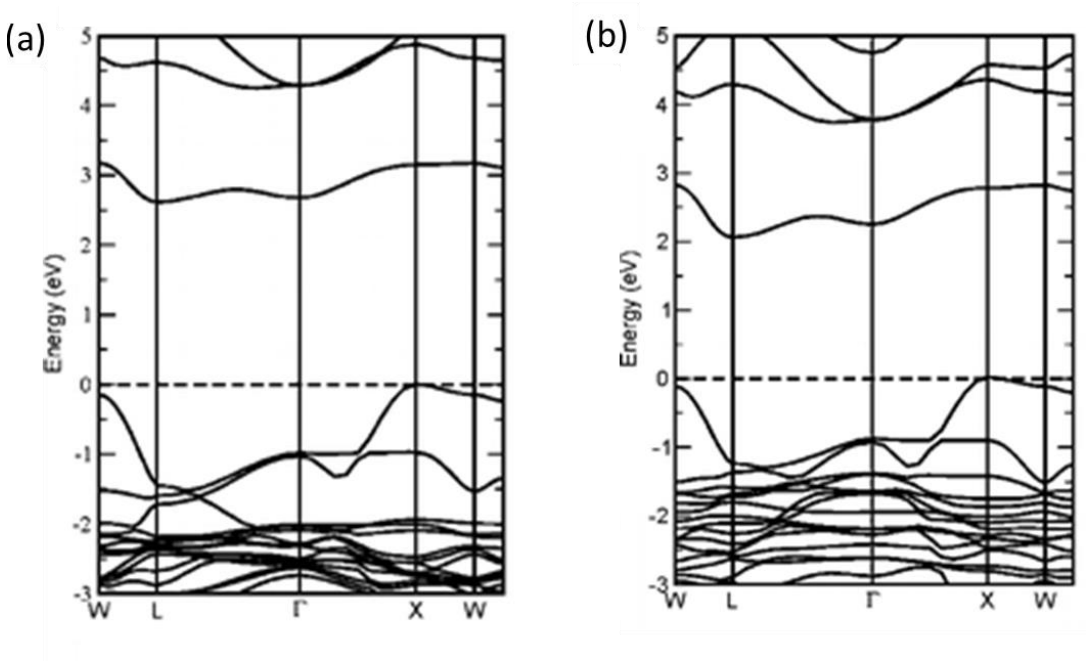

Figure 2. Electronic band structures of (a) $Cs_2AgBiCl_6$ and (b) $Cs_2AgBiBr_6$ resulted from the DFT calculations.[23]

The flexibility of elemental substitution in lead-free double perovskites allowed their bandgap and effective masses to be tuned and the hole effective masses of double perovskites were shown to be lighter than that of lead-contained perovskites.[23] Elemental substitution and doping are effective method for tuning the optoelectronic properties; thus attempts have been made in order to modify the electronic structure of double perovskites.[61] Tl was applied as a dopant in $Cs_2AgBiBr_6$ to form a compound of $Cs_2(Ag_{1-a}Bi_{1-b})Tl_xBr_6$ (x = a+b) for band edge modification. Calculation results demonstrated that the bandgap, as well as transition nature, was alternated by Tl dopant. Besides, calculation results also suggested that low-level doping of Tl^+ cation within A-sites reduced the bandgap with 0.1 eV and converted the indirect bandgap into direct nature. On the other hand, the bandgap showed a reduction of 0.8 eV and maintained its indirect nature with Tl^{3+} doped into Bi^{3+} site. Nevertheless, the toxicity of Tl is more fatal than Pb, pointing out significant room of searching alternative dopant in order to further reduce the bandgap while possessing direct transition nature without toxicity.

$Cs_2AgBiBr_6$ demonstrated its flexibility in tunable photovoltaic properties with diverse doping and elemental replacement. The calculations of $Cs_2AgBi_{1-x}In_xBr_6$ (x = 0, 0.25, 0.5, and 0.75) and $Cs_2AgBi_{1-x}Sb_xBr_6$ (x = 0, 0.125, and 0.375) presented the crucial role of atomic substitution for photovoltaic properties with alternated electronic structure.[62] The assigned range of x was determined in order to retain the double perovskite phase. The maximum substitution rate of In^{3+} was 75% which increased the

bandgap while that of Sb^{3+} was 37.5%, resulting in a reduced bandgap. Therefore, the elemental substitution enabled a maximum variation of 0.41 eV of bandgap adjustment by different atomic configurations.

Typically, the electronic configuration of semiconductor is significantly influenced by the chemical composition.[63] By controlling the ordering parameter at the mixed sublattice, the band structure of $Cs_2AgBiBr_6$ varied continuously from indirect bandgap to narrowed pseudo-direct bandgap because of the band hybridization and increased disorder of crystallization. Consequently, the VBM shifted from the Γ point to the X point and the Brillouin zone folding at the Γ point could convert the transition of bandgap from indirect to direct configuration. Despite the fact that the direct transition is forbidden by symmetry, the above observation indicated a possibility of reaching direct bandgap.[38] For further controlling the ordering parameter, octahedral tilts and various steric size could be introduced to A-site by doping or atomic substitution, such as MA or formamidinium (FA), to further alternate the electronic configuration.[64]

The partially disordered $Cs_2AgBiBr_6$ exhibited a pseudo-direct bandgap with a noteworthy value around 0.44 eV and the partial disorder was further highlighted with the presence of Ag^+ at M(I) site and Bi^{3+} at M(II) site.[51] The variation of bandgap values was also attributed to the intrinsic disorder of atoms as shown by simulations.[18] Apart from the effect of bandgap tuning, the structural disorder enabled the formation of point defects and deep trap levels with low formation energy. Li et al. demonstrated that one could control the effects of intrinsic defects on carrier trapping and Fermi-level pinning with the exploration of the phase diagram of double perovskites.[65] Experimental results demonstrated that the optimized heat treatment could lead to an ordered crystal structure of $Cs_2AgBiBr_6$ with reduced defects and enhanced mobility.[66] Kim et al. reported that the cation ordering displayed significant impact on electronic structures by changing octahedron alignments, and even zero gap states could be realized.[67] For instance, the $Cs_2AgBiCl_6$ showed reduced total energy when the $BiCl_6$ was surrounded with 6 $AgCl_6$ (0D alignment) octahedrons, resulting in a wide and indirect bandgap. Furthermore, the bandgap of $Cs_2AgBiCl_6$ was narrowed with the increasing dimensionality of $BiCl_6$.

Further investigation of electronic interaction among M(I), M(III) and X-sites within double perovskites was realized by substituting Ag^+ (d states) with ions having valence s states, such as In^+ (5s) and Tl^+ (6s).[68] In the hypothetical $Cs_2TlBiBr_6$, Tl ions possessed s states which were able to interact with the s states of bismuth. The interaction, which was suggested to be the origin of the indirect bandgap of Cs_2AgBiX_6, between Ag d states and Bi s states was eliminated in the valence when Ag ion is absent. The Tl–Bi double perovskites were semiconductors with bandgaps which were suitable for PV application while the In–Bi bromide double perovskites exhibited metallic

nature. Nevertheless, the application of Tl raised the concern of toxicity. An alternative way for changing the electronic transition nature is to fill the A sites with atoms other than Cs in order to break the symmetry restrictions, an approach yet to be explored.

The effect of lone-pair s states existed in B-site cations was also reported by Zhang et al. who manipulated the cation combinations and configurations.[40] They revealed that only the $A_2M_{IIIA}^{+}M_{VA}^{3+}X_6$ family was able to reach a direct bandgap with unlimited optical transitions among all the double perovskites with NaCl-like structure (e.g. ordered double perovskite). The VBM of $Cs_2BiInCl_6$ was predominated by In 5s and Cl 3p orbitals due to the strong s–p coupling with even parity, while the CBM was predominated by the Bi 6p orbitals due to the lack of s–p coupling with odd parity. Hence, the band edge transitions of $Cs_2BiInCl_6$ were partially allowed with parity. As a result, the M^+/M^{3+} cations in $A_2M^+M^{3+}X^6$ must possessed the lone-pair s state in order to achieve appropriate direct bandgap along with parity-allowed band edge transitions. Numerous compounds proposed by literature are inappropriate for optoelectronic application due to the indirect bandgaps or parity-induced forbidden transitions.[50, 69]

In order to perform as a promising active layer, the semiconductors are expected to exhibit high majority carrier density and low density of deep level defects. The typical $Cs_2AgBiBr_6$ exhibited beneficial defect properties since calculated results showed that the Ag vacancies could be readily formed and acted as shallow acceptors, resulting in an intrinsic p-type conductivity.[70] Moreover, Bi vacancies and AgBi antisites were deep acceptors and the dominant defects under the Br-rich growth conditions. Such results indicated the formation of deep trap levels should be inhibited when growing $Cs_2AgBiBr_6$ under Br-poor/Bi-rich conditions, leading to improved performance of PSCs. A detailed discussion is shown in **Section 3**.

The widely considered candidates of Pb substitution, such as In^+, Tl^+, Sb^{3+}, and Bi^{3+} cations, have identical ns^2 states with Pb^{2+}. Nevertheless, the energy levels of their ns^2 states are distinct from $6s^2$ of Pb^{2+} which resulted in diverse defect properties.[71] Results of DFT calculations suggested that the double perovskites composed of Tl-Bi and In-Bi along with Br in X-sites agreed with such viewpoint.[68] Xiao et al. pointed out that the Tl-Bi bromides exhibited semiconducting p-type properties, while the In–Bi bromides could only show metallic p-type regardless the synthesis condition due to the low formation energy of In vacancy. The low formation energy was attributed to the high energy level and energetically unstable In 5s state. Moreover, the In intended to replace the Bi site and thus introduced structural disorder, turning out to be a localized In-In bromide double perovskites. The local In–In bromide exhibited a lowered CBM which might reduce the open-circuit voltage. On the contrary, Tl-Bi bromide displayed the potential for photovoltaic application with desired properties under bromine-poor growth condition. The synthesis route was proposed in order to

achieve low hole density and low defect density. Despite the feasibility as an active layer, this type of double perovskites suffered from the low stability since $B(I)_{IIIA}^{+}$ was readily oxidized to $B(I)_{IIIA}^{3+}$, giving rise to a degradation of double perovskites. The oxidation was suppressed when large organic alternatives were introduced to A-site, such as MA and FA since the oxidation became energetically less favorable.

The use of organic molecule was further theoretically investigated for a few double perovskites. Ag^{+} and Bi^{3+} showed a potential for replacing Pb^{2+} in double perovskite when incorporated with organic species.[21] Cheng et al. synthesized MA_2AgBiI_6 with an indirect bandgap of 1.96 eV and an effective electron mass higher than that of $MAPbI_3$. MA_2AgBiI_6 presented decent ambient stability as its crystal structure remained unchanged for 4 months. The conduction band of MA_2AgBiI_6 (-4.3 eV) was lower than commonly applied electron transport layer (i.e. TiO_2), and thus SnO_2 (-4.5 eV) or C_{60} (-4.5 eV) may be electronically compatible with MA_2AgBiI_6. On the other hand, MA_2AgSbI_6 was synthesized by Li et al. and delivered a bandgap value of 1.93 eV.[72] Despite Bi and Sb are in the same group, the noteworthy difference of their electronic configuration was demonstrated because of the different ionic radius and the spin–orbit coupling effect. Similar substitution has been made by replacing I with Br within MA_2AgBiI_6, resulting in a bandgap of 2.02 eV which was 0.25 eV lower than that of $Cs_2AgBiBr_6$ due to the larger ionic radius of MA than that of Cs^{+}.[73] The indirect nature of the bandgap of $(MA)_2AgBiBr_6$ was verified by DFT calculation along with optical spectroscopy. The family of $(MA)_2M(I)M(III)X_6$ exhibited tunable bandgaps by changing the X-site halides and M(I)-site cations. Specifically, halide atoms with larger ionic radius would lead to the wider bandgap.

Experimental results of Bi-based double perovskites highlighted the possibility of applying double perovskites as active layers.[66, 74-83] Feng et al. presented a comprehensive study of interfacial carrier dynamic between Cs_2MBiX_6 (M = Ag, Cu; X = Br, Cl) and TiO_2 to evaluate the carrier extraction efficiency.[84] The Cs_4X_4 (X = Br and Cl)/TiO_2-mediated interfaces was beneficial for charge extraction and separation due to the withdrawn trap states of TiO_2 when contacted with Cs_4X_4. DFT calculations further indicated a suitable band alignment, reduced bandgap of double perovskites and a smooth gradient distribution for the locally projected density of states in the direction which was normal to the interfaces. These results suggested the interface between Cs_2AgBiX_6 and TiO_2 being an efficient channel for charge transfer. **Figure 3** showed the charge displacement curve analysis of Ag-based double perovskites which was an indicator of the efficient charge transfer at the interface.

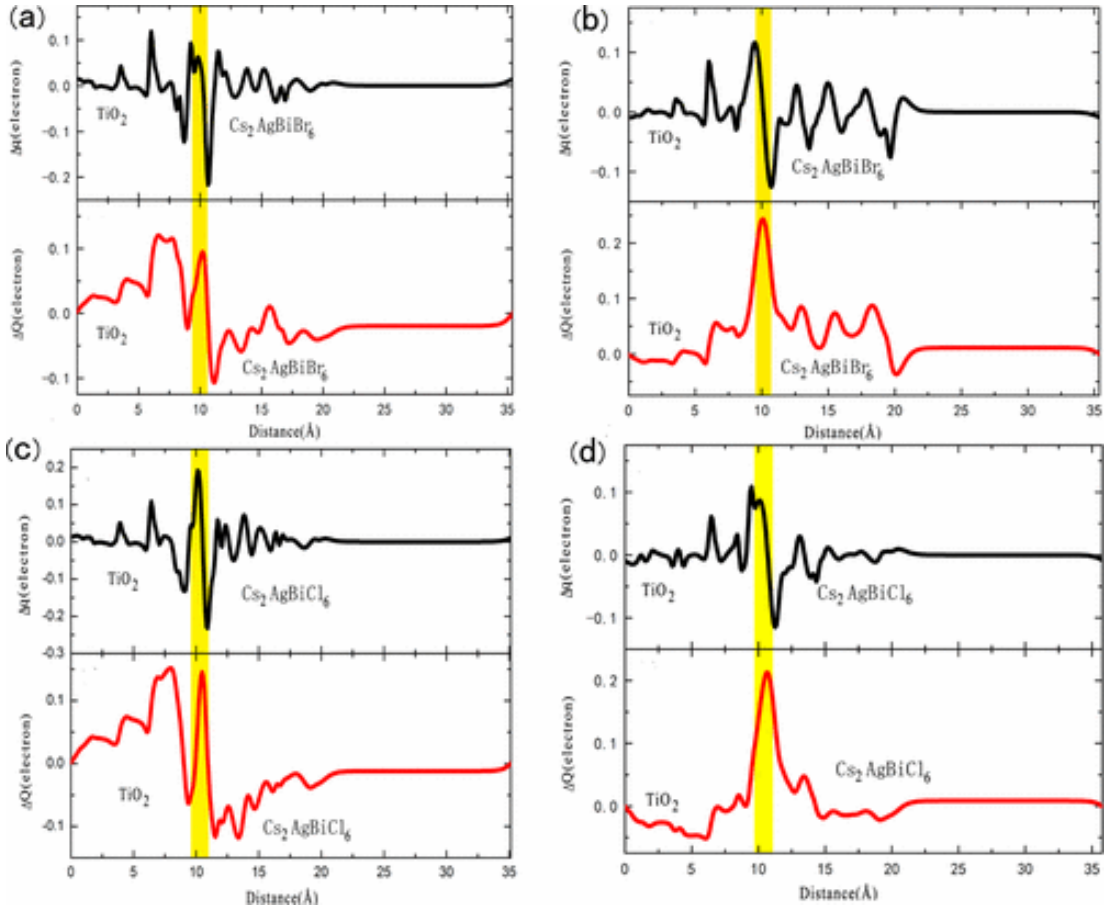

Figure 3. The plane-averaged charge difference and charge displacement curve (CDC) of (a) $Ag_2Bi_2Br_8/TiO_2$, (b) Cs_4Br_4/TiO_2, (c) $Ag_2Bi_2Cl_8/TiO_2$, and (d) Cs_4Cl_4/TiO_2 heterojunctions in Cs_2AgBiX_6 (X = Br and Cl)/TiO_2. The upper and the lower scale bar represented the plane-averaged charge difference and the CDC, respectively.[84]

2.2.2 Theoretical calculations of In-based double perovskites

In order to bypass the indirect bandgap of Bi-based double perovskites, a straightforward idea is to substitute Bi with other trivalent ions, such as In. In^{3+} shows an electronic structure without lone-pair *s* electrons, resulting in a good matching with the Ag d orbit and forming a bandgap with direct nature.[85] For instance, Ag-In and Cu-In are two combinations which were theoretically predicted to possess direct bandgap.[19, 69, 86, 87] Specifically, Cu-based double perovskites, such as $Cs_2CuInCl_6$, exhibited a narrower direct bandgap compared with corresponding Ag^+-based counterpart due to the antibonding hybridization which was formed by the Cu d^{10} states and the halide *p* states.[69, 87] Nevertheless, the Cu-based double perovskites were demonstrated to be thermodynamically unstable by DFT calculations compared with Ag-based double perovskites.[19] The low decomposition enthalpy of Cu-based double perovskites was ascribed to the higher energy level and the smaller ionic radius of Cu^+ than that of Ag^+. On the other hand, $Cs_2AgInCl_6$ exhibited a direct bandgap which was

tunable by halide substitution, such as $Cs_2InAgCl_{6-x}Br_x$, in order to realize maximum efficiency. However, this group of the compound was shown to suffer from the parity-dependent weak optical transition.

The parity-induced forbidden transitions of double perovskites, which is induced by the inversion symmetry, is a vital factor for designing double perovskites for optoelectronic applications. Volonakiset al. experimentally realized the synthesis of Cs_2AgInX_6 in early 2017 with the calculated bandgaps of 1.33 eV for $Cs_2AgInBr_6$ and 2.0 eV for $Cs_2AgInCl_6$, which demonstrated a discrepancy with the measured optical bandgap of $Cs_2AgInCl_6$ (3.3 eV).[85] Via DFT calculations, Meng et al. demonstrated that it was the inversion-symmetry induced parity-induced forbidden transitions lead to such difference.[50] This observation explained why the synthesized powder showed white color with a measured bandgap of 3.3 eV while the photoluminescence (PL) emission energy was 2.0 eV. The parity-induced forbidden transitions affected the optical absorption significantly and hindered the PV applications. As shown in **Figure 4a**, the Perdew–Burke–Ernzerhof (PBE) calculated band structure of $Cs_2AgInCl_6$ exhibited VBM and CBM with the identical even parity which induced the parity-induced forbidden transition at the Γ point. Nevertheless, the parity of the conduction band edge changed at k points away from the Γ point, while the valence band edge remained unchanged. This results in an increase in the calculated dipole transition matrix element, as the k point changes from Γ to L point. Consequently, $Cs_2AgInCl_6$ double perovskites exhibited weak optical absorption coefficients. Although a noteworthy PL lifetime of 595 ns was observed, the parity-induced forbidden transitions impede the photovoltaic application of this compound.[88]

Figure 4b was proposed by Meng et al. with nine types of lead-free double perovskite designed, while six types of them showed direct bandgap.[50] Among the six types of compound, five types of them exhibited inversion-symmetry induced parity-forbidden transitions which hampers the PV application of these materials. Only the combinations of B^+ = In, Tl and B^{3+} = Sb, Bi possessed suitable optical absorption and electronic properties for PSCs. Since the Tl is extremely toxic, the In^+ was then regarded as the only nontoxic candidate for high-efficiency PSCs. Comparing with $Cs_2AgInCl_6$, the $Cs_2InBiCl_6$ exhibited different behavior in which both the CBM and VBM lied at the Γ point. **Figure 4c** shows that the CBM of $Cs_2InBiCl_6$ had a representation of Γ^{4-} while that of VBM was Γ^{1+}, resulting in no parity-induced forbidden transition existed in this band structure. Moreover, the calculated result suggested a large transition parameter value at the Γ point which referred to remarkable light absorption. Nevertheless, the applicability of $Cs_2InBiCl_6$ remained questionable since the calculated results pointed out an instability under redox reaction.[71]

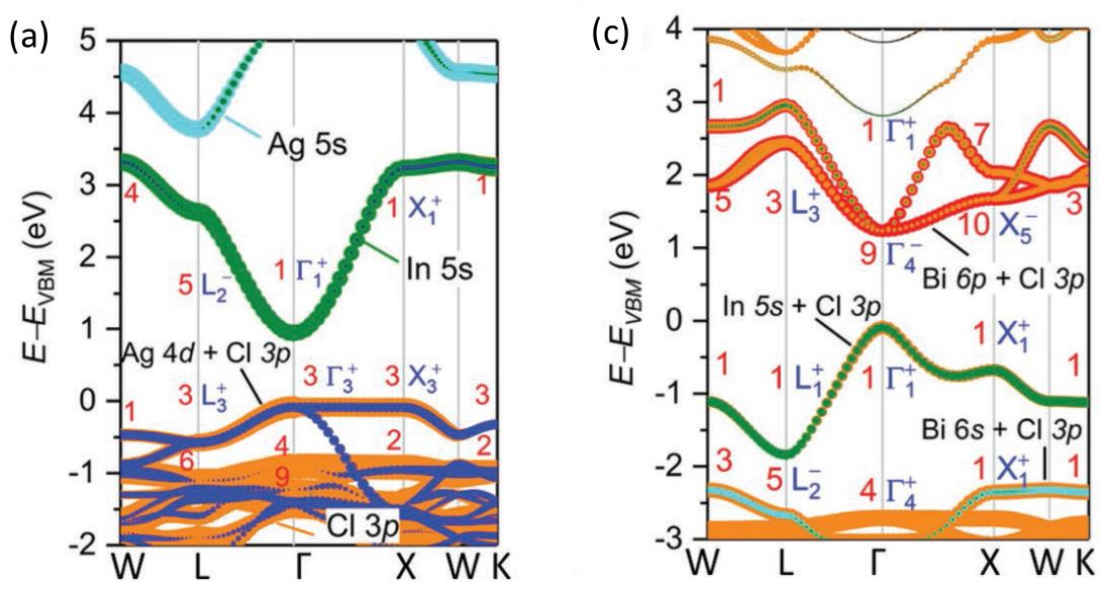

(b)

B^+ \ B^{3+}		Group 3	Group 13	Group 15
		Sc, Y	Al, Ga, In(3+), Tl(3+)	Sb(3+), Bi (3+)
Group 1	Na, K, Rb, Cs	Direct (*All forbidden*)	Direct (*All forbidden*)	Mostly Direct (*Weak transition*)
Group 11	Cu, Ag, Au	Indirect	Direct (*partial forbidden*)	Indirect
Group 13	In(1+), Tl(1+)	Direct (*Weak transition*)	Indirect	Direct (*Strong transition*)

Figure 4. (a) PBE calculated band structure provided an indication of weak transition parameter in $Cs_2AgInCl_6$. (b) PBE calculated band structures provided an indication of the strong transition parameter in $Cs_2InBiCl_6$. (c) A table of probable combinations for $A_2M^+M^{3+}X_6$ along with their parity-dependent transitions.[50]

For future double perovskite design, the parity-induced forbidden transition should be avoided in order to achieve desirable photovoltaic properties. For instance, the substitution of Pb^{2+} with a group XII or group II ion delivered the same parity at CBM and VBM without parity-induced forbidden transition induced since the CBM and VBM located at the different k points.[89] Nevertheless, the CBM and VBM would fold to the same k point with an increased size of the unit cell, leading to the parity-induced forbidden transitions between the band edges. The calculated results above were based on hypothetical double perovskite $Cs_2ZnZnCl_6$.

Defect tolerance is a crucial property for PV application. Calculated results revealed that the growth condition enabled the optimization of defect property.[90, 91] Hence, the

synthesis for obtaining high-quality double perovskite is a vital issue which will be discussed in **Section 3**. Carrier dynamics including the mobility, diffusion length and carrier lifetime of nonradiative recombination of PSCs have shown to be significantly influenced by defect properties.[92] Xu et al. carried out the first-principle calculations and discussed the intrinsic defect physics and phase stability of $Cs_2AgInCl_6$.[90] Results suggested that the shallow defects were formed under Ag-rich and Br-poor growth condition without unwanted secondary phases. This growth condition provided a decent chemical potential region to obtain $Cs_2AgInCl_6$ with direct bandgap and good n-type conductivity. Contrarily, the growth condition of $Cs_2AgInCl_6$ was also investigated by Li et al. by the first-principle calculations with different results proposed.[65] Authors suggested that the $Cs_2AgInCl_6$ should be grown under In^{3+} poor and Cl^- rich condition in order to realize $Cs_2AgInCl_6$ compound with the suppressed defect and a long minority-carrier lifetime. More research is needed to understand the discrepancy between the calculated results.

In 2019, Xu et al. further investigated the atomic structures and electronic properties of double perovskites by first-principles calculations.[91] The grain boundary was found to induce deep level defect states within bandgap and thus hinder the PV application of double perovskites. On the contrary, the formation of some intrinsic defects and defect complexes enable the elimination of these deep-levels. With the adjustment of chemical potential, these defects or defect complexes were found to be incorporated into the grain boundary avoiding the disadvantageous of deep-level defects. Above-mentioned results of theoretical calculation provided insights and guidance for the future design of double perovskites. More research activities are required to explore the numerous materials suggested by theoretical calculation to realized high performance PV characteristics.

2.2.3 Concluding remarks:

The structural formability stands as a stepping stone for obtaining perovskite structure with a stable cubic lattice and identifies numerous possible combinations of novel LFDP. The applicability of tolerance factor along with the octahedral factor for LFDP has been recognized as an effective evaluation for material prediction. The newly developed factor τ varies monotonically with the ionic radii and provides a straightforward way for predicting the formability. Considering the various combinations of M(I) and M(III), the modified tolerance factors effectively narrow down the range of searching lead-free perovskite alternatives.

The different bond length between Ag-Br and Bi-Br might lead to lattice distortion which has an impact on the defect formation, structural stability and electronic properties. The effect induced by lattice distortion has not been investigated. In a cubic unit cell of LFDPs, the outermost electron orbital of neighbor M' site and M'' site

cations are localized (without overlap) which results in a flat conduction band minimum and a wide bandgap. As a result, the crystal structure beyond cubic cell is suggested to be an approach to realize promising properties akin to Pb-based perovskites, such as the Ag-Bi-I system.

Bi-based LFDPs possessing the $6s^0 6p^0$ electronic configuration are widely investigated through calculations and experiments. The different electronic configuration between Ag and Bi results in an indirect bandgap of the prototypical LFDPs (i.e. $CsAgBiX_6$ and its relevant compounds), implying that the element combinations from group 11 and group 15 give rise to an indirect band transition. Although various bandgap engineering is proposed to eliminate the involvement of phonon during the transition, such as A-/B-site substitution, dimensional engineering, and synthesis route, the intrinsic wide and indirect bandgap limit the spectral power conversion efficiency of $CsAgBiBr_6$-based solar cells with an 8% maximum. On the other hand, the Cs_2AgInX_6 family exhibits direct bandgap but the emerging issue lies in the parity-induced forbidden transition. Such effect results in a wide optical bandgap which hinders the device performance. Alternatives such as $A_2M_{IIIA}^{+}M_{VA}^{3+}X_6$ family with direct bandgap and parity-allowed band transitions are proposed but further research is needed for gaining the insight and applicability for PV applications.[50]

3. Experimental results of various Metal Halide Lead-free double perovskites

The prominent LFDP of $Cs_2AgBiBr_6$ exhibits promising property such as long carrier lifetime whose synthesis route, optoelectronic properties, carrier dynamics, and defect states are discussed in **Section 3.1.1**. Issues such as indirect and wide bandgap, intrinsic defects, electron-phonon coupling, and ion migration are presented.

The possession of lone-pair electrons of Bi and Sb ion in Cs_2AgBiX_6 and Cs_2AgSbX_6 results into an indirect bandgap leading to an inefficient transition with phonon involved. By replacing the Bi element in $Cs_2AgBiBr_6$ with In, the band structure converts from the indirect to direct nature, as demonstrated in **Section 3.1.2**. The major issue of the IIIA-contained LFDPs is the parity-induced forbidden transition which is ascribed to the electronic configuration of element composition. Such effect leads to a low optical absorption coefficient and weak PL intensity. Strategies of bandgap engineering through elemental substitution, energetic alignment of the frontier orbitals and quantum confinement for nanocrystal are demonstrated to modify the electronic configuration.

Other than $A_2M(I)M(III)X_6$, multi-valence metal double perovskite of $A_2M(IV)X_6$ family has been taken into consideration due to its suitable bandgap and 3D cubic structure. Three members in the $A_2M(IV)X_6$ family are discussed in **Section 3.2** and their application in optoelectronic devices is presented.

Dopants are employed as an effective approach to modify the optoelectronic properties since LFDPs frequently have wide bandgaps. The various dopant, such as Mn, Er, and Yb, doping into the LFDPs alternates the electronic structure and band transition nature. The resultant band structure and the emission profile of LFDPs are modified via different dopants, resulting in effects such as PL shift, dual emission, narrowed band, acceptor states, and defect-induced luminescence.

3.1 $A_2M(I)M(III)X_6$ multi-valence metal double perovskite

3.1.1 $Cs_2AgBiBr_6$ and its relevant compound $Cs_2M(I)M(III)X_6$[M(I) = Cu, Ag; M(III) = Sb, Bi; X = I, Br, Cl]

Theoretical calculations have demonstrated double perovskites as potential candidates for lead-free PSCs with nontoxic and stable nature. The $6s^26p^0$ electronic structure of lead-based perovskite contributed to the material's shallow defect states and long carrier lifetimes, while the high p-orbital-based density of states near the band edges provide for the material's strong absorption.[93] There are three ions have stable cations with the $6s^26p^0$ electronic configuration: Tl^+, Pb^{2+}, and Bi^{3+}. Among the three ions, only Bi^{3+} has low toxicity. Hence, a straightforward idea is to replace Pb^{2+} with Bi^{3+} for double perovskites with charge neutrality and proper crystal structure. In the following sections, experimental results of the widely used double perovskite: $Cs_2AgBiBr_6$ and its relevant compounds will be discussed.

Single crystal $Cs_2AgBiBr_6$ was synthesized by Slavney et al. in 2016 who discovered its noteworthy photovoltaic properties and stability.[37] The precursors containing stoichiometric CsBr, AgBr, and $BiBr_3$ were dissolved in a concentrated HBr solution to crystallize $Cs_2AgBiBr_6$ single crystal under 110 ℃. An indirect bandgap of 1.95 eV was estimated using Tauc plot and a weak PL centered at 1.87 eV was observed. A long carrier lifetime around 660 ns was deduced by time-resolved photoluminescence (TRPL) which was comparable to that of $MAPbI_3$, suggesting that $Cs_2AgBiBr_6$-based PSC could have a decent photovoltaic performance. $Cs_2AgBiBr_6$ single crystal exhibited remarkable stability against moisture, light soaking and heat. The XRD confirmed a stable crystal structure with the material stored either in the dark at 55% relative humidity or irradiated at 50 °C with a broad-spectrum halogen lamp (0.75 Sun) under dry N_2 for 30 days. Moreover, the thermal stability was verified by XRD for sample heated at 100 °C in air for 72 h and thermogravimetric analysis (TGA).

Polycrystalline $Cs_2AgBiBr_6$ and $Cs_2AgBiCl_6$ were synthesized by McClure et al. in 2016 via a solid state route.[23] As-synthesized $Cs_2AgBiBr_6$ and $Cs_2AgBiCl_6$ were formed with a bandgap of 2.26 and 3.00 eV, respectively. As shown in **Table 1**, a significant discrepancy of bandgap values determined from the synthesized $Cs_2AgBiBr_6$ was observed. The discrepancy of the reported bandgap values of

$Cs_2AgBiBr_6$ and $Cs_2AgBiCl_6$ was investigated by Filip et al. via state-of-the-art GW quasiparticle calculations along with experimental measurements.[43] The calculations delivered indirect gaps of 2.4 and 1.8 eV for $Cs_2AgBiCl_6$ and $Cs_2AgBiBr_6$, respectively. These values were in good agreement with the experimental results (2.2 eV for $Cs_2AgBiCl_6$; 1.9 eV for $Cs_2AgBiBr_6$), indicating GW quasiparticle simulation was a reliable tool for predicting bandgap of LFDP.

Indirect bandgap is unfavorable for PV application due to involvement of phonons during the absorption and results in weakly optical absorption.[94] Bandgap engineering was adopted by Du et al. in order to adjust the electronic band structure.[62] The Bi in the B-site was substituted with Sb or In with a maximum amount before phase segregation. The $Cs_2Ag(Bi_{1-x}M_x)Br_6$ (M=In, Sb) showed a phase stability with the In^{3+} content up to 75% or the Sb^{3+} content up to 37.5%. The bandgap was broadened with the incorporation of In^{3+} and narrowed with the incorporation of Sb^{3+}. The atomic substitution enabled the bandgap modulation of 0.41 eV. From the DFT calculations, the shift of bandgap was ascribed to the electronic structure of Sb for Sb-substituted samples. For the In-substituted samples, the In 5s states and the reduced chemical bonds of Bi atoms demonstrated opposite effect on bandgap shift. Upon In substitution, the band transition of $Cs_2Ag(Bi_{1-x}In_x)Br_6$ remained the indirect nature. Moreover, a weak and shifted PL intensity suggested the existence of defects. It is noted that as-synthesized materials delivered a decent stability up to 60 days in the ambient environment.

Due to the wide bandgap of $Cs_2AgBiBr_6$ (>2 eV), Slavney et al. synthesized Cs_2AgTlX_6 (X = Br & Cl) members with a bandgap of 1.96 and 0.95 eV for $Cs_2AgTlCl_6$ and $Cs_2AgTlBr_6$, respectively.[95] The simulation indicated that bandgap transition was attributed to the metal-to-metal charge transition. The crystallized single crystal from concentrated acid solution showed no PL peaks which was ascribed to the symmetry-forbidden transition. Despite the long carrier lifetime (micro-second) and narrow bandgap, the incorporation of Tl still hindered this material from practical use due to its high toxicity of Tl. Alternative metal ion substitution has been demonstrated to the synthesized $Cs_2AgIn_xBi_{1-x}Cl_6$ which displays direct bandgap and improved PLQE.[94] Details of such material will be addressed in **Section 3.1.2**.

Owing to the tunable bandgap, long carrier lifetime and light effective masses, Cs_2AgBiX_6 (X=Br, Cl) double perovskites have been regarded as potential candidates for Pb-free PSCs.[66] Greul et al. firstly demonstrated the fabrication of $Cs_2BiAgBr_6$ thin film with one-step solution process and further integrated it into PSCs. As shown in **Figure 5a**, the spin-coated $Cs_2AgBiBr_6$ was annealed at a temperature above 250 ^oC in order to obtain pure double perovskite phase. As-fabricated thin film was integrated in PSCs composed of fluorine doped tin oxide (FTO)/compact layer TiO_2 (cl-

TiO_2)/mesoporous (mp)-TiO_2/$Cs_2AgBiBr_6$/Spiro-OMeTAD/Au. With the annealing temperature increasing from 25 to 250 °C, the devices received PCE increasing from ~0.5% to above 2%. The champion PSC showed a noteworthy power conversion efficiency of 2.43% with an open circuit voltage (V_{OC}) of 0.98 V, short-circuit current density (J_{SC}) of 3.93 mA/cm^2 and a fill factor (FF) of 0.63 with significant hysteresis. As-fabricated devices showed a stable power output up to 300 minutes and stable PV performance under continuous illumination (AM1.5) up to 100 minutes, indicating a better stability than $MAPbI_3$ counterpart. Moreover, the device performance showed minor variation after storing in the ambient environment without light soaking.

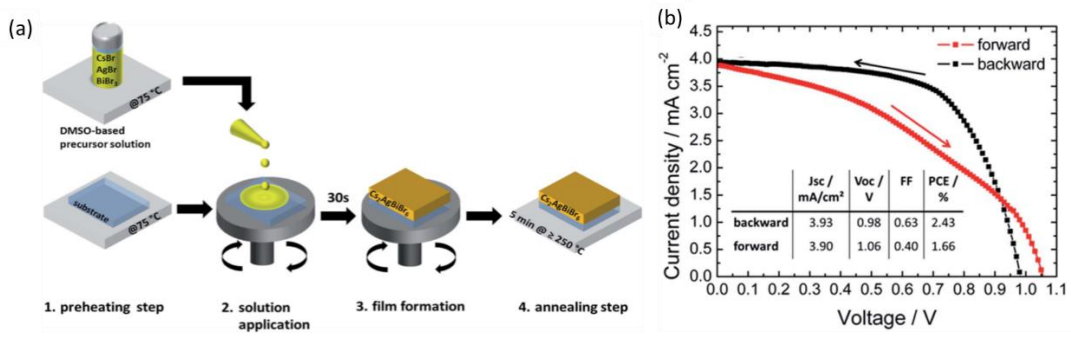

Figure 5. (a) Schematic of the synthesis for $Cs_2AgBiBr_6$ (b) J–V curve of the champion $Cs_2AgBiBr_6$-based cell.[66]

Wu et al. applied low-pressure-assisted deposition in order to achieve uniform thin film with smooth morphology.[74] The synthesized thin film exhibited similar crystal structure, PL emission, and absorption onset with previous reports except for the exciton absorption. It was reported that the annealing temperature affected the PV performance significantly. A champion cell with a planar heterojunction of ITO/SnO_2/$Cs_2AgBiBr_6$/P3HT/Au exhibited a PCE of 1.44% along with a V_{OC} of 1.04 V, a J_{SC} of 1.78 mA/cm^2, and a high FF of 0.78. The device with P3HT showed a rapid degradation within few hours while the device without P3HT stabilized over a month under ambient conditions without any encapsulation, suggesting an instability induced by P3HT.

Ning et al. first demonstrated the planar PSCs employed the one-step solution-processed $Cs_2AgBiBr_6$.[75] A photoexcited carrier diffusion length of ≈110 nm and the coexistence of excitons and free carriers were determined from the TRPL result. PSCs composed of ITO/cl-TiO_2/$Cs_2AgBiBr_6$/Spiro-OMeTAD/Au delivered a best PCE of 1.22% along with a V_{OC} of 1.06 V, a J_{SC} of 1.55 mA/cm^2, and a FF of 0.74. Gao et al. applied anti-solvent treatment to improve the thin film morphology.[96] The film exhibited a carrier trap state density of 9.1x10^{16} cm^{-3} by measuring space charge limited currents (SCLC) and such value was comparable with Pb-based perovskite. The smooth

film was integrated into PSCs composed of ITO/Cu-doped NiO/$Cs_2AgBiBr_6$/C60/BCP/Ag, which was referred as an inverted planar structure. With the application of anti-solvent treatment and optimization of annealing temperature, the PSCs exhibited a maximum PCE of 2.23% with a V_{OC}=1.01 V, a J_{SC}=3.19 mA/cm^2, and a FF=69.2%. The devices retained 90% of its initial PCE over 10 days and showed minor hysteresis. What's worth noting was that the existence of intermediate phase yet to be observed when using DMSO as solvent.

The anti-solvent treatment was also adopted by Pantaler et al., combing with usage of various hole transport layers (HTLs), such as Spiro-OMeTAD, PTAA and PCPDTBT.[76] The n-i-p devices possessed a structure of FTO/cl-TiO_2/mp-TiO_2/$Cs_2AgBiBr_6$/HTM/Au and their representative PV parameters were shown in **Figure 6b**. The champion PSC incorporated with PTAA exhibited a PCE of 1.26%, a V_{OC} of 1.02 V, a J_{SC} of 1.84 mA/cm^2 and a FF of 0.67. Nevertheless, the origin of photovoltaic performance of devices employed different HTL remained to be investigated. The results showed that a minor impact on the performance for the PSCs adopting various HTLs and electron transport layers (ETLs).

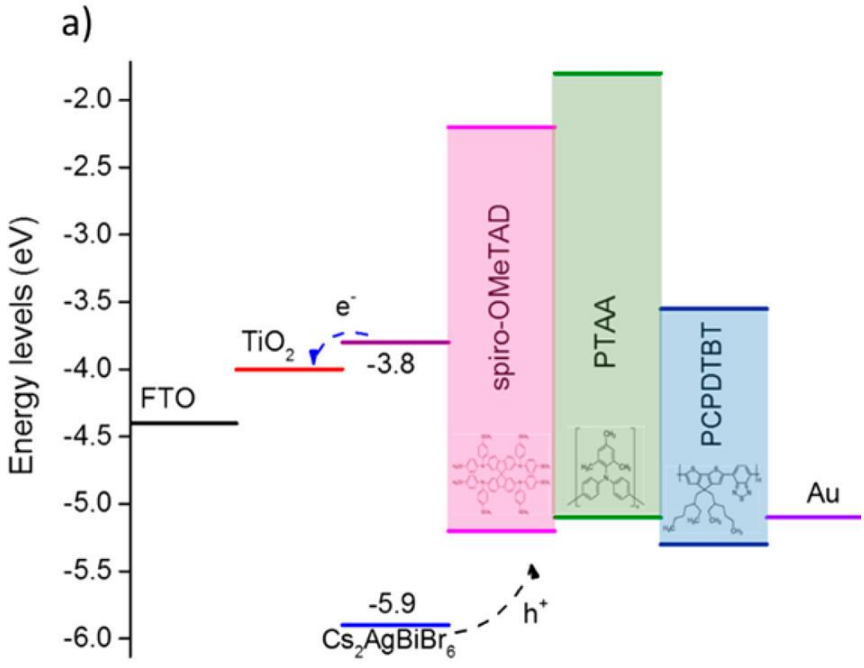

(b)

HTM	J_{SC} (mA/cm^2)	V_{OC} (V)	FF	PCE (%)
PCPDTBT	1.67	0.71	0.57	0.68
spiro-OMeTAD	2.45	0.64	0.57	0.90
PTAA	1.84	1.02	0.67	1.26

Figure 6. (a) Energy level of PSCs contacted with different HTLs. (b) table of PV performance of PSCs based on different HTLs.[76]

Thin film preparation of $Cs_2AgBiBr_6$ evolved from solution process to vapor phase reaction. First report on all vapor deposition was presented by Pantaler et al. using single-, dual- and triple-sources sequential vapor deposition.[97] Nevertheless, as-synthesized double perovskites showed a low phase purity and impurity phases of BiOBr and AgBr were observed by XRD. Similarly, the sequential vapor deposition was employed by Wang et al. to fabricate uniform and smooth double perovskite films.[77] It was reported that excess $BiBr_3$ effectively eliminated the impurities as examined by XRD. As-deposited film delivered diffusion lengths for electron and hole of 147 and 232 nm respectively, which are slightly longer than that of solution-processed $Cs_2AgBiBr_6$. Planar PSCs with an architecture of FTO/cl-TiO_2/$Cs_2AgBiBr_6$/P3HT/Au were fabricated. The top-performed PSCs exhibited a PCE of 1.37% with a noteworthy V_{OC} of 1.12 V and a J_{SC} of 1.79 mA/cm^2. The thin film remained stable up to 10 hours with a temperature of 150 ^{o}C under ambient environment. Moreover, the device retained over 90% of its initial PCE value after 240 hours of storage in dry box. Notably, no hysteresis has been measured for this device structure.

In 2019, both solution process and vapor deposition were employed by Igbari et al. in order to investigate the processes dependence on the photovoltaic properties of $Cs_2AgBiBr_6$-based PSCs.[98] Stoichiometric ratio of solution- and vacuum-processed $Cs_2AgBiBr_6$ thin films was investigated by quantitative X-ray photoelectron spectra (XPS). It was observed that vapor-processed film suffered a larger loss of Br and displayed a wide deviation from expected atomic ratio, while the solution-processed film exhibited an accurate composition stoichiometry. The bromine deficiency might result in point defects which were identified as deep electron traps. The Raman spectra suggested a monotonic relationship between degree of crystallinity, phonon energy, and peak intensity. The solution-processed film exhibited higher crystallinity, narrower bandgap, longer carrier lifetime, and higher carrier mobility than the vapor-processed film.

The solution- and vacuum-processed $Cs_2AgBiBr_6$ thin films were respectively integrated into n-i-p heterojunction PSCs composed of FTO/TiO_2/$Cs_2AgBiBr_6$/Spiro-OMeTAD/MoO_3/Ag.[98] Owing to an well-controlled stoichiometric ratio of solution-processed $Cs_2AgBiBr_6$, the champion device delivered a PCE = 2.51%, a V_{OC} = 1.01 V, a J_{SC} = 3.82 mA/cm^2 and a FF = 0.65. On the other hand, the top performance of vapor-processed device showed a PCE = 1.41%, a V_{OC} = 1.05 V, a J_{SC} = 2.06 mA/cm^2 and a FF = 0.65. The solution-processed $Cs_2AgBiBr_6$ achieved a record efficiency among inorganic double perovskite solar cells. Moreover, a reduced hysteresis was shown by the solution-processed device. Both vacuum- and solution-processed PSCs exhibited a decent stability with 90% of initial PCE retained in ambient without

encapsulation for 15 days. Research efforts are highly encouraged to further enrich the knowledge of this field and to improve the PV performance of double perovskite-based PSCs.

The carrier dynamic of $Cs_2AgBiBr_6$ single crystal was investigated by Bartesaghi et al. via time-resolved microwave conductance (TRMC).[58] The photoconductivity was directly proportional to the product of the charge photogeneration yield, φ and the sum of electron and hole mobility Σμ. With a given charge yield, a lower bound mobility of 1 $cm^2\ V^{-1}\ s^{-1}$ was estimated. On the other hand, the TRMC results exhibited a long-lived tail corresponding to mobile charges with microsecond lifetimes which became dominated with an excitation wavelength near the bandgap. Based on the temperature- and intensity-dependent TRMC results, a shallow trap density state around 10^{16} cm^{-3} in bulk was deduced. Despite the low mobility and high trap density state, the rate of trap-assisted recombination seemed to be slow and the traps are energetically shallow. The carrier kinetic process following the photogeneration of charge carriers close the surface and in the bulk of $Cs_2AgBiBr_6$ single crystal was illustrated in **Figure 7a**.

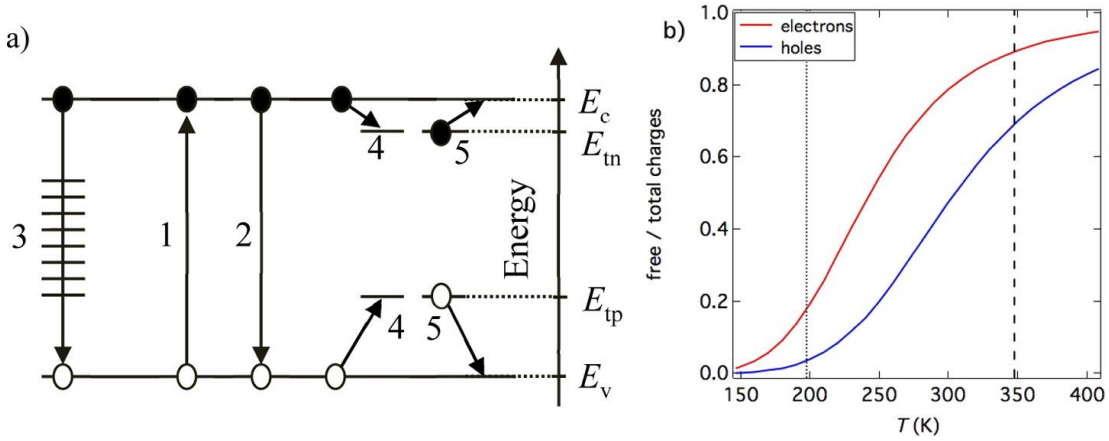

Figure 7. (a) Schematic representation of carrier kinetic within $Cs_2AgBiBr_6$. (1): Generation of free electrons and holes in the conduction (E_C) and valence band (E_V), respectively. (2): Band to band carrier recombination. (3): Surface states recombination. (4) Free charges captured by trap states. (5): Trapped charges was thermally released to the band edges. (b) The ratio of the number of free charges to the total number of charges which stands for the equilibrium distribution of electrons and holes.[58]

Pulse radiolysis time-resolved microwave conductivity (PR-TRMC) was also employed by Hutter et al. to investigate the optoelectronic properties of $Cs_2AgBiBr_6$ and $Cs_2AgBi_{1-X}Sb_XBr_6$ in both powder and film forms.[99] The $Cs_2AgBi_{1-X}Sb_XBr_6$ exhibited a narrowed bandgap of ~1.6 eV upon replacing 40% of the Bi^{3+} with Sb^{3+}. The carrier mobility showed a minor decrease on increasing x. Furthermore, the mobility exhibited a noteworthy dependence on temperature (~ T^{-p}, with p ≈1.5),

indicating a band-like transport of charges in both $Cs_2AgBiBr_6$ and $Cs_2AgBi_{1-X}Sb_XBr_6$. These results addressed that the phonon scattering was the dominant scattering mechanism determining the charge carrier mobility. The substitution of Sb^{3+} was, for the first time, realized via low-temperature solution process to prevent the formation of undesired phase. Moreover, the high trap densities of both $Cs_2AgBiBr_6$ and $Cs_2AgBi_{1-X}Sb_XBr_6$ demanded further optimization for future PV application.

The presence and role of the excitons within $Cs_2AgBiBr_6$ were under debate in the previous reports. Bartesaghi et al. claimed that the exciton effect was a minor issue.[58] On the contrast, Yang et al. reported profound excitonic features and considerable trapping of carrier in $Cs_2AgBiBr_6$ nanoparticles via TRPL and transient absorption (TA) spectroscopy.[100] They further described the negative signals observed in TA spectra around 443 nm as bleach nature which was resulted from defect state-filling effect. On the contrary, Kentsch et al. showed that this negative signal should be explained as the transient broadening of an exciton feature via Femtosecond UV−vis−NIR transient absorption spectra combing with observation of other measurements.[101]

Kentsch et al. conducted a detailed study of $Cs_2AgBiBr_6$ with the employment of femtosecond UV−vis−NIR transient absorption, which enabled the observation of exciton.[101] Additionally, a pronounced coherent oscillation of a strong A_{1g} optical phonon mode of the double perovskite at 177 cm^{-1} was deduced by Fourier amplitude map and verified by DFT calculations. These results suggested a strong electron−phonon coupling via Fröhlich interactions. Similar behaviors were also reported for the related vacancy-ordered perovskite $Cs_3Bi_2Br_9$ and the mother compound $BiBr_3$. Both excitonic effect and electron-phonon coupling were known to result in unfavorable carrier recombination and hinder the carrier transportation. Therefore, an efficient charge extraction at the interface between double perovskites and the carrier transport layer was required.

Despite the achievements of $Cs_2AgBiBr_6$-based PSCs discussed above, the wide bandgap of $Cs_2AgBiBr_6$ restricted the upper limit of PCE. Colloidal Cs_2AgBiX_6 (X = Br and Cl) NCs were first synthesized by Creutz et al..[102] The authors demonstrated the post synthetic modification through anion exchange and cation extraction, which enabled the conversion of novel material (e.g. Cs_2AgBiI_6). This was the first realization of Cs_2AgBiI_6 which showed strong absorption within visible region and a narrowed bandgap of ~1.75 eV which was much smaller than that of bulk $Cs_2AgBiBr_6$. Although theoretical calculations suggested low stability of Cs_2AgBiI_6, the synthesized Cs_2AgBiI_6 NCs through ion-exchange reaction provides an effective method for developing stable iodide-based double perovskites.

Yang et al. also reported the colloidal materials with the synthesis of Cs_2AgBiX_6 (X = I, Br and Cl).[100] Similar optoelectronic properties were observed, such as tunable

bandgap and PL emission wavelength. Notably, the intensity of the PL was increased by 100 times with surfactant (oleic acid) added to passivate the defects.

Nanocrystal is feasible for the study of structural stability since the structural change could be verified via high-resolution transmission electron microscopy (HR-TEM) in the atomic scale.[56] Bekenstein et al. investigated the stability and optical properties of Cs_2AgBiX_6 NCs (X = Br and Cl) by HR-TEM and various optical measurements. Energy-dispersive X-ray spectroscopy (EDS) results of single crystals revealed that the diffusion and coalescence of silver ion led to the formation of $Cs_3Bi_2Br_9$ and Cs_3BiBr_6, and thus degraded the crystals.

3.1.2 $Cs_2AgInCl_6$ and its relevant compound $Cs_2M(I)M(III)X_6$ [M(I)= Cu, Ag; M(III) = Ga, In; X = I, Br, Cl]

The indirect bandgap implied weak oscillator strengths for optical absorption and hence a thicker active layer was needed to reach saturated absorption. When the material possessed low carrier mobility, such thickness effect could greatly reduce the PV performance due to increase of carrier recombination. Inspired by the above works, the development of direct-bandgap double perovskites is in high demand. Volonakis et al. firstly synthesized the $Cs_2AgInCl_6$ via precipitation from an acidic solution of hydrochloric acid.[85] As-synthesized powder of $Cs_2AgInCl_6$ showed an absorption edge at near 380 nm while a peak of PL was observed around 608 nm (2.04 eV). The inconsistency between absorption edge and PL emission was attributed to the parity-induced forbidden transitions. $Cs_2AgInCl_6$ demonstrated excellent stability against moisture, light and heat. Parity-induced forbidden transitions might also lead to low PLQE. In order to break the parity-induced forbidden transition, Luo et al. doped Na into $Cs_2AgInCl_6$ to form alloyed $Cs_2(Ag_{0.60}Na_{0.40})InCl_6$.[22] Because the lattice mismatch between $Cs_2NaInCl_6$ and $Cs_2AgInCl_6$ was as low as 0.30%, Na^+ could be incorporated uniformly into $Cs_2AgInCl_6$ lattice without causing detrimental defects or phase separation. In addition, alloyed $Cs_2(Ag_{0.60}Na_{0.40})InCl_6$ with 0.04 % bismuth doping emitted warm-white light with 86 ± 5 % PLQE and survived for over 1,000 hours. Such phenomena were well explained by the parity-induced forbidden transition as discussed in **Section 2**.

Tran et al. demonstrated that the bandgap nature was tunable based on chemical adjustment.[103] $Cs_2AgSbCl_6$, $Cs_2AgInCl_6$ and $Cs_2AgSbxIn_{1-x}Cl_6$ were synthesized by solid state reaction while the $Cs_2AgSbCl_6$ and $Cs_2AgInCl_6$ single crystals were prepared by hydrothermal method. As-synthesized materials were stable after 4 weeks under the exposure of air and water. Moreover, the bandgap converted from direct to indirect with the increasing of Sb composition. When the s-orbital-derived CBM was transferred to p-orbital-derived CBM with the increasing Sb composition, the bandgap was converted

from indirect bandgap to direct one. The observation above indicated the existence of the lone-pair electrons typically led to indirect bandgaps, and provided an effective strategy for material design.

Abovementioned strategy was further developed by Yang et al. who synthesized $Cs_2AgIn_xBi_{1-x}Cl_6$ NCs with tunable bandgap and improved PLQE.[94] Results suggested that the bandgap converted from indirect to direct nature with increasing In content. With the conversion from indirect bandgap to direct bandgap, the direct transition between VBM and CBM without the participation of phonons resulted in a large absorption cross section. Moreover, a dual color emission was observed at 395 nm (violet) and 570 nm (orange, PLQE: 2%) for $Cs_2AgIn_{0.9}Bi_{0.1}Cl_6$ NCs. The variation of In content resulted in tunable emission and improved carrier lifetime deduced by TRPL with a rapid component corresponding to the intrinsic sub-band gap trapping. The PL excitation spectra verified that the parity-induced forbidden transitions affected absorption only, but not on relaxation of the photoexcited carriers, affording PL with an orange color. Combining the results of PL excitation spectra, DFT calculations, TRPL and transient absorption spectrum, a carrier dynamic model was proposed as shown in **Figure 8**. The chemical adjustment displayed its potential for future material design to achieve efficient and stable PSCs.

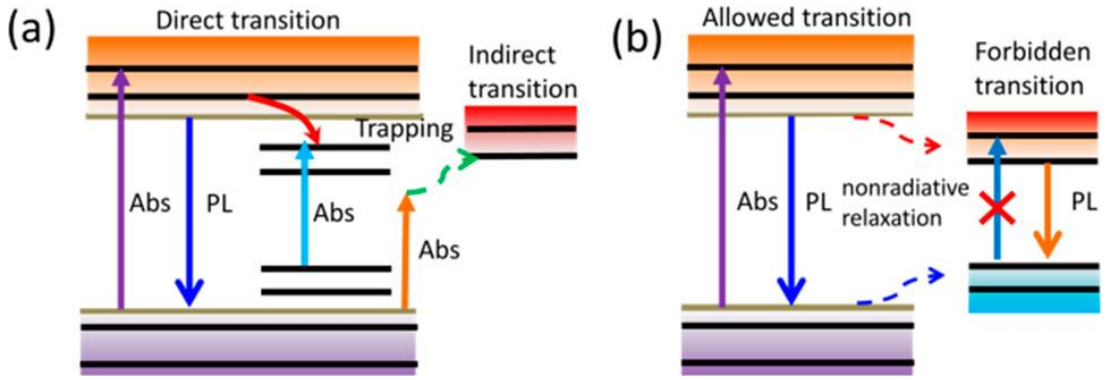

Figure 8. Model of carrier dynamics of (a) $Cs_2AgIn_xBi_{1-x}Cl_6$ (x = 0, 0.25, and 0.5) NCs with indirect bandgap and (b) $Cs_2AgIn_xBi_{1-x}Cl_6$ (x = 0.75 and 0.9) NCs with direct bandgap.[94]

Slavny et al. synthesized $Cs_2(Ag_{1-a}Bi_{1-b})Tl_xBr_6$ by dissolving $Cs_2AgBiBr_6$ in TlBr/HBr solution with careful control of cooling temperature.[61] Even though thallium shows more toxic than lead, Tl-substituted $Cs_2AgBiBr_6$ exhibited comparable bandgap energy and carrier lifetime to those of $CH_3NH_3PbI_3$. In the next year, the same research group developed new double perovskites Cs_2AgTlX_6 (X=Cl and Br) with an optimized synthesis process.[95] They demonstrated a different method for creating small bandgap through the energetic alignment of the frontier orbitals of the B and B'-site metals. The

$Cs_2AgTlCl_6$ and $Cs_2AgTlBr_6$ possessed direct bandgap of 2.0 and 0.95 eV, respectively, which are approximately 1 eV lower than those of analogous perovskites. When Bi^{3+} was replaced with Tl^{3+}, the loss of Bi 6s character decreased the energy of the VBM at the X point while the VB energy at the Γ point was unaffected, resulting in a flat VBM of $Cs_2AgTlCl_6$ along Γ-X direction. Moreover, a decrease of the CBM at Γ point for $Cs_2AgTlCl_6$ yielded a direct gap and reduced bandgap as displayed in **Figure 9**.

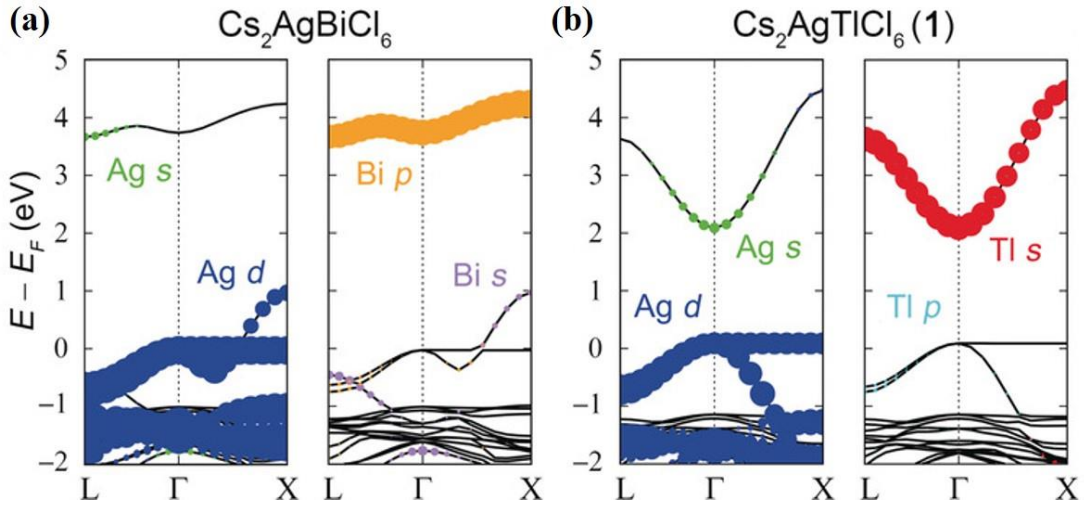

Figure 9. Band structures of (a) $Cs_2AgBiCl_6$ and (b) $Cs_2AgTlCl_6$, calculated with DFT-HSE06+SOC in their primitive unit cells using measured lattice parameters. Band structures are shown in duplicate with only metal orbital contributions shown; chloride orbitals are present but omitted for clarity.[95]

3.2 $A_2M(IV)X_6$: perovskites with M $^{4+}$

3.2.1 Cs_2SnI_6

The crystal structure of $Cs_2SnI_6$is derived from the 3-D perovskite $CsSnI_3$ by removing every second Sn layer along ⟨111⟩. In other words, a 50% Sn deficient perovskite derivative featuring isolated $[SnI_6]^{2-}$ octahedral was illustrated in **Figure 10**.[104] Cs_2SnI_6 was first used in photovoltaic in 2014 by Lee and coworkers.[105] The Sn in the 4^+ oxidation state makes A_2SnI_6 compounds a high-symmetry cubic structure.[106] They successfully used Cs_2SnI_6 as a hole transporter for dye-sensitized solar cell (DSSC) with a structure: FTO /mesoporous TiO_2/dye/Cs_2SnI_6/Pt/FTO. The Cs_2SnI_6 can be deposited by drop-casting and then post-annealing. By optimization the devices with Li-TFSI and TBP additives in Cs_2SnI_6, the maximum IPCE (incident photon-to-electron conversion efficiency) exceeded 74% at 530 nm, 10% higher than that for devices without additives. It is said that the additives reduced interfacial recombination and thus enhanced hole-transport characteristics. In this structure, a Z907/Cs_2SnI_6 DSSC displayed a power conversion efficiency of 4.63%. Using a

mixture of N719 with YD2-o-C8 and RLC5 dyes, extended absorption spectrum further increased the PCE to nearly 8% by improvements in J_{SC} and V_{OC} from 13.2 to 18.6 mA/cm^2 and 0.57 to 0.62 V, respectively.

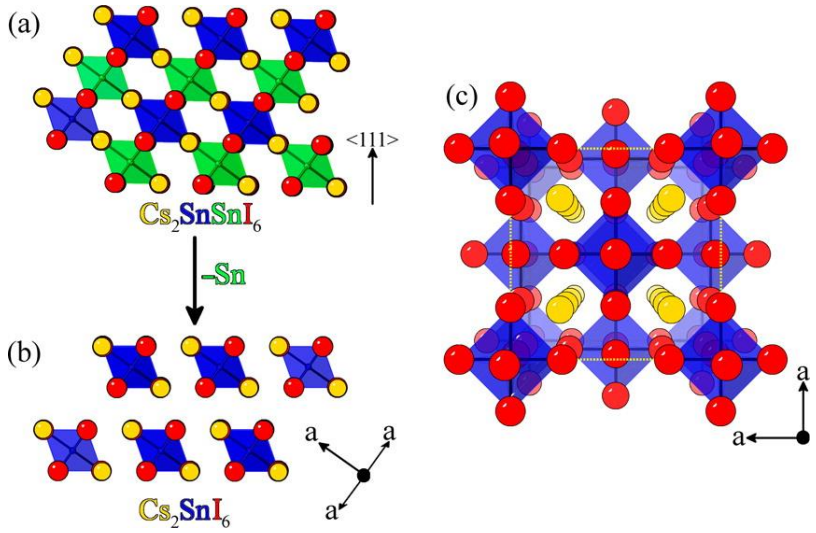

Figure 10. A schematic depiction of the relationship between the crystal structures of (a) the 3-D parent perovskite $Cs_2Sn_2I_6$ (i.e., $CsSnI_3$) and (b) the 0-D Cs_2SnI_6. (c) Perspective view of the crystal structure of Cs_2SnI_6 emphasizing its cubic perovskite-derived crystal structure.[104]

Noticeably, Saparov et al. suggested that Cs_2SnI_6 exhibited insufficient stability and contained intrinsic deep-defects.[104] They used two-step deposition approach to prepare continuous and well-structured Cs_2SnI_6 thin films for analysis. The CsI film was first deposited by thermal evaporation and then underwent annealing at 190 °C in a SnI_4 (excess) atmosphere in the glovebox. In their research, Cs_2SnI_6 films stored in moist air exhibited superior stability than $CH_3NH_3PbI_3$ films stored under similar conditions.[107] The XRD peaks (**Figure 11**) of air-exposed Cs_2SnI_6 film became sharper, similar to what has been observed for $CH_3NH_3PbI_3$ films.[107, 108] Furthermore, the full width at half-maximum (FWHM) value decreased for the main characteristic (222) peaks and a CsI impurity peak appeared when the samples were stored in air after one mouth.

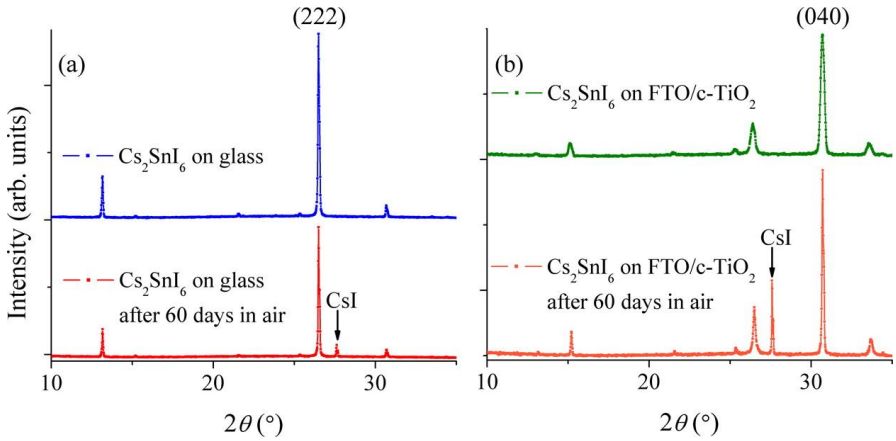

Figure 11. Cs_2SnI_6films deposited on (a) glass and (b) FTO/cl-TiO_2 substrates in ambient air.[104]

Qiu et al. fabricated a lead-free Cs_2SnI_6 and investigated its application for perovskite solar cell.[80] The γ-$CsSnI_3$ film can spontaneously convert into Cs_2SnI_6 film in air at room temperature via the following reaction **Equation 3**:

$$2CsI+2SnI_2+O_2 \rightarrow Cs_2SnI_6+SnO_2 \quad (3)$$

By optimizing the thickness of TiO_2 layer, the resulting Cs_2SnI_6 with a bandgap of 1.48 eV integrated in a planar n-i-p structure obtained a PCE of near 1%. Lee et al. improved the film quality and crystallinity of Cs_2SnI_6 by E-spraying CsI crystalline film and then chemically reacting with spin-coated SnI_4.[83] The photo anode was composed by FTO/cp-TiO_2/2 wt% Sn–TiO_2/$Cs_2SnI_xBr_{6-x}$/solid state HTM of Cs_2SnI_6 and the photo cathode was consisted of large effective-surface-area polyaromatic hydrocarbon (LPAH)/FTO. The two electrodes are then laminated together to achieve a promising V_{OC} of 0.56V, a J_{SC} of 6.23 mA/cm^2, a FF of 0.58, corresponds to a PCE of 2.02% and survived after air-expose for 50 days.

3.2.2 Cs_2PdI_6

Sakai et al.[109] synthesized a new type of lead-free Cs_2PdBr_6 perovskite by in-situ oxidization of Pd^{2+} to Pd^{4+} via solution process. Cs_2PdBr_6 exhibits an optical bandgap of 1.6 eV with electron and hole effective masses of 0.53 and 0.85 m_e, respectively. They further demonstrated the Cs_2PdBr_6–based photodetector using sandwiched structure of ITO/Cs_2PdBr_6/Ag junction under 1 sun illumination. Recently, Zhou et al. reported a photo-electrochemical cell using Cs_2PdBr_6 NCs covered on FTO substrate as photoelectrode.[110] The Cs_2PdBr_6 NCs were formed through a facile microcrystal-mediated antisolvent approach at room temperature. The resultant Cs_2PdBr_6 NCs could further transform to Cs_2PdI_6 NCs via an anion exchange reaction. Such Cs_2PdBr_6 NCs displayed high stability against light illumination (1 sun for more than 1000 h), high moisture (70% for 2 months), and high temperature (120 °C for 600 h). From the

photophysical test in **Figure 12**, transient absorption results indicated intrinsic deep trap states of Cs_2PdBr_6, which corresponded with short PL decay lifetime in TRPL spectra. The ultrafast charge trapping process mainly resulted from the radiative recombination between electrons and holes.[111] The resultant photo-electrochemical cell achieved a photocurrent density of ~1.2 $\mu A/cm^2$ with at an applied potential of 0.65 $V_{Ag/AgCl}$ under 1 sun illumination.

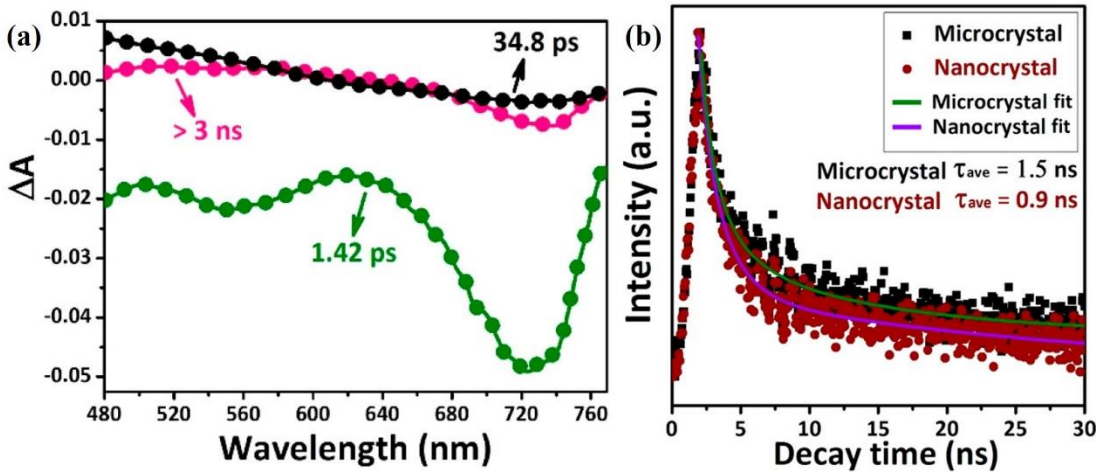

Figure 12. Decay associated spectra for three fitting components from (a) TA spectra, and (b) TRPL spectra of Cs_2PdBr_6.[76]

3.2.3 Cs_2TiI_6

Ju et al. theoretically and experimentally studied the vacancy-ordered double perovskites based on the earth-abundant, nontoxic Ti(IV) element in B-site.[112] They calculated the chemical formula of A_2TiX_6 (in which A = K^+, Rb^+, Cs^+, In^+, MA^+, or FA^+; X = Cl, Br, or I) with suitable bandgaps in the range 1.0 to 1.8 eV by first-principles density functional theory (DFT)calculations. From the thermodynamic, structural and defect simulations, Ti-based perovskites exhibited large decomposition enthalpy values and good intrinsic stability up to high temperatures. (**Figure 13**) In contrast, others transition metals, such as Zr, Hf, V, Nb, Mo, or W, replaced Ti in B-site were predicted to be wide bandgap perovskites and became metallic semiconductor. Based on their calculation, $Cs_2TiI_2Br_4$ and Cs_2TiBr_6 HPs possessed bandgaps of ~1.38 and ~1.78 eV, which are ideal absorbers for perovskite solar cells. Further, the same research group demonstrated the first Ti-based double perovskite solar cells in 2018.[79] They used two step vapor-based method in virtue of thermal evaporation of CsBr reacted with $TiBr_4$ vapor to prepare Cs_2TiBr_6 perovskite thin films. The Ti^{4+} and Br^- ions in $TiBr_4$ were transported from top surface to bottom of the film via solid-state diffusion, resulting in a conversion-reaction from front into the bulk film. A Ti-based double perovskite solar cell with the structure of FTO/ TiO_2/Cs_2TiBr_6/P3HT/Au

showed a J_{SC} of 4.03 mA/cm^2, a V_{OC} of 0.89 V, a FF of 0.63, and a PCE of 2.15%. Introducing C_{60} as an interfacial layer between TiO_2 and Cs_2TiBr_6 active layer pushed the device performance up to 3.22% PCE. In addition, the unencapsulated device maintained 94% of its initial efficiency after 350hr storage time (exposure conditions:70°C, 30% RH, ambient light).

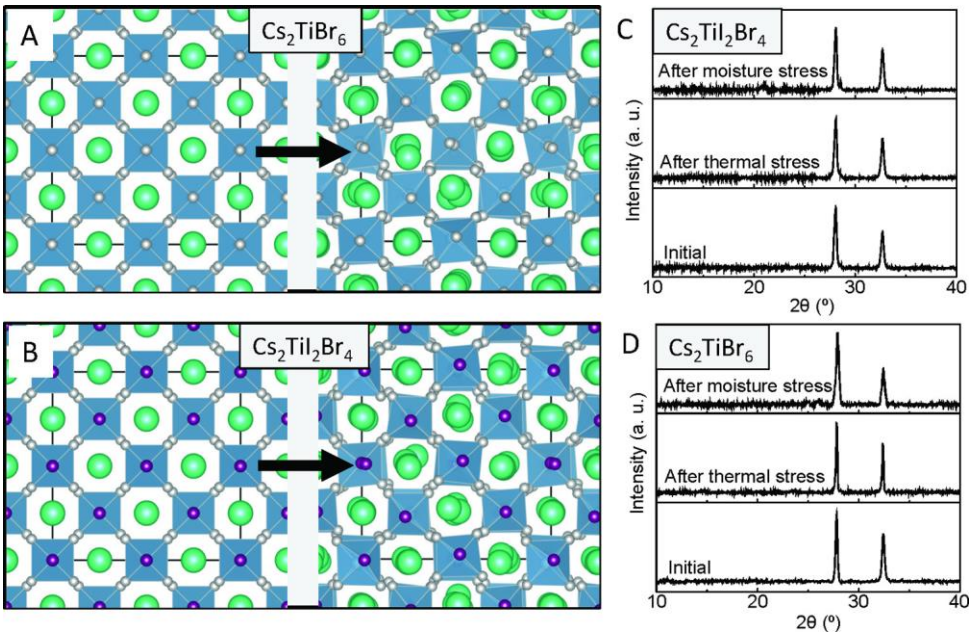

Figure 13. Initial structures (left panels) and snapshots (right panels) of (a) Cs_2TiBr_6 and (c) $Cs_2TiI_2Br_4$ after 5 ps of ab initio molecular dynamic (AIMD) simulations 500K. Experimentally measured XRD patterns of (b) Cs_2TiBr_6 and (d) $Cs_2TiI_2Br_4$ samples before and after exposure to thermal and moisture stresses. For the thermal stability testing, the samples were annealed at 473 K for 1 h. For the moisture stability testing, the samples were stored at 298 K for 4 h under 70% RH.[112]

Table 1. Device architecture and photovoltaic parameters of double perovskite based solar cells

Double Perovskites	**Device Configuration**	**Perovskite Deposition method**	**Voc [V]**	**Jsc [mA/cm^2]**	**FF**	**PCE [%]**	**Ref.**
$Cs_2AgBiBr_6$	ITO/SnO_2/ $Cs_2AgBiBr_6$/P3HT/Au	one-step spin coating & low-pressure assisted method	1.04	1.78	0.78	1.44	[74]
$Cs_2AgBiBr_6$	ITO/SnO_2/ $Cs_2AgBiBr_6$/Au	one-step spin coating & low-pressure assisted method	0.95	1.5	0.6	0.86	[74]
$Cs_2AgBiBr_6$	ITO/Cu-NiO/$Cs_2AgBiBr_6$/C60/BCP/Ag	one-step spin-coating with anti-solvent	1.01	3.19	0.69	2.23	[96]

$Cs_2AgBiBr_6$	FTO/cl-TiO_2/mp-TiO_2/$Cs_2AgBiBr_6$/Spiro-OMeTAD/Au	one-step spin-coating	0.98	3.93	0.63	2.43	[66]
$Cs_2AgBiBr_6$	ITO/cl-TiO_2/$Cs_2AgBiBr_6$/Spiro-OMeTAD/Au	one- step spin-coating	1.06	1.55	0.74	1.22	[75]
$Cs_2AgBiBr_6$	FTO/cl-TiO_2/mp-TiO_2/ $Cs_2AgBiBr_6$/PTAA/Au	one-step spin-coating with anti-solvent	1.02	1.84	0.67	1.26	[76]
$Cs_2AgBiBr_6$	FTO/cl-TiO_2/mp-TiO_2/ $Cs_2AgBiBr_6$/Spiro-OMeTAD/Au	one-step spin-coating with anti-solvent	0.64	2.45	0.57	0.9	[76]
$Cs_2AgBiBr_6$	FTO/cl-TiO_2/mp-TiO_2/ $Cs_2AgBiBr_6$/PCPDTBT/Au	one-step spin-coating with anti-solvent	0.71	1.67	0.57	0.68	[76]
$Cs_2AgBiBr_6$	FTO/cl-TiO_2/$Cs_2AgBiBr_6$/P3HT/Au	sequential-vapor-deposition	1.12	1.79	NA	1.37	[113]
Cs_2NaBiI_6	FTO/cl-TiO_2/mp-TiO_2/Cs_2NaBiI_6/Spiro-OMeTAD/Au	one-step spin-coating	0.47	1.99	0.44	0.42	[78]
Vacancy-ordered double perovskite							
Cs_2TiBr_6	FTO/TiO_2/Cs_2TiBr_6/P3HT/Au	two-step vapor deposition	0.89	4.03	0.63	2.26	[79]
Cs_2TiBr_6	FTO/TiO_2/C60/Cs_2TiBr_6/P3HT/Au	two-step vapor deposition	1.02	5.69	0.56	3.28	[79]
Cs_2SnI_6	FTO/cl-ZnO/mp-ZnO/Cs_2SnI_6/P3HT/Ag	one-step spin-coating	0.52	3.2	0.51	0.86	[82]
Cs_2SnI_6	FTO/cl-TiO_2/Cs_2SnI_6/P3HT/Ag	two-step sequential vapor deposition	0.51	5.41	0.35	0.96	[80]
Cs_2SnI_6	FTO/cl-TiO_2/Cs_2SnI_6/P3HT/Ag	chemical bath deposition	0.25	7.41	0.24	0.47	[81]
$Cs_2SnI_{6-x}Br_x$	FTO/cl-TiO_2/Sn-TiO_2/$Cs_2SnI_{6-x}Br_x$/Cs_2SnI_6 HTM/LPAH/FTO	two-step solution synthesis	0.56	6.22	0.57	2.03	[83]

3.3 Dopant in double perovskite

The electronic orbitals of M'- and M''-site metal dominate the band structure of double perovskite. Most double perovskite materials deliver large bandgap (> 2 eV), indirect bandgap or parity-induced forbidden transition that are not suitable for photovoltaic and optoelectronic applications. An effective strategy for modifying the

optoelectronic properties of double perovskite is by doping impurity cation, such as Mn^{2+}, Cu^{2+}, Bi^{3+}, Yb^{3+} and Er^{3+}, in double perovskite. The pioneer work done by Nandha and Nag demonstrated the Mn-doped $Cs_2AgInCl_6$ double perovskite by adding $MnCl_2$ in the precursor (mixture of AgCl, $InCl_3$ and HCl).[114] CsCl was added in the precursor to form a pale white precipitate. After washing and heating, the resultant powders exhibited white color for pristine and Mn-doped $Cs_2AgInCl_6$ due to their absorption onset close to 350-400 nm. Although $Cs_2AgInCl_6$ double perovskite exhibited direct bandgap, weak PL of $Cs_2AgInCl_6$ at ~619 nm was observed due to the parity-induced forbidden transition resulted from same even parity of VBM and CBM at Γ point. On the contrary, Mn-doped $Cs_2AgInCl_6$ delivered intense PL emission with a shift wavelength at 632 nm which was attributed to charge transfer from $Cs_2AgInCl_6$ host to Mn^{2+} dopant and $^4T_1$ to $^6A_1$ transition (d-d transition) of Mn d electron. However, the spin-forbidden $^4T_1$ to $^6A_1$ transition resulted in a long carrier lifetime (sub-ms to ms timescale). X-band electron paramagnetic resonance (EPR) spectrum further confirmed the Mn^{2+} ions into the lattice of $Cs_2AgInCl_6$.

The first colloidal synthesis of $Cs_2AgInCl_6$ NCs was fabricated by Locardi et al. via hot-injection approach.[115] Metal carboxylate precursors including Ag(ac), $In(ac)_3$ and Cs-oleate were dissolved in diphenyl ether along with co-ligands of oleylamine (OLA) and oleic acid (OA) and sequentially reacted with benzoyl chloride to nucleate and grow NCs under working temperature of 105 °C. A pure phase of cubic NCs of $Cs_{2.5}Ag_{0.9}In_{1.1}Cl_6$ stoichiometry with an average size of 9.8 nm was obtained from the ICP, XPS and TEM measurements. The as-synthesized $Cs_2AgInCl_6$ NCs showed a weak and broad PL emission at 560 nm which was blue shift as compared to the previous work (PL at 619 nm) due to quantum confinement effect. Furthermore, the $Cs_2AgInCl_6$ NCs presented remarkable environmental-stability in air and thermal-stability up to 500 °C. To further enhance the PL emission, $Mn(ac)_2$ was added in the above mixture with a doping levels of 0.2%. Inclusion of Mn ions in $Cs_2AgInCl_6$ NCs was proven by XRD and EPR spectroscopy which led to a PL emission at 620 nm.

Similarly, Liu et al. employed facile hot-injection to synthesize $Cs_2AgInCl_6$ and Bi-doped $Cs_2AgInCl_6$ NCs, for which $AgNO_3$, $InCl_3$ and $BiCl_3$ were dissolved in hydrochloric acid (HCl) and octadecene (ODE) together with ligands (OA and OLA) reacted at desired temperature.[116] Hot Cs-oleate was sequentially injected into the precursor. Full crystallization of double perovskite NCs with high crystallinity was obtained at temperature of 280 °C. The amounts of ligands and hydrochloric acid were optimized to prevent impurity or second phases formation during synthesis. The absorption onset of $Cs_2AgInCl_6$ NCs was around 350 nm which was corresponding to an optical bandgap of 4.25 eV, while the absorption onset of Bi-doped $Cs_2AgInCl_6$ NCs was shifted to 390 nm with corresponding optical bandgap of 3.28 eV (referred to

Figure 14(a)). The PL spectra of undoped and Bi-doped NCs excited by 368 nm exhibited a weak blue emission at 470 nm and broad orange emission centered at 580 nm, respectively. Mismatch between absorption and PL emission of $Cs_2AgInCl_6$ NCs mainly originated from the parity-induced transition and defect states as revealed in Fig. 15(b) (transition 1). First two valance states of VBM and VBM-1 at Γ point had the same parity with CBM, resulting in forbidden transition. The opposite parity of third valance state (VBM-2) to CBM allowed the optical transition from VBM-2 to CBM which assigned to the optical bandgap of 4.25 eV. With Bi doping in $Cs_2AgInCl_6$ NCs, the optical bandgap is comparable with electronic bandgap presumably due to the release of parity-induced forbidden transition by Bi cation or surface states passivation. (referred to transition 2 in Fig. 15(b)) Moreover, Bi cation would serve as an acceptor to receive the electron from $Cs_2AgInCl_6$ which underwent optical transition with an emission wavelength centered at 580 nm.

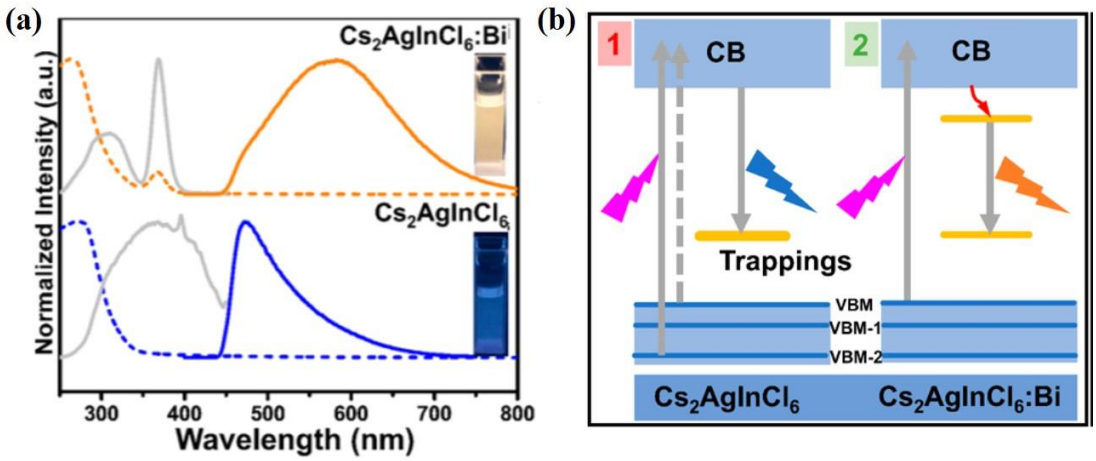

Figure 14. (a) Normalized UV-Vis absorption (dash), photoluminescence excitation (emission at 580 nm for Bi-doped NCs and 470 nm for undoped NCs) spectra (gray) and PL spectra of pristine and Bi-doped $Cs_2AgInCl_6$ NCs (solid orange and blue lines). Insets show the respective colloidal suspension under 365 UV lamp. (b) Transition path of pristine and Bi-doped $Cs_2AgInCl_6$ NCs.[116]

Lee et al. introduced lanthanide of Er^{3+} and Yb^{3+} to replace In^{3+} in $Cs_2AgInCl_6$ to modulate the PL emission from visible to infrared/near-infrared wavelength.[117] The $Cs_2AgInCl_6$ NCs as well as Er-doped, Yb-doped and Er/Yb doped $Cs_2AgInCl_6$ NCs were prepared by solvothermal approach. The Yb-doped $Cs_2AgInCl_6$ shown a sharp PL peak at 996 nm due to the f-band transition of Yb ($^2F_{5/2}$ to $^2F_{7/2}$), while the Er-doped $Cs_2AgInCl_6$ presented a sharp PL peak at 1537 nm in virtue of the f-band transition of Er ($^4F_{13/2}$ to $^4F_{15/2}$). The defective trapped states in doped $Cs_2AgInCl_6$ NCs led to

incapable energy transfer from $Cs_2AgInCl_6$ to lanthanide dopants. Similarly, Chen et al. doped Yb^{3+} in the $Cs_2AgBiCl_6$ and Cs_2AgBiI_6 NCs via hot injection method to produce a dual emission profiles which was opposite to the results of last work.[118] In addition to the intrinsic trap states induced visible PL emission (~680 nm) of undoped double perovskite, $^2F_{5/2}$ to $^2F_{7/2}$ f-f transition produced a near-infrared emission at ~1000 nm, implying the energy transfer from $Cs_2AgBiCl_6$ or Cs_2AgBiI_6 to Yb^{3+} dopant.

Tan et al. introduced Bi^{3+} cation as impurity dopant in Cs_2SnCl_6 double perovskite whose ionic radius and electronic configuration of $4f^{14}5d^{10}6s^2$ is similar to Pb^{2+}.[119] Cesium chloride, tin chloride and bismuth chloride dissolved in HCl aqueous solution underwent hydrothermal reaction to produce Bi-doped Cs_2SnCl_6 powders. From the inductively coupled plasma optical emission spectrometry (ICP-OES), XRD and XPS, partial Bi was successfully incorporated into Cs_2SnCl_6. Undoped Cs_2SnCl_6 presented an optical absorption edge at 315 nm corresponding to an optical bandgap of 3.93 eV. Upon Bi doping, an additional absorption peak at ~400 nm was detected which was presumably resulted from the transition from CBM (Sn 5s orbital) to VBM' (hybrid Cl 3p/Bi 6s orbital) as shown in **Figure 15**. As a result, the bandgap of Cs_2SnCl_6 significantly reduced from 3.9 to 3.0 eV. (referred to **Figure 16(c)**) As examined from PL excitation spectra, no energy transfers between host Cs_2SnCl_6 and Bi was observed. Thermodynamically preferred defect complex of Bi_{Sn} (Bi-on-Sn substitution) and V_{Cl} (vacancy defect of Cl) in Bi-doped Cs_2SnCl_6 presumably served as the luminescent centers which was responsible for the strong blue emission.

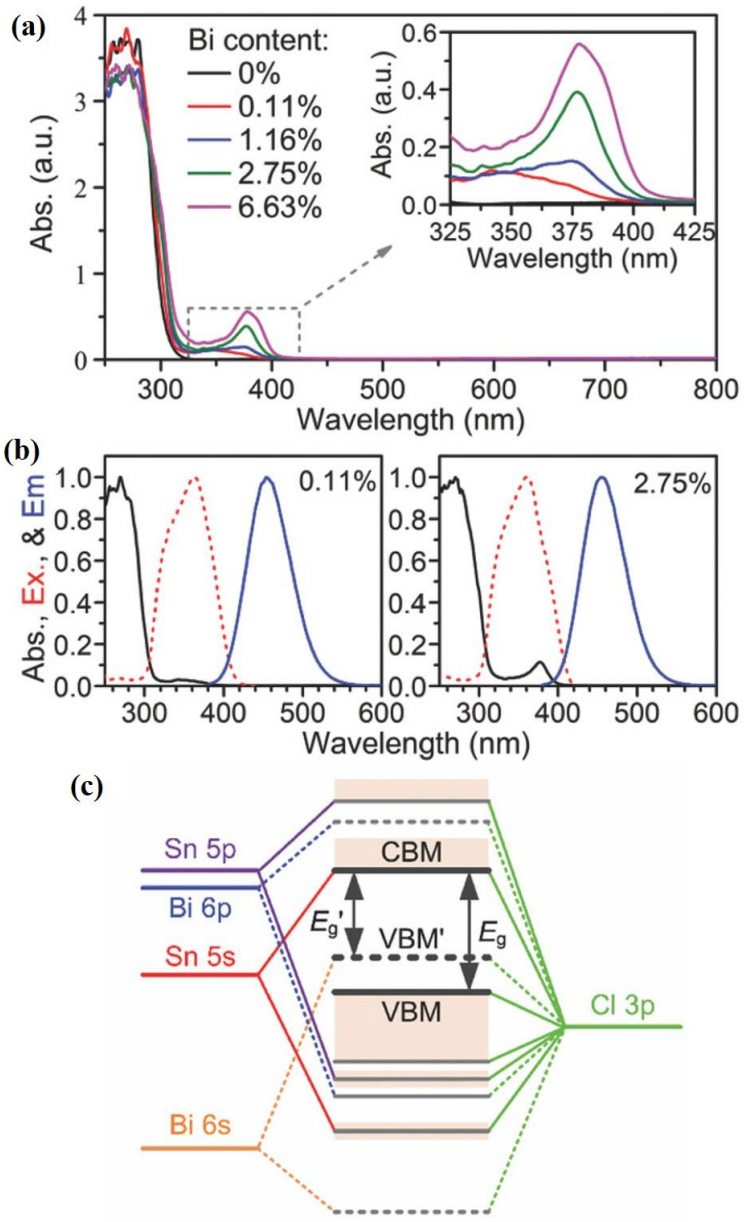

Figure 15. (a) UV-Vis absorption spectra of Bi-doped Cs_2SnCl_6 double perovskite. (b) Normalized absorption (black), excitation (red) and emission (blue) spectra of 0.11% Bi-doped Cs_2SnCl_6 (left) and 2.75% Bi-doped Cs_2SnCl_6. (c) Schematic energy diagram for Bi-doped Cs_2SnCl_6.[119]

$Cs_2SbAgCl_6$ double perovskite exhibits large bandgap with indirect band transition which are assigned to the VBM of Sb 5s/Ag 4d hybrid orbital and CBM of Sb 5p orbital. Karmer et al. proposed that incorporation of $3d^9$ orbitals metal cation in double perovskite can narrow the bandgap.[120] They introduced heterovalent Cu^{2+} cation in $Cs_2SbAgCl_6$ double perovskite which significantly reduced the bandgap from 2.6 eV (pristine $Cs_2SbAgCl_6$) to 1 eV (Cu-doped $Cs_2SbAgCl_6$). The Cu^{2+} preferentially substituted for Ag^+ in the double perovskite which caused microstrain structural defects due to lower ionic radius of Cu^{2+} compared to Sb^{3+} and Ag^+. Low doping level of Cu^{2+}

in $Cs_2SbAgCl_6$ would induce localized impurity states near the band edges which narrowed the bandgap. The Cu-doped $Cs_2SbAgCl_6$ demonstrated long-term structural and photophysical stability under thermal and moisture exposure.

Majher et al. doped Mn^{2+} into the $Cs_2NaBiCl_6$ double perovskite which presented a broad PL emission centered at 590 nm as shown in **Fig. 16**.[121] It is noted that dominant two peaks in the excitation spectrum in Fig. 17 were corresponding to the $6s^2 \rightarrow 6s^1p^1$ transition of Bi^{3+} ions, including spin-forbidden $^1S_0 \rightarrow {}^3P_2$ transition (294 nm) and spin-forbidden $^1S_0 \rightarrow {}^3P_1$ transition (354 nm). The $Cs_2NaBiCl_6$ double perovskite exhibited a weak PL at 730 nm. When Mn^{2+} was doped into $Cs_2NaBiCl_6$ double perovskite, energy transfer from Bi^{3+} to Mn^{2+} activators lead to an emission peak at 590 nm via the spin-forbidden $^4T_1 \rightarrow {}^6A_1$ transition of octahedrally coordinated Mn^{2+}.

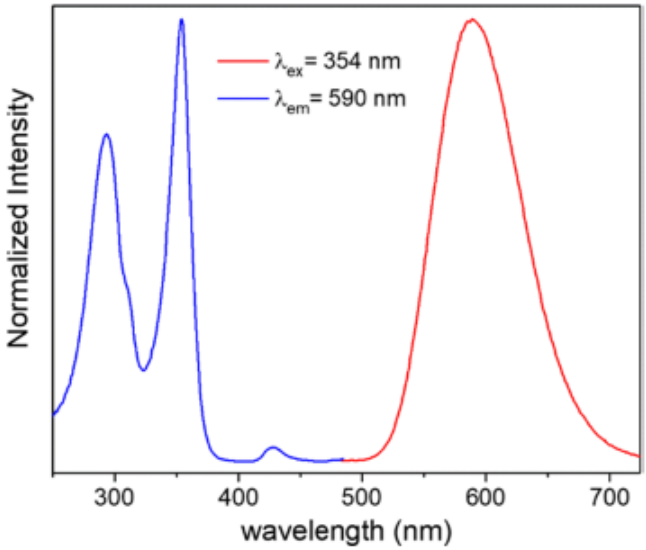

Figure 16. Excitation (blue) and emission (red) spectrum scanned for excitation wavelength at 375 nm for Mn-doped $Cs_2NaBiCl_6$ double perovskite.[121]

3.4 Concluding remarks:

Simple fabrication process and suitable optoelectronic properties allow $CsAgBiBr_6$ to be widely investigated in terms of PV application. Despite the maximum PCE of $CsAgBiBr_6$-based solar cells is limited to 8%, the decent stability and the low toxicity of $CsAgBiBr_6$ still attract noteworthy attention. Nevertheless, concerns about the indirect bandgap originated from the existence of lone-pair electron from VA groups, the large trap density, exciton effect, and the electron-phonon coupling hinder its application in solar cells.

The different synthesis routes of $CsAgBiBr_6$ could result in a different stoichiometric ratio. Moreover, the detailed crystallization mechanism during various synthesis remains unclear. Nucleation and crystal growth kinetic could be well-

controlled to create high-quality LFDP film. Large trap states in $CsAgBiBr_6$ perovskite quench the PL intensity. Obtaining high-quality LFDP film with reduced trap states is needed. It is noted that high-temperature annealing for $CsAgBiBr_6$ perovskite significantly improves the solar cell performance; however, the mechanism is still under debate. A further enhancement in photovoltaic performance could be realized by employing the $CsAgBiI_6$ which exhibits a suitable bandgap of 1.75 eV after improving its intrinsic instability.

The direct bandgap of $CsAgInX_6$ and its relevant compounds avoid the electron-phonon coupling in indirect-bandgap Bi-based LFDPs. Nevertheless, the parity-induced forbidden transition resulting from the IIIA group elements significantly gives rise to low absorption and a low quantum efficiency which affects the device performance. Bandgap engineering has shown to be an effective method for modulating bandgap with direct band transition instead of parity-induced forbidden transition. Replacing Bi, Sb or In with Tl has been demonstrated to change the band transition despite the high toxicity of Tl. Tunable optoelectronic properties can be achieved by different dopants. For instance, various dopants, including Mn^{2+}, Cu^{2+}, Er^{3+}, and Yb^{3+} are also applied to alternate the band structure and PL emission profile. Despite research progresses have been made on the Cs_2AgInX_6/Cs_2AgBiX_6 family, development of LFDPs other than Cs_2AgInX_6/Cs_2AgBiX_6 is highly demanded to overcome the intrinsic issues of LFDP-based PSCs.

The carrier transport layer plays an important role in the whole device to effectively extract carrier from LFDPs active layer. Only a few candidates of the carrier transport layer have been incorporated into LFDPs-based PSCs. Nevertheless, the reaction chemistry, defects, and carrier dynamic at perovskite/carrier transport layer interface carrier are rarely discussed. On the other hand, the transport layers with suitable energy levels, environmental stability, high transparency, high mobility and high-temperature tolerance for post-annealing also require further investigation.

4. Beyond the scope of lead-free double perovskite solar cells

4.1 Other Application of double perovskites

Although LFDPs have shown their success on photovoltaic, their electronic structure mentioned above limits the device efficiency. Beyond the solar cells, researches also focus on other optoelectronic applications, such as photocatalytic, thermochromism, light emitting diode, photodetector, and X-ray detector, due to their simple synthesis, eco-friendly content and environmental stability of halide double perovskites. This section briefly summarizes the extensive optoelectronic applications based on the halide double perovskite.

4.1.1 Photocatalytic

Zhou et al. synthesized high-quality $Cs_2AgBiBr_6$ double perovskite NCs via the hot-injection method.[59] Small amount of hydrobromic acid (HBr) was added in the precursor to ensure a full ionization of Ag^+ cation which prevented the AgBr impurity residual in the final product. Moreover, co-ligands of OA and OLA, and the reaction temperature were controlled for the synthesis of $Cs_2AgBiBr_6$ NCs. The as-fabricated NCs after washing exhibit remarkable stability in terms of stable structure in low polarity solutions (up to 3 weeks), phase uniformity against moisture (55% RH), light-soaking stability (under 70 mW cm^{-2} illumination for 500 hr) and thermal stability (heating at 100°C for 300 hr).

The $Cs_2AgBiBr_6$ NCs had a suitable conduction band to undergo a photochemical conversion of CO_2 into solar fuels. Ligand-enclosed NCs would hamper the photogenerated charges transport across the ligand and reduce the photocatalytic performance. In addition, photoconversion products easily accumulated in the ligand sheet, resulting in catalyst poisoning and decrease in activity. Hence, low ligand density of washed NCs was benefit to the high photoconversion performance due to the efficient charge transfer efficiency. Total electron consumption of 105 μmol g^{-1} for CO_2 reduction reaction was demonstrated under AM 1.5G illumination (150 mW cm^{-2}) for 6 hr, rendering $Cs_2AgBiBr_6$ double perovskite as environmentally friendly photocatalysts.

4.1.2 Thermochromism

More recently, Ning et al. demonstrated a thermochromic lead-free halide $Cs_2AgBiBr_6$ double perovskite in the form of single crystal and thin film whose bandgap can be modulated by temperature.[122] Reversible bandgap modulation of $Cs_2AgBiBr_6$ double perovskite, after heating/cooling test under ambient condition, delivered its thermal and environmental stability. Ab initio molecular dynamic simulation suggested that anharmonic fluctuations of Ag-Br and Bi-Br bonds, strong electron-phonon coupling, and strong spin-orbit coupling were responsible for the thermochromic effect. Stable and thermochromic double perovskite was promising for the applications of smart windows, temperature sensors, and visual thermometers.

4.1.3 Light emitting diode

$Cs_2AgInCl_6$ double perovskite is a promising emission material for the LED in terms of its direct bandgap, nontoxicity, broad spectrum (~400-800 nm), thermal and environmental stability. However, it suffers from low PLQE, especially in red wavelength, due to the parity-induced forbidden transitions and self-trapped exciton. Locardi et al. synthesized $Cs_2AgInCl_6$ NCs via colloidal hot-injection approach.[115] The

resultant $Cs_2AgInCl_6$ NCs showed a broad PL emission at 560 nm with a low PLQE of ~1.6±1%. The PLQE was further improved to ~16±4% by doping Mn^{2+} in $Cs_2AgInCl_6$ NC. PL emission of Mn-doped $Cs_2AgInCl_6$ NCs shifted to orange emission at 620 nm due to the $^4T_1 \rightarrow {}^6A_1$ transition of Mn^{2+} dopant.

Yang et al. synthesized In-alloyed $Cs_2AgBiCl_6$ NCs by antisolvent recrystallization which can be tuned from indirect to direct bandgap with variant In content.[94] Synthesized $Cs_2AgIn_{0.75}Bi_{0.25}Cl_6$ and $Cs_2AgIn_{0.9}Bi_{0.1}Cl_6$ NCs exhibited direct bandgap, 3 times greater absorption cross section, lower sub-bandgap trap-states and >5 times PLQE compared to indirect bandgap NCs of $Cs_2AgBiCl_6$. The $Cs_2AgIn_{0.9}Bi_{0.1}Cl_6$ NCs presented dual color emission originating from direct band-to-band transition (violet, PLQE=36.6%) and parity-induced forbidden transition (orange, PLQE=2%).

Liu et al. applied facile hot-injection with a green synthetic approach (without harmful reagents) to prepare $Cs_2AgInCl_6$ and Bi-doped $Cs_2AgInCl_6$ NCs. [116] The synthesis condition including synthesis temperature, amounts of ligands and hydrochloric acid were well-controlled to optimize their structures and optical properties. The Bi-doped $Cs_2AgInCl_6$ NCs delivered a broad orange emission at 580 nm with 11.4% PLQE. Majher et al. doped Mn^{2+} into the $Cs_2NaBiCl_6$ double perovskite to prepare orange-red phosphor with a broad emission centered at 590 nm (PLQE~15%).[121] Bi^{3+} ions in the host $Cs_2NaBiCl_6$ absorbed near-UV light which undergoes energy transfer fromBi^{3+} to Mn^{2+} activators, resulting in an emission peak at 590 nm via the spin-forbidden $^4T_1 \rightarrow {}^6A_1$ transition of octahedrally coordinated Mn^{2+}.

The synthesized double perovskite NCs are potential phosphor for LED. The full LED device was demonstrated by Tang et al. who introduced impurity doping of Bi^{3+} in the host Cs_2SnCl_6 double perovskite.[119] The Bi-doped Cs_2SnCl_6 exhibited a deep-blue emission at 455 nm with a high PLQE of 78.9%. The thermodynamically preferred defect complex of Bi_{Sn} + V_{Cl} (vacancy defect) in the Bi-doped Cs_2SnCl_6 was presumably responsible for the strong blue emission. The synthesized Cs_2SnCl_6:Bi double perovskite presented excellent resistance against water corrosion due to the formation of BiOCl as a protective layer on the surface. Moreover, Cs_2SnCl_6:Bi also demonstrated an impressive thermal stability which was ascribed to its large decomposition enthalpy. The LED device integrated Cs_2SnCl_6:Bi phosphors with commercial yellow phosphors and ultraviolet LED chip delivered a warm-light emission with a correlated color temperature of 4486 K and Commission Internationale de L'Eclairage (CIE) coordinate of (0.36, 0.37).

The same group alloyed sodium cations into $Cs_2AgInCl_6$ double perovskite to break the inversion symmetry induced parity forbidden transition and reduce the electronic dimensionality.[22] Alloyed $Cs_2(Ag_{0.6}Na_{0.4})InCl_6$ presented an enhanced

photoluminescence efficiency by three orders of magnitude compared to pristine $Cs_2AgInCl_6$ double perovskite. Further Bi^{3+} doping in $Cs_2(Ag_{0.6}Na_{0.4})InCl_6$ improved crystal perfection and promoted exciton localization, leading to an optimized PLQE of 86±5% with an emission wavelength centered at 550 nm. The as-fabricated powder integrated with commercial ultraviolet LED chip emitted warm-white light with a correlated color temperature of 4.054 K and a CIE coordinate of (0.396, 0.448) which reached the requirements for indoor lighting. The LED device without encapsulation also delivered outstanding stability when operated at ~5,000 cd m^{-2} for over 1,000 hr under ambient condition.

4.1.4 Photodetector

Tang' s group introduced the one-pot hydrothermal approach to grow high-quality $Cs_2AgInCl_6$ single crystals which exhibited a low trap-state density of 8.6×10^8 cm^{-3}.[88] $Cs_2AgInCl_6$ single crystals showed two absorption edges at 384 and 595 nm that were corresponding to the band-to-band transition (from CBM to VBM_2) and parity-induced forbidden transition (from CBM to VBM), respectively. The strong absorption wavelength lower than 400 nm of $Cs_2AgInCl_6$ made it promising for UV-light detection. A stable UV detector based on the photoconductive planar structure was demonstrated with a responsivity of ~0.013 A W^{-1}, on/off photocurrent ratio of ~500, fast photoresponse of ~1 ms, and high detectivity of ~10^{12} Jones.

Lei et al. prepared $Cs_2AgBiBr_6$ thin film by the one-step spin-coating method as a light absorber for photodetector based on the photoconductive planar structure.[123] The as-fabricated device exhibited a high responsivity of 7.01 A W^{-1}, on/off photocurrent ratio of 2.16×10^4, fast response time of ~ 1 ms, and detectivity of 5.66×10^{11} Jones. The photodetector without encapsulation also demonstrated remarkable ambient stability. Wu et al. fabricated a photovoltaic-type photodetector with an ITO/SnO_2/$Cs_2AgBiBr_6$/Au planar heterojunction in which $Cs_2AgBiBr_6$ film was prepared via the low- pressure assisted solution process.[124] The built-in field at $Cs_2AgBiBr_6$/SnO_2 interface facilitated the photogenerated carrier separation, rendering its outstanding photodetection performance than other photodetectors based on semiconductor oxide heterojunction. The resultant device without encapsulation was self-powered because of the photovoltaic architecture and suitable for UV and deep-blue light detecting with a responsivity of 0.11 A W^{-1} (at 350 nm), fast response time of 2 ms, specific detectivity of 2.1×10^{10} Jones and long-term stability.

Zhou et al. fabricated narrowband photodetectors based on a photoconductive structure which employed millimeter-sized $Cs_2SnCl_{6-x}Br_x$ single crystals by hydrothermal method.[125] The response spectra of photodetectors can be continuously tuned from near violet to orange by changing the halide composition as well as the

bandgap of synthesized single crystals. The narrowband photodetection was attributed to the strong surface charge recombination near the crystal surfaces. The device exhibited narrowband photodetection with FWHM of ~45 nm, high detectivity of 2.71×10^{10} Jones and satisfying moisture resistance.

Li et al. demonstrated a self-powered photodetector utilizing solution-processed double perovskite Cs_2AgBiI_6 with a photovoltaic architecture of In/GaN/Cs_2AgBiI_6/Ag.[126] Cs_2AgBiI_6 double perovskite contacted with n-type GaN produced a built-in electrical field at Cs_2AgBiI_6/GaN interface which effectively separated the photogenerated exciton and facilitated electron extraction by GaN. Impressive photodetection performances including high on/off photocurrent ratio of 4.16×10^4, high photoresponsivity of 1.46 A W^{-1}, and a specific detectivity of 9.4×10^{13} Jones were demonstrated. The unencapsulated photodetector also delivered remarkable thermal and environmental stability when the device was continuously operated under a relative humidity of 35~50% and 100°C. The photodetector was further applied as sensing pixels for image system and provided a high-resolution imaging pattern.

Ghosh et al. synthesized Cs_2SnI_6 nanoparticles with three morphologies, namely nanosheet, nanocube, and nanorod, using the hot-injection process.[127] When the dimension of Cs_2AgBiI_6 was reduced from 2D (nanosheet), 1D (nanorod) to 0D (nanocube), quantum confinement effect had a significant impact on the bandgap increasing from 1.375, 1.41 to 1.48 eV, respectively. Colloidal inks of nanosheet, nanocube and nanorod were spin-casting onto the patterned ITO substrate to fabricate a photodetector with photoconductive structure. Nanorod-based photodetector exhibited on/off photocurrent gain of 475 and response time of ~1 s whereas nanosheet-based one had the maximum responsivity and detectivity.

4.1.5 X-ray detector

Indirect bandgap of $Cs_2AgBiBr_6$ limits its application on photovoltaic and lighting applications. However, its high X-ray absorption coefficient (due to the existence of heavy element of Bi), high carrier lifetime (due to indirect transition) and efficient charge extraction, high resistivity (10^9-10^{11}Ω cm for $Cs_2AgBiBr_6$ single crystal), low ionization energy and high X-ray detection (due to reduced filed-driven ionic migration) make it as a promising X-ray detector.

Tang's group demonstrated sensitive X-ray detectors with low detection limit using solution-processed $Cs_2AgBiBr_6$ double perovskite single crystal.[128] Elimination of Ag^+/Bi^{3+} disordering in the single crystal was achieved by thermal annealing and surface treatment (isopropanol or ethylacetate rinse) to improve the carrier transport and decrease the surface trap density along with crystal resistivity. Moreover, high migration barrier of $Cs_2AgBiBr_6$ single crystals effectively suppressed the ion

migration which allowed a large external bias and was beneficial for efficient charge collection without increase in noise current. The resultant X-ray detector demonstrated a high sensitivity of 105 μCGy_{air}^{-1} cm^{-2} with a low detectable dose rate of 59.7 nGy_{air} s^{-1} under a bias of 5V.

Li et al. embedded $Cs_2AgBiBr_6$ double perovskite in a polymer matrix as a composite film for X-ray detector.[129] Polymer of poly(vinyl alcohol) (PVA) with hydroxyl functional group improved the aggregation of $Cs_2AgBiBr_6$, resulting in a flexible, dense and uniform film with large area via drop-casting method. The flexible X-ray detector was fabricated by sandwiching $Cs_2AgBiBr_6$ composition film with two gold electrodes. The device exhibited a sensitivity of 40 μCGy_{air}^{-1} cm^{-2} at bias of 400 V without degradation after flexing/bending test. The authors also demonstrated the concept of pixelated X-ray imager to serve as X-ray image sensing device.

Yuan et al. introduced phenylethylamine bromide (PEABr) to in-situ modulate $[BiX_6]^{3-}$ and $[AgX_6]^{5-}$ octahedral disordering in $Cs_2AgBiBr_6$ single crystal.[130] The regulation of order-disorder phase effectively decreased the defect density and increased the carrier mobility which gave rise to suppression of self-trapped exaction formation. Eventually, the X-ray detector based on a photoconductive structure of Au/PEA-treated $Cs_2AgBiBr_6$/Au performed better than pristine $Cs_2AgBiBr_6$-based device with fast response (τ_{rise}= 24 μs, and τ_{decay}=13 μs) and high sensitivity of 288.8 μCGy_{air}^{-1} cm^{-2} at 50 V bias voltage. Double perovskites using trivalent lanthanide, namely $Cs_2NaTbCl_6$ and $Cs_2NaEuCl_6$, were synthesized by Hu et al. by using the hydrothermal process.[131] Typical f-f transition of lanthanide cations makes $Cs_2NaTbCl_6$ and $Cs_2NaEuCl_6$ exhibit strong green and weak red photoluminescence, respectively. High light yield of $Cs_2NaTbCl_6$ of 46600 photons MeV^{-1} under X-ray radiations allowed its applications in detecting high energy radiations and medical imaging.

Other material properties of emerging lead-free double perovskite, such as piezoelectricity, triboelectric effect, nonlinear optical effect, and magnetism effect, are required to be further investigated. These properties are beneficial for the development of novel devices. Moreover, the inorganic nature of LFDP is expected to make the LFDP survive during the various fabrication process, such as ion beam sputter, physical or chemical etching. As a result, LFDP would be a potential optoelectronic material for the integration on silicon photonics to fabricate functional devices.

4.2 Defect Engineering of Double perovskites

The concept of vacancy-ordered structure is also employed to describe another group of compounds with a formula unit of $A_3B_2X_9$. Such compound could be viewed as perovskites with a stoichiometry of $AB_{2/3}X_3$, in which one in three octahedral B^{3+}

sites is vacant for maintaining the charge neutrality. These materials exhibited a layered structure which is known as two-dimensional layered perovskite derivatives as shown in **Figure 17**. Among this group of compounds, Pb^{2+} was replaced by Sb^{3+} or Bi^{3+}, such as $Cs_3Sb_2I_9$ and $Rb_3Sb_2I_9$.[107, 132] With the substitution of large cation at A-site, the layered structured was converted into zero-dimensional dimers of face-sharing BX_6 octahedra (space group of $P6_3/mmc$), such as $MA_3Sb_2I_9$ and $MA_3Bi_2I_9$. Compounds with perovskite-related structure were further developed in PSCs which delivered noteworthy efficiency. For instance, the Ag-Bi-I system has reached a remarkable PCE above 5%. These lead-free perovskite derivatives acquired by defect engineering are discussed in this section for the aim of providing an outlook toward future lead-free PSCs.

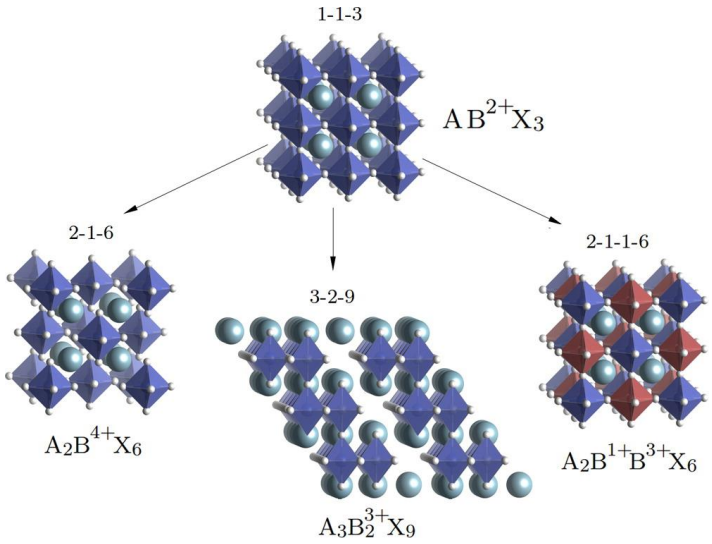

Figure 17. Illustration of the structural diversity of typical perovskite via vacancy engineering.[52]

The elements of group 15 in the periodic table including Bi and Sb were considered to be potential candidates for Pb substitution due to their similar electronic configuration with bivalent Pb.[133] The incorporation of Bi and Sb could be realized in different crystal structures, such as double perovskites, distorted perovskites and defect-engineered perovskites. Saparov et al. first synthesized the $Cs_3Sb_2I_9$ thin films via both solution process and vapor deposition in 2015.[107] As-synthesized $Cs_3Sb_2I_9$ exhibited 0D structure through solution process and 2D structure via vapor deposition. (referred to **Figure 18)** When $Cs_3Sb_2I_9$ transformed from 0D to 2D structure, the color of $Cs_3Sb_2I_9$ film changed from orange to red correspondingly. The optoelectronic properties of 2D layered $Cs_3Sb_2I_9$ showed a large bandgap of 2.05 eV and high absorption coefficient of 10^5 cm^{-1}. The PV performance of $Cs_3Sb_2I_9$-based PSCs composed of FTO/cl-TiO_2/$Cs_3Sb_2I_9$/PTAA/Au showed a low open-circuit voltage in

the range of 0.25-0.3 volt and a PCE less than 1%. The poor performance was ascribed to deep level defects. It is noted that $Cs_3Sb_2I_9$ thin film exhibited considerable air stability up to 60 days.

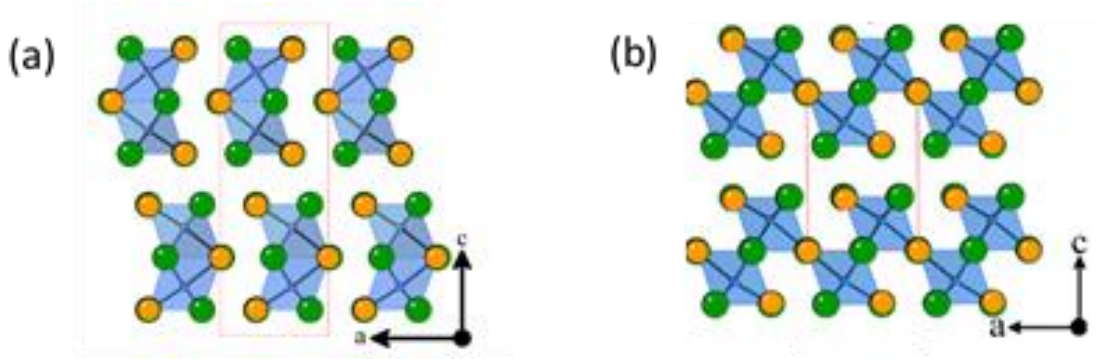

Figure 18. (a) 0D dimer modification of $Cs_3Sb_2I_9$ is composed of $Sb_2I_9^{3-}$ anions separated by Cs^+ cations. (b) 2D layered modification of $Cs_3Sb_2I_9$ of $Cs_3Sb_2I_9$. Cs and I are shown as orange and green spheres, respectively; Sb coordination polyhedral are shown in blue.[107]

In 2017, the $Cs_3Sb_2I_9$ and $MA_3Sb_2I_9$ with 0D structures were integrated into PSCs by Boopathi et al. via solution process.[134] After adding HI, the bandgap of $Cs_3Sb_2I_9$ was reduced from 2.3 to 2.0 eV and the bandgap of $MA_3Sb_2I_9$ was reduced from 2.20 to 1.95 eV. Owing to the enhanced absorption, $Cs_3Sb_2I_9$-based PSCs increased their PCE from 0.67% to 0.84%, while the $MA_3Sb_2I_9$ counterpart increased from 1.11% to 2.04%. The low V_{OC} and J_{SC} indicated the need for further optimization.

Because of the low current density of $MA_3Sb_2I_9$-based PSCs, F.Y. Jiang et al. doped Cl at the X-site in $MA_3Sb_2I_9$ to suppress the charge carrier recombination and fabricate a densely-packed film.[135] The resultant compound exhibited a general formula of $MA_3Sb_2Cl_xI_{9-x}$. With the addition of Cl^-, the crystal structure transformed from 0D dimer to 2D layered structure. The layered $MA_3Sb_2Cl_xI_{9-x}$ was integrated into PSCs with an architecture of FTO/cl-TiO_2/mp-TiO_2/$MA_3Sb_2Cl_xI_{9-x}$/Spiro-OMeTAD/Au which delivered a PCE of 2.19% along with a V_{OC} = 0.69 V and a J_{SC} of 5.04 mA/cm^2.

These results have shown that $A_3Sb_2I_9$ compounds tended to crystallize into a dimer structure (with fused bi-octahedron) or a layered structure (with corner sharing octahedron). With the application of DFT calculation, P.C. Harikesh et al. found that the $Rb_3Sb_2I_9$ showed a stronger tendency to form a layered structure than $Cs_3Sb_2I_9$. (referred to **Figure 19**)[132] This tendency was attributed to a smaller ionic radius of Rb (1.72Å) than Cs (1.88 Å). The $Rb_3Sb_2I_9$ exhibited an absorption coefficient above 10^5 cm^{-1} with a bandgap of 2.5 eV and a decent thermal stability up to 250°C. PSCs with an architecture of FTO/cl-TiO_2/$Rb_3Sb_2I_9$/poly-TPD/Au exhibited a PCE of 0.66%, a

V_{OC} of 0.55 V and a J_{SC} of 2.11 mA/cm^2. The low-dimensional structure of antimony-based perovskites leads to an anisotropic charge transport which was a limiting factor for the PV application. The modest performance of Sb-based perovskites solar cells was also ascribed to the defects.

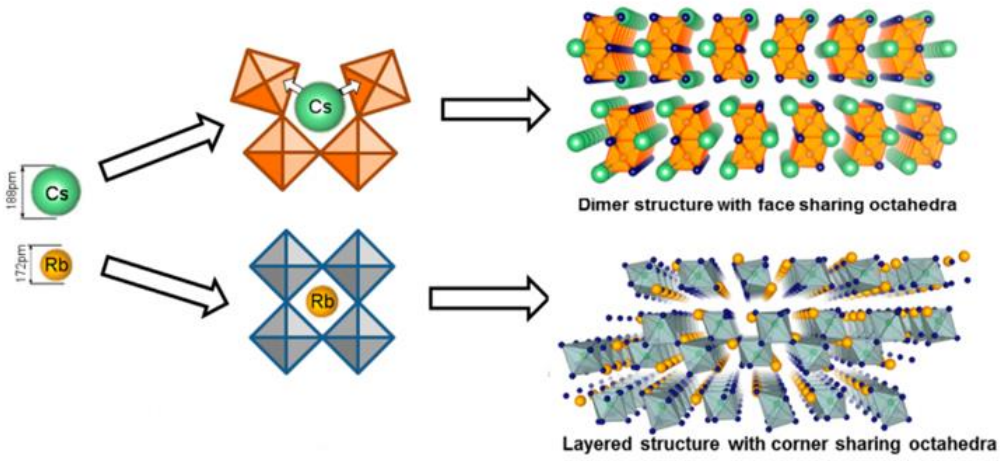

Figure 19. Schematically showing the influence of A-site cation size on the structure of $A_3Sb_2I_9$.[132]

C.T. Zuo et al. used NH_4^+ cation at the A-site in $A_3Sb_2I_9$ and doped the X-site with Br^- to obtain $(NH_4)_3Sb_2I_xBr_{9-x}$ ($0 \leq x \leq 9$).[136] The bandgap of $(NH_4)_3Sb_2I_xBr_{9-x}$ was tuned with the Br^- incorporation as evidenced from the absorption spectra. It was reported that the absorption onsets for $(NH_4)_3Sb_2I_6Br_3$, $(NH_4)_3Sb_2I_3Br_6$ and $(NH_4)_3Sb_2Br_9$ films were 516, 486, and 453 nm, respectively. Moreover, the electron mobility was improved from 1.5×10^{-4} to 12.3 cm^2 V^{-1} s^{-1} after the Br^- incorporation. Nevertheless, a worse PV performance was delivered for PSCs using $(NH_4)_3Sb_2I_xBr_{9-x}$ which was ascribed to the wider bandgap. Solar cells with a structure of ITO/PEDOT:PSS/$(NH_4)_3Sb_2I_9$/PC61BM/Al showed a PCE of 0.51%, a V_{OC} of 1.03 V, and a J_{SC} of 1.15 mA/cm^2. The PCE of $(NH_4)_3Sb_2I_6Br_3$-, $(NH_4)_3Sb_2I_3Br_6$-, and $(NH_4)_3Sb_2Br_9$-based devices was 0.19 %, 0.06 %, and 0.01 %, respectively

Due to the wide bandgap and low dimensionality of Sb-based perovskites, partial substitution was adopted in attempt to reduce the bandgap and improve the carrier transport. S. Chatterjee et al. partially replaced Sb^{3+} by Sn^{4+} and obtained a bandgap of 1.55 eV for the perovskite doped with 40% Sn^{4+}.[137] The PSCs with an inverted structure of ITO/Cu:NiO/$MA_3(Sb_{1-X}Sn_X)_2I_9$/ZnO/Al were fabricated and exhibited a PCE of 2.70%, a V_{OC} of 0.56 V, a J_{SC} of 8.32 mA/cm^2 and a FF of 0.58. The improved PCE was ascribed to the narrowed bandgap and the efficient charge extraction.

The typical 3D perovskite structure was realized by Nie et al. who first incorporated chalcogenide S^{2-} into $MA_3Sb_2I_9$, resulting in a compound with a general formula of $MASbSI_2$. The $MASbSI_2$ was carried out by the sequential reaction with antimony trisulfide (Sb_2S_3), antimony triiodide (SbI_3), and methylammonium iodide (MAI), in which Sb_2S_3 was deposited by chemical bath deposition on top of substrate first, followed by the spin-coating of SbI_3 and MAI. PSCs with a configuration of FTO/cl-TiO_2/mp-TiO_2/$MASbSI_2$/PCPDTBT/PEDOT:PSS/Au were fabricated and exhibited a PCE of 3.08%, a V_{OC} of 0.65V, and a J_{SC} of 8.12 mA/cm^2. Adonin et al. further employed Sb(V)-based pseudo-perovskite as a potential candidate for a light absorber.[138] The bromoantimonate (V) (N-EtPy)[$SbBr_6$] single crystal was synthesized by solution precipitation and formed perovskite-like 3D crystalline frameworks. Planar heterojunctions PSCs with structures of ITO/PEDOT:PSS/(N-EtPy)[$SbBr_6$]/PDI/Ag (p-i-n heterojunction) and ITO/cl-TiO_2/(N-EtPy)[$SbBr_6$]/P3HT/Au (n-i-p heterojunction) were fabricated. The n-i-p heterojunction PSCs achieved the best PCE of 3.8%, a V_{OC} of 1.29V, a J_{SC} of 5.1 mA/cm^2 and a FF of 0.58.

As a whole, the Sb-based defect perovskites with the 0-dimensional dimer phase can be easily synthesized, but have a wide bandgap and a low carrier transport. On the contrary, the 2-dimensional layered phase of Sb-based defect perovskites has a narrow bandgap and a higher carrier transport capability, but is hard to be synthesized. Recently, there are some solutions toward efficient Sb-based defect perovskites solar cells: (i) putting some additive (e.g. HI) in low dimensional Sb-based defect perovskites to decrease the bandgap, and (ii) doping ions at X-site or B-site to alter the crystal structure from lower to higher dimension.

Bismuth halide perovskite also exhibited a high structural diversity in terms of the face-, edge- or corner-sharing networks whose dimensionality ranging from zero-dimensional dimer units, to one-dimensional chain-like motifs or two dimensional layered networks, up to three-dimensional double perovskite frameworks (double perovskites).[139] Bismuth halide perovskite with zero dimensionality showed a basic formula unit of $A_3Bi_2X_9$. The double octahedral structure was composed of pairs of face-sharing BiX_6 octahedra to deliver complex $Bi_2X_9^{3-}$ anionic clusters, which were known as isolated metal halide dimers.[139-141] The discrete anionic bi-octahedral moieties were surround by the A-site cations. Multiple A-site cations have been incorporated into the 0D bismuth halide perovskite, such as K^+, Rb^+ and Cs^+.[139]

The widely studied 0D bismuth halide perovskite, $(CH_3NH_3)_3Bi_2I_9$, was composed of pairs of isolated metal halide dimer units of $Bi_2I_9^{3-}$ which was surrounded by randomly disordered $CH_3NH_3^+$ cations.[140] Öz et al. integrated the $(CH_3NH_3)_3Bi_2I_9$ into planar PSCs with a configuration of ITO/PEDOT:PSS/$(CH_3NH_3)_3Bi_2I_9$/PCBM/Ca/Al and demonstrated their photovoltaic performance with a V_{OC} of 0.66 V, a J_{SC} of 0.22

mA/cm^2, a FF of 49%, and a PCE of around 0.1%.[142] High exciton binding energy led to inefficient charge separation in the perovskite active layer which limited the J_{SC} of devices. The top performance of PSCs employing 0D bismuth halide perovskite was achieved by Park et al. who integrated $Cs_3Bi_2I_9$ into mesoscopic architecture.[143] PSCs composed of FTO/cl-TiO_2/mp-TiO_2/$Cs_3Bi_2I_9$/Spiro-OMeTAD/Ag exhibited a PCE of 1.09% a FF of 0.6, a V_{OC} of 0.85 V, and a J_{SC} of 2.15 mA/cm^2.

The 1D Bi-based perovskite was composed of BiI_5^{2-} which was resulted from the corrugated metal halide chains of distorted corner-sharing BiI_6 octahedra. Such metal halide chains were interlinked via divalent A-site cations.[144] The $HDABiI_5$ [HDA = 1,6-hexanediammonium $[H_3N\text{-}(CH_2)_6\text{-}NH_3]^{2+}$] with 1D structure was investigated by Fabian et al. who synthesized the compound with an orthorhombic crystal structure by a solution process. As-synthesized $HDABiI_5$ possessed a bandgap of 2.05 eV with an indirect band transition. PSCs with an architecture of FTO/cl-TiO_2/mp-TiO_2/$HDABiI_5$/Spiro-OMeTAD/Au were fabricated and delivered a PCE of 0.027%, a V_{OC} of 0.40 V, a J_{SC} of 0.12 mA/cm^2, and a FF of 43%.

Two-dimensional layered structures were observed in metal-deficient or defect-type perovskites which employed ion with higher valence. The crystal structure was based on cubic close packing octahedra with the B-site ions filling with two-thirds of the octahedral cavities, while one-third of the B-sites were vacant. Above arrangement resulted in an inorganic metal-deficient layers with the formula of $B_{2/3}X_4^{2-}$, which were made of ridged layers of corner-sharing, distorted BX_6 octahedra to realize the 2D structure. Thus, the structure could be considered as a distorted defect variant of typical ABX_3 perovskite.[139]

Besides the 0D structure of $Cs_3Bi_2I_9$, Johansson et al. reported that $CsBi_3I_{10}$ exhibited a 2D layered structure.[145] $Cs_3Bi_2I_{10}$ was synthesized by adjusting the stoichiometric composition of the CsI and BiI_3 via solution process. As-synthesized $CsBi_3I_{10}$ exhibited a bandgap of 1.77 eV along with an absorption coefficient of 1.4 x 10^5 cm^{-1}, suggesting a comparable light extinction to Pb-based analogues. The synthesis of $CsBi_3I_{10}$ resulted in a more uniform, smoother and pinhole-free film compared with the $Cs_3Bi_2I_9$ film. PSCs with a structure of FTO/cl-TiO_2/mp-TiO_2/$CsBi_3I_{10}$/P3HT/Ag exhibited a PCE of 0.40%, which was higher than the $Cs_3Bi_2I_9$-based counterpart (0.2 %) and the BiI_3-based counterpart (0.03 %). These results suggested that the perovskites with low dimensionality (0D to 2D) usually suffered from wide bandgap and anisotropic carrier transport.

The photovoltaic response exhibited by the bismuth halide perovskite based solar cells with different stoichiometry was put under the spotlight since the $A_3B_2X_9$ variant perovskite suffers from wide bandgap and anisotropic carrier transport. The Ag-Bi-I system has demonstrated a high diversity in structure and promising optoelectronic

properties. The B-site cavity of AgBiI could be filled with different ratio between Ag^{+}, Bi^{3+} and vacancy, resulting in a general chemical formula of $Ag_aBi_bI_x$ where x=a+3b. The phase diagrams of $Ag_aBi_bI_x$ system have been proposed by several groups and significant discrepancies of stoichiometry and phase transformations are presented. In 1979, Ceolin et al. determined the two types of $Ag_aBi_bI_x$ alloys in the stoichiometric formula of Ag_2BiI_5 and $AgBi_2I_7$ by differential thermal analysis.[146] On contrary, Bulakhova et al. revealed that two types of stoichiometry for $Ag_aBi_bI_x$ alloys was Ag_3BiI_6 and $AgBiI_4$ via the thermal and X-ray phase analysis.[147] Mashadieva et al. investigated the Ag-Bi-I system by differential thermal analysis, XRD techniques as well as electro-motive force measurements.[148] This detailed study revealed that the two types of $Ag_aBi_bI_x$ alloys were Ag_2BiI_5 and $AgBi_2I_7$. The synchrotron XRD discovered the composition modulation in the $Ag_{2-3x}Bi_xI_2$ ($x = 0.33 \sim 0.60$) crystal structure exhibits single phase.[149] For instance, the Ag-rich compound presented rhombohedral structures while the Bi-rich compound exhibited defect-spinel-type cubic structures. Moreover, the rhombohedral structure compounds delivered shallower valence band maximum, larger indirect bandgap, and higher electrical conductivity along with lower activation energy for electron hopping than the cubic structure compounds.

Apart from the differences within the phase diagram, a large variance was observed among the interpretations of crystal structure. Sargent et al. interpreted $AgBi_2I_7$ crystal as a combination between $[AgI_6]$ octahedra and $[BiI_8]$ hexahedra which was originated from the cubic structure of $ThZr_2H_7$.[150] Nevertheless, this interpretation was questionable since the Bi-I bond was too short to support the lattice structure compared with the known Ag−Bi−I compounds.[151] Consequently, the $ThZr_2H_7$-type $AgBi_2I_7$ structure showed an unreasonably large mass density of 10.29 g/cm^3, which was twice that of other known Ag−Bi−I compounds. Yan et al. showed that the $ThZr_2H_7$-type $AgBi_2I_7$ was thermodynamically unstable via DFT calculation and $AgBi_2I_7$ should be described as an Ag-deficient $AgBiI_4$ structure.

Turkevych et al. proposed that the Ag-Bi-I system should belong to the rudorffite family with a typical structure similar to $NaVO_2$ as shown in **Figure 20**.[152] The crystal structure of aforementioned $AgBi_2I_7$ was recognized as rudorffite structure with a space group of R3m. The major difference between the rudorffite and the prototypical $NaVO_2$ was that the cation cavities within the sublattice showed a co-distribution of Ag^{+}, Bi^{3+} and vacancies to reach the charge neutrality. Rudorffite was composed of the combination of two types of edge-shared octahedra ($M'X_6$ and $M''X_6$), resulting in a layered structure. The authors investigated the crystal structures and the optoelectronic properties of Ag_3BiI_6, Ag_2BiI_5, $AgBiI_4$ and $AgBi_2I_7$ which were thermodynamically favorable with the smallest unit cell. $Ag_aBi_bI_x$ thin films with different stoichiometry

were synthesized by solution process which displayed a lifetime around 200 ns deduced by TRPL. PSCs with a mesoscopic structure of FTO/cl-TiO_2/mp-TiO_2/Ag_3BiI_6/PTAA/Au achieved a remarkable PCE of 4.3% along with a V_{OC} of 0.63 V, a J_{SC} of 10.7 mA/cm^2, and a FF of 0.64.

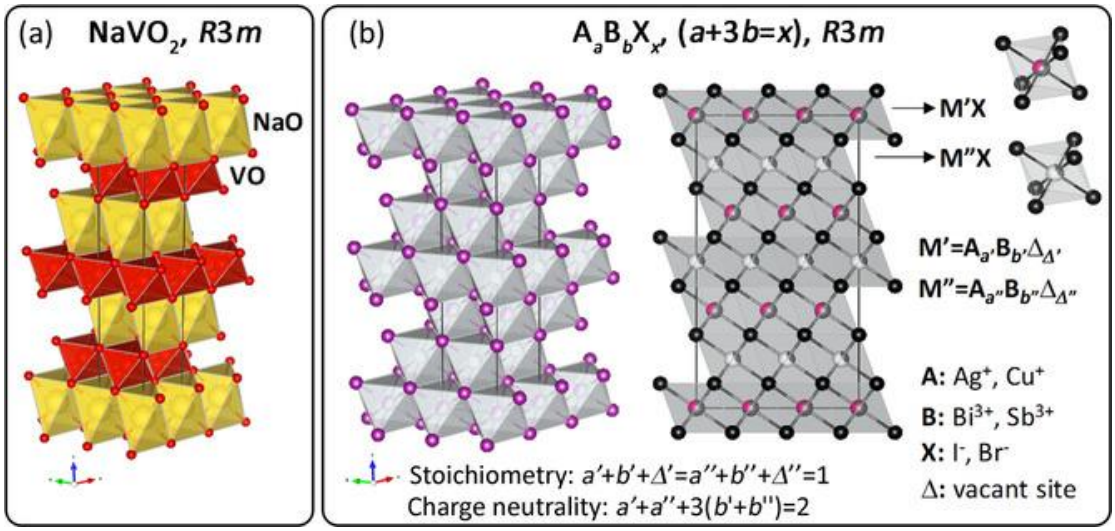

Figure 20. (a) Illustration of $NaVO_2$ crystal structure. (b) Crystal structures of the $A_aB_bX_x$ halide rudorffites.[152]

The Ag-Bi-I family was further expanded with the incorporation of sulfide anions via a solution process.[153] Partial substitution of sulfide and changing levels of anionic substitution in $Ag_aBi_bI_x$ led to tunable optoelectronic properties. Moreover, a minor substitution of I^- with S^{2-} still induced notable contractions of the bandgaps and upshifts of the valence band edges. PSCs composed of FTO/cl-TiO_2/mp-TiO_2/silver bismuth sulfoiodides/PTAA/Au were fabricated with various stoichiometry of $Ag_aBi_bI_{a+3b}$ and different level of anion substitution. The champion cell was fabricated based on $Ag_3BiI_{6-2x}S_x$ whose PCE (active area of 0.16 cm^2) enhanced from 4.33 ± 0.05 to 5.44 ±0.07% upon changing x from 0 to 4 at% as shown in **Figure 21a**. As-fabricated PSCs exhibited a noteworthy stability and retained over 90% of their initial PCE after 45 days under ambient conditions. These results in this subsection imply that the Ag-Bi-I system serves as an effective active layer and exhibits promising properties for the future PV application.

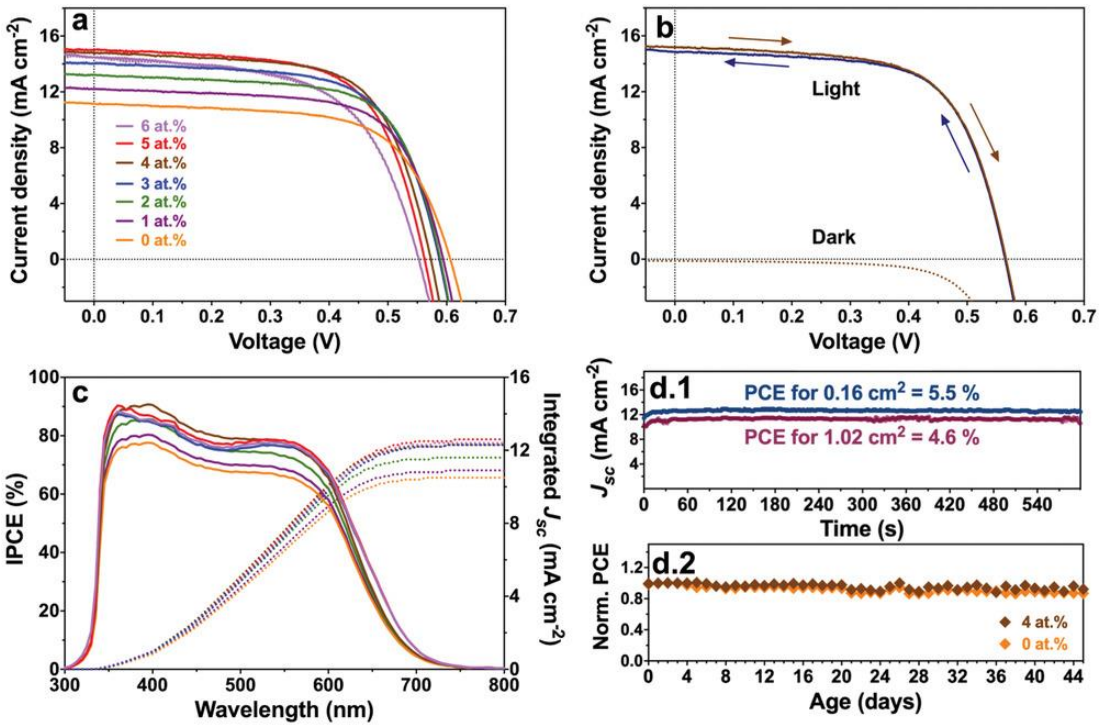

Figure 21. (a) J-V curves of $Ag_3BiI_{6-2x}S_x$-based PSCs with different level of substitution: x = 0 (orange), 1 (purple), 2 (green), 3 (blue), 4 (brown), 5 (red), and 6 at% (magenta). (b) J-V curves of device with x=4 at% under forward and reverse scan along with the dark current. (c) IPCE spectra of various devices corresponding to Fig. (a). (d.1) Transient photocurrent of devices biased at maximum power point; (d.2) Stability test of $Ag_3BiI_{6-2x}S_x$-based PSCs with x = 0 and 4 at% stored in air under light.[153]

5. Conclusion

A typical perovskite solar cells is usually composed of a perovskite active layer sandwiched between two selective contacts to extract the charge carries. Despite the high PCE, the stability and toxicity of PSCs are the key issues for real commercial uptake. Lead-free double perovskite has been regarded as a potential candidate for PSCs due to its diversity of metal cation substitution, suitable optoelectronic properties, high stability, and nontoxicity.

This review presents the theoretical calculations of the optoelectronic properties for various classes of double perovskites showing their properties and potential for future applications in PVs and beyond. The structural and electronic properties calculations suggest that some double perovskites have suitable bandgaps which meets the requirement of Shockley–Queisser limit. Moreover, substitution of variant elements in double perovskites effectively modulate the band structure, transition nature and bandgap. Despite the suitable bandgap values, theoretical predictions indicate that most

of the Bi-based double perovskites have indirect bandgaps which are disadvantageous for optical absorption and carrier transport due to the participation of phonon-assisted processes. On the other hand, although the In-based double perovskites display direct bandgaps, this group of compounds suffers from the parity-induced forbidden transitions which obstruct the optical transition.

Experimental details of double perovskites including the deposition methodology, post-treatment, chemical composition, nanostructure, and doping effects are discussed in this review. These parameters have a significant impact on the material characteristics and directly determine the structure, optoelectronic properties and PV performances. An apparent trend is that all the double perovskites have displayed an improved thermal and ambient stability compared with Pb-based PSCs, but humbler PV performance. The discrepancies observed in bandgap values of double perovskite require in-depth investigation since the bandgap significantly influences the operational characteristics of PSCs. Elemental substitution has shown to be an effective method for improving PV performance with tunable bandgap and optoelectronic properties. The investigated carrier dynamics can serve as a fundamental insight for future optimization and design of double perovskites.

Optoelectronic applications including photocatalytic, thermochromism, light emitting diode, photodetector, and X-ray detector have delivered promising results due to the unique properties of double perovskites. The Cs2AgInCl6-based LED with direct bandgap and high ambient stability achieved a PLQE over 80% by the elemental substitution that breaks the parity-induced forbidden transition and reduces the electronic dimensionality. $Cs_2AgBiBr_6$-based X-ray detector accomplished a fast response (τ rise =24 μs, τ decay =13 μs) and a high sensitivity of 288.8 μC Gy air-1 cm-2 at 50 V bias voltage due to the intrinsic X-ray detectivity and octahedral disordering. On the other hand, defect engineering in halide perovskite provided another outlook for Pb-substitution with distorted perovskite structure. The vacancy-ordered A3B2X9 perovskite and the AaBbXx halide rudorffites are semiconductors with suitable bandgaps, and the fabricated cells have demonstrated a PCE above 5%.

Most studies focused on two prototypical types of double perovskites, $Cs_2AgBiBr_6$ and $Cs_2AgInCl_6$, indicating a huge territory of perovskites waiting to be investigated by considering a wide variety of single-valent and trivalent ions. Moreover, the energy-level matching charge transport layers are highly required for double perovskite solar cells. Other related issues such as carrier dynamic and interfacial chemistry at charge transport layer/perovskite interface are calling for deeper research efforts for future cell optimization. It is expected that, combining theoretical and experimental studies, stable and efficient lead-free double perovskite solar cells will be realized showing an interesting alternative for perovskite based technology.

Acknowledgements

The authors are grateful to the research grant from the Ministry of Science and Technology of Taiwan (MOST 107-2221-E-006-190-MY3, MOST 107-2119-M-006-002, MOST 108-3116-F-006-001, 108-2218-E-006 -043 -MY3). This work was financially supported by the Hierarchical Green-Energy Materials (Hi-GEM) Research Center, from The Featured Areas Research Center Program within the framework of the Higher Education Sprout Project by the Ministry of Education (MOE) in Taiwan. This research was, in part, supported by the Ministry of Education, Taiwan, R. O. C. Headquarter of University Advancement to the National Cheng Kung University) NCKU. D. C. L. and M.P. thank PeroBOOST project (EFRE-0800120; NW-1-1040h) for funding. G.G. acknowledges the "HY-NANO" project that has received funding from the European Research Council (ERC) Starting Grant 2018 under the European Union's Horizon 2020 research and innovation programme (Grant agreement No. 802862).

References

[1] A. Kojima, K. Teshima, Y. Shirai, T. Miyasaka, *J. Am. Chem. Soc.* **2009**, *131*, 6050.

[2] H.-S. Kim, C.-R. Lee, J.-H. Im, K.-B. Lee, T. Moehl, A. Marchioro, S.-J. Moon, R. Humphry-Baker, J.-H. Yum, J. E. Moser, M. Grätzel, N.-G. Park, *Sci. Rep.* **2012**, *2*, 591; M. M. Lee, J. Teuscher, T. Miyasaka, T. N. Murakami, H. J. Snaith, *Science* **2012**, *338*, 643.

[3] https://www.nrel.gov/pv/assets/pdfs/best-research-cell-efficiencies-190416.pdf.

[4] L. Dou, Y. Yang, J. You, Z. Hong, W.-H. Chang, G. Li, Y. Yang, *Nat. Commun.* **2014**, *5*, 5404.

[5] Q. Van Le, H. W. Jang, S. Y. Kim, *Small Methods* **2018**, *2*, 1700419.

[6] T. A. Berhe, W.-N. Su, C.-H. Chen, C.-J. Pan, J.-H. Cheng, H.-M. Chen, M.-C. Tsai, L.-Y. Chen, A. A. Dubale, B.-J. Hwang, *Energy Environ. Sci.* **2016**, *9*, 323.

[7] N. J. Jeon, J. H. Noh, W. S. Yang, Y. C. Kim, S. Ryu, J. Seo, S. I. Seok, *Nature* **2015**, *517*, 476; D. P. McMeekin, G. Sadoughi, W. Rehman, G. E. Eperon, M. Saliba, M. T. Hörantner, A. Haghighirad, N. Sakai, L. Korte, B. Rech, M. B. Johnston, L. M. Herz, H. J. Snaith, *Science* **2016**, *351*, 151; M. Saliba, T. Matsui, J.-Y. Seo, K. Domanski, J.-P. Correa-Baena, M. K. Nazeeruddin, S. M. Zakeeruddin, W. Tress, A. Abate, A. Hagfeldt, M. Grätzel, *Energy Environ. Sci.* **2016**, *9*, 1989.

[8] K. Hong, Q. V. Le, S. Y. Kim, H. W. Jang, *J. Mater. Chem. C* **2018**, *6*, 2189.

[9] S. F. Hoefler, G. Trimmel, T. Rath, *Monatsh. Chem.* **2017**, *148*, 795.

[10] P.-K. Kung, M.-H. Li, P.-Y. Lin, Y.-H. Chiang, C.-R. Chan, T.-F. Guo, P. Chen, *Adv. Mater. Interfaces* **2018**, *5*, 1800882.

[11] F. Matteocci, L. Cinà, E. Lamanna, S. Cacovich, G. Divitini, P. A. Midgley, C. Ducati, A. Di Carlo, *Nano Energy* **2016**, *30*.

[12] G. Flora, D. Gupta, A. Tiwari, *Interdiscip. Toxicol.* **2012**, *5*, 47.

[13] https://www.cdc.gov/nceh/lead/publications/refugeetoolkit/powerpoint_files/medicalservice.ppt.

[14] S. Shao, J. Liu, G. Portale, H.-H. Fang, G. R. Blake, G. H. ten Brink, L. J. A. Koster, M. A. Loi, *Adv. Energy Mater.* **2018**, *8*, 1702019; D. Yang, J. Lv, X. Zhao, Q. Xu, Y. Fu, Y. Zhan, A. Zunger, L. Zhang, *Chem. Mater.* **2017**, *29*, 524; W. Liao, D. Zhao, Y. Yu, C. R. Grice, C. Wang, A. J. Cimaroli, P. Schulz, W. Meng, K. Zhu, R.-G. Xiong, Y. Yan, *Adv. Mater.* **2016**, *28*, 9333; I. Kopacic, B. Friesenbichler, S. F. Hoefler, B. Kunert, H. Plank, T. Rath, G. Trimmel, *ACS Appl. Energy Mater.* **2018**, *1*, 343.

[15] N. Wang, Y. Zhou, M.-G. Ju, H. F. Garces, T. Ding, S. Pang, X. C. Zeng, N. P. Padture, X. W. Sun, *Adv. Energy Mater.* **2016**, *6*, 1601130; T.-B. Song, T. Yokoyama, C. C. Stoumpos, J. Logsdon, D. H. Cao, M. R. Wasielewski, S. Aramaki, M. G.

Kanatzidis, *J. Am. Chem. Soc.* **2017**, *139*, 836.
[16] P.-P. Sun, Q.-S. Li, L.-N. Yang, Z.-S. Li, *Nanoscale* **2016**, *8*, 1503.
[17] C. N. Savory, A. Walsh, D. O. Scanlon, *ACS Energy Lett.* **2016**, *1*, 949.
[18] X.-G. Zhao, J.-H. Yang, Y. Fu, D. Yang, Q. Xu, L. Yu, S.-H. Wei, L. Zhang, *J. Am. Chem. Soc.* **2017**, *139*, 2630.
[19] X.-G. Zhao, D. Yang, Y. Sun, T. Li, L. Zhang, L. Yu, A. Zunger, *J. Am. Chem. Soc.* **2017**, *139*, 6718.
[20] R. G. Niemann, L. Gouda, J. Hu, S. Tirosh, R. Gottesman, P. J. Cameron, A. Zaban, *J. Mater. Chem. A* **2016**, *4*, 17819; M. T. Klug, A. Osherov, A. A. Haghighirad, S. D. Stranks, P. R. Brown, S. Bai, J. T. W. Wang, X. Dang, V. Bulović, H. J. Snaith, A. M. Belcher, *Energy Environ. Sci.* **2017**, *10*, 236; A. Swarnkar, W. J. Mir, A. Nag, *ACS Energy Lett.* **2018**, *3*, 286; G. Volonakis, F. Giustino, *Appl. Phys. Lett.* **2018**, *112*, 243901; Q. Xu, D. Yang, J. Lv, Y.-Y. Sun, L. Zhang, *Small Methods* **2018**, *2*, 1700316; M.-G. Ju, M. Chen, Y. Zhou, J. Dai, L. Ma, N. P. Padture, X. C. Zeng, *Joule* **2018**, *2*, 1231; X.-G. Zhao, D. Yang, J.-C. Ren, Y. Sun, Z. Xiao, L. Zhang, *Joule* **2018**, *2*, 1662; S. Khalfin, Y. Bekenstein, *Nanoscale* **2019**, *11*, 8665.
[21] P. Cheng, T. Wu, Y. Li, L. Jiang, W. Deng, K. Han, *New J. Chem.* **2017**, *41*, 9598.
[22] J. Luo, X. Wang, S. Li, J. Liu, Y. Guo, G. Niu, L. Yao, Y. Fu, L. Gao, Q. Dong, C. Zhao, M. Leng, F. Ma, W. Liang, L. Wang, S. Jin, J. Han, L. Zhang, J. Etheridge, J. Wang, Y. Yan, E. H. Sargent, J. Tang, *Nature* **2018**, *563*, 541.
[23] E. T. McClure, M. R. Ball, W. Windl, P. M. Woodward, *Chem. Mater.* **2016**, *28*, 1348.
[24] K. I. Kobayashi, T. Kimura, H. Sawada, K. Terakura, Y. Tokura, *Nature* **1998**, *395*, 677; S. Sengodan, S. Choi, A. Jun, T. H. Shin, Y.-W. Ju, H. Y. Jeong, J. Shin, J. T. S. Irvine, G. Kim, *Nat. Mater.* **2014**, *14*, 205; Y. Liu, Z. Wang, J.-P. M. Veder, Z. Xu, Y. Zhong, W. Zhou, M. O. Tade, S. Wang, Z. Shao, *Adv. Energy Mater.* **2018**, *8*, 1702604; S. Yoo, A. Jun, Y.-W. Ju, D. Odkhuu, J. Hyodo, H. Y. Jeong, N. Park, J. Shin, T. Ishihara, G. Kim, *Angew. Chem. Int. Ed.* **2014**, *53*, 13064; R. N. Mahato, K. Sethupathi, V. Sankaranarayanan, *J. Appl. Phys.* **2010**, *107*, 09D714; J.-W. G. Bos, J. P. Attfield, *Z. Anorg. Allg. Chem.* **2004**, *630*, 2248; Y. Moritomo, S. Xu, A. Machida, T. Akimoto, E. Nishibori, M. Takata, M. Sakata, K. Ohoyama, *J. Phys. Soc. Jpn.* **2000**, *69*, 1723; D. D. Sarma, E. V. Sampathkumaran, S. Ray, R. Nagarajan, S. Majumdar, A. Kumar, G. Nalini, T. N. Guru Row, *Solid State Commun.* **2000**, *114*, 465.
[25] K.-L. Hu, M. Kurmoo, Z. Wang, S. Gao, *Chem.: Eur. J.* **2009**, *15*, 12050.
[26] S. Nagane, U. Bansode, O. Game, S. Chhatre, S. Ogale, *Chem. Commun.* **2014**, *50*, 9741.
[27] Q. Jiang, D. Rebollar, J. Gong, E. L. Piacentino, C. Zheng, T. Xu, *Angew. Chem. Int. Ed.* **2015**, *54*, 7617.

[28] J. Qian, B. Xu, W. Tian, *Org. Electron.* **2016**, *37*, 61.
[29] V. M. Goldschmidt, *Naturwissenschaften* **1926**, *14*, 477.
[30] C. Li, X. Lu, W. Ding, L. Feng, Y. Gao, Z. Guo, *Acta Crystallogr B* **2008**, *64*, 702.
[31] W. Travis, E. N. K. Glover, H. Bronstein, D. O. Scanlon, R. G. Palgrave, *Chem. Sci.* **2016**, *7*, 4548.
[32] T. J. Huang, Z. X. Thiang, X. Yin, C. Tang, G. Qi, H. Gong, *Chem.: Eur. J.* **2016**, *22*, 2146.
[33] M. a. L. Johnsson, P. , in *Handbook of Magnetism and Advanced Magnetic Materials*, Wiley-VCH, 2007.
[34]J. I. Uribe, D. Ramirez, J. M. Osorio-Guillén, J. Osorio, F. Jaramillo, *J. Phys. Chem. C* **2016**, *120*, 16393; G. Kieslich, S. Sun, A. K. Cheetham, *Chem. Sci.* **2014**, *5*, 4712.
[35] G. Kieslich, S. Sun, A. K. Cheetham, *Chem. Sci.* **2015**, *6*, 3430.
[36]T. Baikie, Y. Fang, J. M. Kadro, M. Schreyer, F. Wei, S. G. Mhaisalkar, M. Graetzel, T. J. White, *J. Mater. Chem. A* **2013**, *1*, 5628; M. T. Weller, O. J. Weber, P. F. Henry, A. M. Di Pumpo, T. C. Hansen, *Chem. Commun.* **2015**, *51*, 4180.
[37] A. H. Slavney, T. Hu, A. M. Lindenberg, H. I. Karunadasa, *J. Am. Chem. Soc.* **2016**, *138*, 2138.
[38] G. Volonakis, M. R. Filip, A. A. Haghighirad, N. Sakai, B. Wenger, H. J. Snaith, F. Giustino, *J. Phys. Chem. Lett* **2016**, *7*, 1254.
[39] G. King, P. M. Woodward, *J. Mater. Chem.* **2010**, *20*, 5785.
[40] P. Zhang, J. Yang, S.-H. Wei, *J. Mater. Chem. A* **2018**, *6*, 1809.
[41] A. E. Fedorovskiy, N. A. Drigo, M. K. Nazeeruddin, *Small Methods* **2019**, *0*, 1900426.
[42] W. Wong-Ng, J. A. Kaduk, M. Luong, Q. Huang, *Powder Diffr.* **2014**, *29*, 371; M. Vigneshwaran, T. Ohta, S. Iikubo, G. Kapil, T. S. Ripolles, Y. Ogomi, T. Ma, S. S. Pandey, Q. Shen, T. Toyoda, K. Yoshino, T. Minemoto, S. Hayase, *Chem. Mater.* **2016**, *28*, 6436; O. A. Lozhkina, A. A. Murashkina, M. S. Elizarov, V. V. Shilovskikh, A. A. Zolotarev, Y. V. Kapitonov, R. Kevorkyants, A. V. Emeline, T. Miyasaka, *Chem. Phys. Lett.* **2018**, *694*, 18.
[43] M. R. Filip, S. Hillman, A. A. Haghighirad, H. J. Snaith, F. Giustino, *J. Phys. Chem. Lett* **2016**, *7*, 2579.
[44] D. Weber, *J. Chem. Sci.* **1978**, *33*, 1443.
[45] R. Pandey, J. D. Gale, S. K. Sampath, J. Recio, *J. Am. Ceram. Soc.* **2004**, *82*, 3337.
[46] A. E. Maughan, A. M. Ganose, M. M. Bordelon, E. M. Miller, D. O. Scanlon, J. R. Neilson, *J. Am. Chem. Soc.* **2016**, *138*, 8453; I. D. Brown, *Can. J. Chem.* **1964**, *42*, 2758.
[47] C. J. Bartel, C. Sutton, B. R. Goldsmith, R. Ouyang, C. B. Musgrave, L. M. Ghiringhelli, M. Scheffler, *Sci. Adv.* **2019**, *5*, eaav0693.

[48] T. Umebayashi, K. Asai, T. Kondo, A. Nakao, *Phys. Rev. B* **2003**, *67*, 155405.
[49] H. Gaspard-Iloughmane, C. Le Roux, *Eur. J. Org. Chem.* **2004**, *2004*, 2517; S. Antoniotti, E. Duñach, *Eur. J. Org. Chem.* **2004**, *2004*, 3459.
[50] W. Meng, X. Wang, Z. Xiao, J. Wang, D. B. Mitzi, Y. Yan, *J. Phys. Chem. Lett* **2017**, *8*, 2999.
[51] J. Yang, P. Zhang, S.-H. Wei, *J. Phys. Chem. Lett* **2018**, *9*, 31.
[52] F. Giustino, H. J. Snaith, *ACS Energy Lett.* **2016**, *1*, 1233.
[53] L. Liang, P. Gao, *Adv. Sci.* **2018**, *5*, 1700331.
[54] A. M. A. Leguy, P. Azarhoosh, M. I. Alonso, M. Campoy-Quiles, O. J. Weber, J. Yao, D. Bryant, M. T. Weller, J. Nelson, A. Walsh, M. van Schilfgaarde, P. R. F. Barnes, *Nanoscale* **2016**, *8*, 6317.
[55] N. Rajeev Kumar, R. Radhakrishnan, *Mater. Lett.* **2018**, *227*, 289.
[56] Y. Bekenstein, J. C. Dahl, J. Huang, W. T. Osowiecki, J. K. Swabeck, E. M. Chan, P. Yang, A. P. Alivisatos, *Nano Lett.* **2018**, *18*, 3502.
[57] Q. Li, Y. Wang, W. Pan, W. Yang, B. Zou, J. Tang, Z. Quan, *Angew. Chem. Int. Ed.* **2017**, *56*, 15969.
[58] D. Bartesaghi, A. H. Slavney, M. C. Gélvez-Rueda, B. A. Connor, F. C. Grozema, H. I. Karunadasa, T. J. Savenije, *J. Phys. Chem. C* **2018**, *122*, 4809.
[59] L. Zhou, Y.-F. Xu, B.-X. Chen, D.-B. Kuang, C.-Y. Su, *Small* **2018**, *14*, 1703762.
[60] R. L. Z. Hoye, P. Schulz, L. T. Schelhas, A. M. Holder, K. H. Stone, J. D. Perkins, D. Vigil-Fowler, S. Siol, D. O. Scanlon, A. Zakutayev, A. Walsh, I. C. Smith, B. C. Melot, R. C. Kurchin, Y. Wang, J. Shi, F. C. Marques, J. J. Berry, W. Tumas, S. Lany, V. Stevanović, M. F. Toney, T. Buonassisi, *Chem. Mater.* **2017**, *29*, 1964.
[61] A. H. Slavney, L. Leppert, D. Bartesaghi, A. Gold-Parker, M. F. Toney, T. J. Savenije, J. B. Neaton, H. I. Karunadasa, *J. Am. Chem. Soc.* **2017**, *139*, 5015.
[62] K.-z. Du, W. Meng, X. Wang, Y. Yan, D. B. Mitzi, *Angew. Chem. Int. Ed.* **2017**, *56*, 8158.
[63] J. N. Wilson, H. Idriss, *J. Am. Chem. Soc.* **2002**, *124*, 11284; L. Bellaiche, A. Zunger, *Phys. Rev. B* **1998**, *57*, 4425.
[64] M. R. Filip, G. E. Eperon, H. J. Snaith, F. Giustino, *Nat. Commun.* **2014**, *5*, 5757.
[65] T. Li, X. Zhao, D. Yang, M.-H. Du, L. Zhang, *Phys. Rev. Appl.* **2018**, *10*, 041001.
[66] E. Greul, Michiel L. Petrus, A. Binek, P. Docampo, T. Bein, *J. Mater. Chem. A* **2017**, *5*, 19972.
[67] J. Kim, H. Kim, M. Chandran, S.-C. Lee, S. H. Im, K.-H. Hong, *APL Mater.* **2018**, *6*, 084903.
[68] Z. Xiao, Y. Yan, H. Hosono, T. Kamiya, *J. Phys. Chem. Lett* **2018**, *9*, 258.
[69] Z. Xiao, K.-Z. Du, W. Meng, D. B. Mitzi, Y. Yan, *Angew. Chem.* **2017**, *129*, 12275.
[70] Z. Xiao, W. Meng, J. Wang, Y. Yan, *ChemSusChem* **2016**, *9*, 2628.

[71] Z. Xiao, K.-Z. Du, W. Meng, J. Wang, D. B. Mitzi, Y. Yan, *J. Am. Chem. Soc.* **2017**, *139*, 6054.
[72] Y.-J. Li, T. Wu, L. Sun, R.-X. Yang, L. Jiang, P.-F. Cheng, Q.-Q. Hao, T.-J. Wang, R.-F. Lu, W.-Q. Deng, *RSC Adv.* **2017**, *7*, 35175.
[73] F. Wei, Z. Deng, S. Sun, F. Zhang, D. M. Evans, G. Kieslich, S. Tominaka, M. A. Carpenter, J. Zhang, P. D. Bristowe, A. K. Cheetham, *Chem. Mater.* **2017**, *29*, 1089.
[74] C. Wu, Q. Zhang, Y. Liu, W. Luo, X. Guo, Z. Huang, H. Ting, W. Sun, X. Zhong, S. Wei, S. Wang, Z. Chen, L. Xiao, *Adv. Sci.* **2018**, *5*, 1700759.
[75] W. Ning, F. Wang, B. Wu, J. Lu, Z. Yan, X. Liu, Y. Tao, J.-M. Liu, W. Huang, M. Fahlman, L. Hultman, T. C. Sum, F. Gao, *Adv. Mater.* **2018**, *30*, 1706246.
[76] M. Pantaler, K. T. Cho, V. I. E. Queloz, I. García Benito, C. Fettkenhauer, I. Anusca, M. K. Nazeeruddin, D. C. Lupascu, G. Grancini, *ACS Energy Lett.* **2018**, *3*, 1781.
[77] M. Wang, P. Zeng, S. Bai, J. Gu, F. Li, Z. Yang, M. Liu, *Sol. RRL* **2018**, *2*, 1800217.
[78] C. Zhang, L. Gao, S. Teo, Z. Guo, Z. Xu, S. Zhao, T. Ma, *Sustainable Energy Fuels* **2018**, *2*, 2419.
[79] M. Chen, M.-G. Ju, A. D. Carl, Y. Zong, R. L. Grimm, J. Gu, X. C. Zeng, Y. Zhou, N. P. Padture, *Joule* **2018**, *2*, 558.
[80] X. Qiu, B. Cao, S. Yuan, X. Chen, Z. Qiu, Y. Jiang, Q. Ye, H. Wang, H. Zeng, J. Liu, M. G. Kanatzidis, *Sol. Energy Mater. Sol. Cells* **2017**, *159*, 227.
[81] Y. Jiang, H. Zhang, X. Qiu, B. Cao, *Mater. Lett.* **2017**, *199*, 50.
[82] X. Qiu, Y. Jiang, H. Zhang, Z. Qiu, S. Yuan, P. Wang, B. Cao, *Phys. Status Solidi Rapid Res. Lett.* **2016**, *10*, 587.
[83] B. Lee, A. Krenselewski, S. I. Baik, D. N. Seidman, R. P. H. Chang, *Sustainable Energy Fuels* **2017**, *1*, 710.
[84] H.-J. Feng, W. Deng, K. Yang, J. Huang, X. C. Zeng, *J. Phys. Chem. C* **2017**, *121*, 4471.
[85] G. Volonakis, A. A. Haghighirad, R. L. Milot, W. H. Sio, M. R. Filip, B. Wenger, M. B. Johnston, L. M. Herz, H. J. Snaith, F. Giustino, *J. Phys. Chem. Lett* **2017**, *8*, 772.
[86] M. R. Filip, X. Liu, A. Miglio, G. Hautier, F. Giustino, *J. Phys. Chem. C* **2018**, *122*, 158.
[87] J. Zhou, Z. Xia, M. S. Molokeev, X. Zhang, D. Peng, Q. Liu, *J. Mater. Chem. A* **2017**, *5*, 15031.
[88] J. Luo, S. Li, H. Wu, Y. Zhou, Y. Li, J. Liu, J. Li, K. Li, F. Yi, G. Niu, J. Tang, *ACS Photonics* **2018**, *5*, 398.
[89] G. Volonakis, A. A. Haghighirad, H. J. Snaith, F. Giustino, *J. Phys. Chem. Lett* **2017**, *8*, 3917.
[90] J. Xu, J.-B. Liu, B.-X. Liu, B. Huang, *J. Phys. Chem. Lett* **2017**, *8*, 4391.

[91] J. Xu, J.-B. Liu, B.-X. Liu, J. Wang, B. Huang, *Adv. Funct. Mater.* **2019**, *29*, 1805870.
[92] J. M. Ball, A. Petrozza, *Nat. Energy* **2016**, *1*, 16149.
[93] W.-J. Yin, J.-H. Yang, J. Kang, Y. Yan, S.-H. Wei, *J. Mater. Chem. A* **2015**, *3*, 8926; M. H. Du, *J. Mater. Chem. A* **2014**, *2*, 9091.
[94] B. Yang, X. Mao, F. Hong, W. Meng, Y. Tang, X. Xia, S. Yang, W. Deng, K. Han, *J. Am. Chem. Soc.* **2018**, *140*, 17001.
[95] A. H. Slavney, L. Leppert, A. Saldivar Valdes, D. Bartesaghi, T. J. Savenije, J. B. Neaton, H. I. Karunadasa, *Angew. Chem. Int. Ed.* **2018**, *57*, 12765.
[96] W. Gao, C. Ran, J. Xi, B. Jiao, W. Zhang, M. Wu, X. Hou, Z. Wu, *ChemPhysChem* **2018**, *19*, 1696.
[97] M. Pantaler, C. Fettkenhauer, H. L. Nguyen, I. Anusca, D. C. Lupascu, *MRS Adv.* **2018**, *3*, 1819.
[98] F. Igbari, R. Wang, Z.-K. Wang, X.-J. Ma, Q. Wang, K.-L. Wang, Y. Zhang, L.-S. Liao, Y. Yang, *Nano Lett.* **2019**, *19*, 2066.
[99] E. M. Hutter, M. C. Gélvez-Rueda, D. Bartesaghi, F. C. Grozema, T. J. Savenije, *ACS Omega* **2018**, *3*, 11655.
[100] B. Yang, J. Chen, S. Yang, F. Hong, L. Sun, P. Han, T. Pullerits, W. Deng, K. Han, *Angew. Chem. Int. Ed.* **2018**, *57*, 5359.
[101] R. Kentsch, M. Scholz, J. Horn, D. Schlettwein, K. Oum, T. Lenzer, *J. Phys. Chem. C* **2018**, *122*, 25940.
[102] S. E. Creutz, E. N. Crites, M. C. De Siena, D. R. Gamelin, *Nano Lett.* **2018**, *18*, 1118.
[103] T. T. Tran, J. R. Panella, J. R. Chamorro, J. R. Morey, T. M. McQueen, *Mater. Horiz.* **2017**, *4*, 688.
[104] B. Saparov, J.-P. Sun, W. Meng, Z. Xiao, H.-S. Duan, O. Gunawan, D. Shin, I. G. Hill, Y. Yan, D. B. Mitzi, *Chem. Mater.* **2016**, *28*, 2315.
[105] B. Lee, C. C. Stoumpos, N. Zhou, F. Hao, C. Malliakas, C.-Y. Yeh, T. J. Marks, M. G. Kanatzidis, R. P. H. Chang, *J. Am. Chem. Soc.* **2014**, *136*, 15379.
[106] M. G. Brik, I. V. Kityk, *J. Phys. Chem. Solids* **2011**, *72*, 1256.
[107] B. Saparov, F. Hong, J.-P. Sun, H.-S. Duan, W. Meng, S. Cameron, I. G. Hill, Y. Yan, D. B. Mitzi, *Chem. Mater.* **2015**, *27*, 5622.
[108] J. You, Y. Yang, Z. Hong, T.-B. Song, L. Meng, Y. Liu, C. Jiang, H. Zhou, W.-H. Chang, G. Li, Y. Yang, *Appl. Phys. Lett.* **2014**, *105*, 183902.
[109] N. Sakai, A. A. Haghighirad, M. R. Filip, P. K. Nayak, S. Nayak, A. Ramadan, Z. Wang, F. Giustino, H. J. Snaith, *J. Am. Chem. Soc.* **2017**, *139*, 6030.
[110] L. Zhou, J.-F. Liao, Z.-G. Huang, X.-D. Wang, Y.-F. Xu, H.-Y. Chen, D.-B. Kuang, C.-Y. Su, *ACS Energy Lett.* **2018**, *3*, 2613.

[111] Y. Tong, E. Bladt, M. F. Aygüler, A. Manzi, K. Z. Milowska, V. A. Hintermayr, P. Docampo, S. Bals, A. S. Urban, L. Polavarapu, J. Feldmann, *Angew. Chem. Int. Ed.* **2016**, *55*, 13887.

[112] M.-G. Ju, M. Chen, Y. Zhou, H. F. Garces, J. Dai, L. Ma, N. P. Padture, X. C. Zeng, *ACS Energy Lett.* **2018**, *3*, 297.

[113] M. Wang, P. Zeng, S. Bai, J. Gu, F. Li, Z. Yang, M. Liu, *Sol. RRL* **2018**, *2*, 1870238.

[114] N. N. K, A. Nag, *Chem. Commun.* **2018**, *54*, 5205.

[115] F. Locardi, M. Cirignano, D. Baranov, Z. Dang, M. Prato, F. Drago, M. Ferretti, V. Pinchetti, M. Fanciulli, S. Brovelli, L. De Trizio, L. Manna, *J. Am. Chem. Soc.* **2018**, *140*, 12989.

[116] Y. Liu, Y. Jing, J. Zhao, Q. Liu, Z. Xia, *Chem. Mater.* **2019**, *31*, 3333.

[117] W. Lee, S. Hong, S. Kim, *J. Phys. Chem. C* **2019**, *123*, 2665.

[118] N. Chen, T. Cai, W. Li, K. Hills-Kimball, H. Yang, M. Que, Y. Nagaoka, Z. Liu, D. Yang, A. Dong, C.-Y. Xu, R. Zia, O. Chen, *ACS Appl. Mater. Interfaces* **2019**, *11*, 16855.

[119] Z. Tan, J. Li, C. Zhang, Z. Li, Q. Hu, Z. Xiao, T. Kamiya, H. Hosono, G. Niu, E. Lifshitz, Y. Cheng, J. Tang, *Adv. Funct. Mater.* **2018**, *28*, 1801131.

[120] A. Karmakar, M. S. Dodd, S. Agnihotri, E. Ravera, V. K. Michaelis, *Chem. Mater.* **2018**, *30*, 8280.

[121] J. D. Majher, M. B. Gray, T. A. Strom, P. M. Woodward, *Chem. Mater.* **2019**, *31*, 1738.

[122] W. Ning, X.-G. Zhao, J. Klarbring, S. Bai, F. Ji, F. Wang, S. I. Simak, Y. Tao, X.-M. Ren, L. Zhang, W. Huang, I. A. Abrikosov, F. Gao, *Adv. Funct. Mater.* **2019**, *29*, 1807375.

[123] L.-Z. Lei, Z.-F. Shi, Y. Li, Z.-Z. Ma, F. Zhang, T.-T. Xu, Y.-T. Tian, D. Wu, X.-J. Li, G.-T. Du, *J. Mater. Chem. C* **2018**, *6*, 7982.

[124] C. Wu, B. Du, W. Luo, Y. Liu, T. Li, D. Wang, X. Guo, H. Ting, Z. Fang, S. Wang, Z. Chen, Y. Chen, L. Xiao, *Adv. Opt. Mater.* **2018**, *6*, 1800811.

[125] J. Zhou, J. Luo, X. Rong, P. Wei, M. S. Molokeev, Y. Huang, J. Zhao, Q. Liu, X. Zhang, J. Tang, Z. Xia, *Adv. Opt. Mater.* **2019**, *7*, 1900139.

[126] Y. Li, Z. Shi, L. Lei, S. Li, D. Yang, D. Wu, T. Xu, Y. Tian, Y. Lu, Y. Wang, L. Zhang, X. Li, Y. Zhang, G. Du, C. Shan, *Adv. Mater. Interfaces* **2019**, *6*, 1900188.

[127] S. Ghosh, S. Paul, S. K. De, *Part. Part. Syst. Charact.* **2018**, *35*, 1800199.

[128] W. Pan, H. Wu, J. Luo, Z. Deng, C. Ge, C. Chen, X. Jiang, W.-J. Yin, G. Niu, L. Zhu, L. Yin, Y. Zhou, Q. Xie, X. Ke, M. Sui, J. Tang, *Nat. Photonics* **2017**, *11*, 726.

[129] H. Li, X. Shan, J. N. Neu, T. Geske, M. Davis, P. Mao, K. Xiao, T. Siegrist, Z. Yu, *J. Mater. Chem. C* **2018**, *6*, 11961.

[130] W. Yuan, G. Niu, Y. Xian, H. Wu, H. Wang, H. Yin, P. Liu, W. Li, J. Fan, *Adv. Funct. Mater.* **2019**, *29*, 1900234.
[131] Q. Hu, Z. Deng, M. Hu, A. Zhao, Y. Zhang, Z. Tan, G. Niu, H. Wu, J. Tang, *Sci. China Chem.* **2018**, *61*, 1581.
[132] P. C. Harikesh, H. K. Mulmudi, B. Ghosh, T. W. Goh, Y. T. Teng, K. Thirumal, M. Lockrey, K. Weber, T. M. Koh, S. Li, S. Mhaisalkar, N. Mathews, *Chem. Mater.* **2016**, *28*, 7496.
[133] W. Ke, M. G. Kanatzidis, *Nat. Commun.* **2019**, *10*, 965.
[134] K. M. Boopathi, P. Karuppuswamy, A. Singh, C. Hanmandlu, L. Lin, S. A. Abbas, C. C. Chang, P. C. Wang, G. Li, C. W. Chu, *J. Mater. Chem. A* **2017**, *5*, 20843.
[135] F. Jiang, D. Yang, Y. Jiang, T. Liu, X. Zhao, Y. Ming, B. Luo, F. Qin, J. Fan, H. Han, L. Zhang, Y. Zhou, *J. Am. Chem. Soc.* **2018**, *140*, 1019.
[136] C. Zuo, L. Ding, *Angew. Chem. Int. Ed.* **2017**, *56*, 6528.
[137] S. Chatterjee, A. J. Pal, *ACS Appl. Mater. Interfaces* **2018**, *10*, 35194.
[138] S. A. Adonin, L. A. Frolova, M. N. Sokolov, G. V. Shilov, D. V. Korchagin, V. P. Fedin, S. M. Aldoshin, K. J. Stevenson, P. A. Troshin, *Adv. Energy Mater.* **2018**, *8*, 1701140.
[139] A. J. Lehner, D. H. Fabini, H. A. Evans, C.-A. Hébert, S. R. Smock, J. Hu, H. Wang, J. W. Zwanziger, M. L. Chabinyc, R. Seshadri, *Chem. Mater.* **2015**, *27*, 7137.
[140] M. Lyu, J.-H. Yun, M. Cai, Y. Jiao, P. V. Bernhardt, M. Zhang, Q. Wang, A. Du, H. Wang, G. Liu, L. Wang, *Nano Res.* **2016**, *9*, 692.
[141] K. Eckhardt, V. Bon, J. Getzschmann, J. Grothe, F. M. Wisser, S. Kaskel, *Chem. Commun.* **2016**, *52*, 3058; T. Kawai, A. Ishii, T. Kitamura, S. Shimanuki, M. Iwata, Y. Ishibashi, *J. Phys. Soc. Jpn.* **1996**, *65*, 1464.
[142] S. Öz, J.-C. Hebig, E. Jung, T. Singh, A. Lepcha, S. Olthof, F. Jan, Y. Gao, R. German, P. H. M. van Loosdrecht, K. Meerholz, T. Kirchartz, S. Mathur, *Sol. Energy Mater. Sol. Cells* **2016**, *158*, 195.
[143] B.-W. Park, B. Philippe, X. Zhang, H. Rensmo, G. Boschloo, E. M. J. Johansson, *Adv. Mater.* **2015**, *27*, 6806.
[144] D. M. Fabian, S. Ardo, *J. Mater. Chem. A* **2016**, *4*, 6837.
[145] M. B. Johansson, H. Zhu, E. M. J. Johansson, *J. Phys. Chem. Lett* **2016**, *7*, 3467.
[146] P. H. Fourcroy, M. Palazzi, J. Rivet, J. Flahaut, R. Ceolin, *Etude du systeme AgIBiI3*, Vol. 14, 1979.
[147] https://inis.iaea.org/search/searchsinglerecord.aspx?recordsFor=SingleRecord&RN=17053980.
[148] L. F. Mashadieva, Z. S. Aliev, A. V. Shevelkov, M. B. Babanly, *J. Alloys*

Compd. **2013**, *551*, 512.
[149] A. Koedtruad, M. Goto, M. Amano Patino, Z. Tan, H. Guo, T. Nakamura, T. Handa, W.-T. Chen, Y.-C. Chuang, H.-S. Sheu, T. Saito, D. Kan, Y. Kanemitsu, A. Wakamiya, Y. Shimakawa, *J. Mater. Chem. A* **2019**, *7*, 5583.
[150] Y. Kim, Z. Yang, A. Jain, O. Voznyy, G.-H. Kim, M. Liu, L. N. Quan, F. P. García de Arquer, R. Comin, J. Z. Fan, E. H. Sargent, *Angew. Chem. Int. Ed.* **2016**, *55*, 9586.
[151] Z. Xiao, W. Meng, D. B. Mitzi, Y. Yan, *J. Phys. Chem. Lett* **2016**, *7*, 3903.
[152] I. Turkevych, S. Kazaoui, E. Ito, T. Urano, K. Yamada, H. Tomiyasu, H. Yamagishi, M. Kondo, S. Aramaki, *ChemSusChem* **2017**, *10*, 3754.
[153] N. Pai, J. Lu, T. R. Gengenbach, A. Seeber, A. S. R. Chesman, L. Jiang, D. C. Senevirathna, P. C. Andrews, U. Bach, Y.-B. Cheng, A. N. Simonov, *Adv. Energy Mater.* **2019**, *9*, 1803396.